UCLouvain

École polytechnique de Louvain

Measurements and analysis of electronic transport in etched graphene nanoconstrictions

Author : **Florian Baulard**
Supervisor : **Benoît Hackens**
Readers : **Vincent Bayot**, **Jean-Christophe Charlier**
Academic year 2018–2019
Master [120] in Physical Engineering

Acknowledgements

First of all, I would tremendously thank my supervisor Dr. Benoît Hackens who gave me the opportunity to work on this project linked to the field of research. His expertise and helpful suggestions have made have paved the way to make this project better. Also, I would highly thank my main assistant and PhD student Nicolas Moreau for always being available in helping and supporting myself during the measurements and the study of data as well as regarding the simulation part. I warmly thank the post-doc Boris Brun-Barrière who has been there for helping in the experimental part and giving me the authorization access to the system of sample measurements. His great expertise in the control and solving experimental issues has been precious for being able to finish all data acquisitions without much problem.

Contents

Introduction

In the world of nanostructures, graphene is one of the most promising materials. Since its first isolation in 2004 [1], it has already been investigated a lot in fundamental physics research as well as for the potential of making new nanoelectronic devices. Fundamentally speaking, what especially makes graphene so unique is its honeycomb-like geometry associated with a localization of energy linear dispersions . The latter are characterized by a zero-gap band structure under the shape of two connecting Dirac cones. This property leads to an ambipolar behavior for conduction either by electrons or holes. Furthermore, it gives to graphene an extremely high mobility of carriers with an approximate Fermi velocity $v_F \simeq c/300$, with c the speed of light. The carriers are like if they flow in graphene with no mass and they are described by the Dirac equation, from which we call them *massless Dirac fermions*. However, in practice, most of the transport measurements involving graphene on a substrate (typically in field-effect transistors) have featured results which were far from corresponding to the intrinsic properties: the most known results from the measurements are much lower carrier mobility and non-zero conductance values at the charge neutrality point like reported in Ref. [1]. Precisely, the most used substrate was silicon dioxide SiO_2 which typically generates a strong inhomogeneous doping in graphene, hence strongly limiting the mobility of the carriers being consequently affected by numerous scattering events. A highly more suitable substrate greatly considered since one decade is hexagonal boron-nitride (hBN). The carrier mobility as well as the homogeneity of local charge density have been largely improved using such kind of substrate [2][3].

Quantum Point Contact (QPC) is a narrow and short constriction either defined by split-gate electrodes [4] or by a lithographically-etched geometry [5] in a high-mobility two dimensional electron gas (2DEG). It is one of the most simple objects in the field of mesoscopic (quantum) and ballistic transport mainly due to the easy quantum confinement which unambiguously leads to conductance quantization with discrete carried quanta described by the quantum of conductance $2e^2/h$. This allows the propagation of specific electronic modes defined as quasi one-dimensional channels. However, more intricate aspects behind size quantization come enriching physics with varied interactions such as quantum interferences, resonances and the influence of a perpendicular magnetic field. In lithographically-etched QPCs, quality of the edges is believed to be also determinant in the transport characteristics: bad edge quality can eventually hide the quantization steps due to pronounced coherent backscattering. In graphene, the demonstration of size quantization is even tougher due to its typical linear dispersion which allows to probe more numerous quantum interferences caused by impurities than in conventional III-V heterostructures. Transport occurring at low carrier density like charging effects produced by localized states near the QPC edges.

Quantum Hall Effect (QHE) is one of the most remarkable quantum physical phenomena. It takes place in a 2-dimensional electron gas (2DEG) subjected to high magnetic fields. The characteristic of the QHE is the possibility to observe series of plateaus at specific fundamental values being multiples of the quantum of conductance e^2/h. The discovery of the QHE has allowed to open ways to investigate deeper in the mesoscopic physics. In addition, the charge carriers in graphene differently behave in the quantum Hall regime. Indeed, an unconventional effect compared to 2DEGs rises with Dirac fermions leading to conductance quantization with a succession of steps $2e^2/h$, $6e^2/h$, $10e^2/h$, ...

In this master thesis report, the aim is to cover and describe several electronic properties that can be determined in two different samples. The samples both include a geometrical, etched constriction featuring a width at the nanometer scale for investigating quantum transport. The samples will be compared by discussing about the results and graphics based on basic transport measurements under magnetic fields or at different temperatures.

Chapter 1 covers the most essential notions about the nanostructures of interest like graphene and the quantum point contacts. A modest description of the technologically advances in graphene nanoconstrictions is then given. Finally, a theoretical review of the quantum Hall effect and its implication in graphene ends the current Chapter.

Chapter 2 is about the experimental part of the project. The samples and their mounting on a sample holder are described. After that, the working of cryogenic system used for the measurements at low temperatures and the setup are provided. Finally, all aspects regarding the electronic tools and the system of control of the measurements are given.

Chapter 3 covers the most important part of this manuscript. It focuses on the analysis of data collected from the graphene QPC devices at low temperatures and subjected to perpendicular magnetic field. Firstly, general characterizations of the samples are described along with a discussion about their quality or defects. Secondly, the results possibly evoking signatures of size quantization and quantum ballistic transport due to the nanoconstrictions are analyzed and discussed at the low-magnetic field regime. Thirdly, the high field regime is explored by evidencing some peculiar features in the quantum Hall regime. Lastly, a simulation part is realized and constitutes an attempt of reproducibility of an observed experimentally observed based on specific hypotheses.

Chapter 1

Theoretical notions and state of the art

This chapter will introduce the theoretical part of this master thesis report by giving the essential properties of monolayer graphene as well as the influence of the choice of the substrate on based-graphene device properties. Then, a definition of the quantum point contact (QPC) is given as well as its impact on transport. Finally, a theoretical development until the description of the quantum Hall effect is given. The anomalous quantum effect called half-integer quantum Hall in graphene is also described.

1.1 Graphene

The following description is based on two heavy papers which summarize the main structural and electronic characteristics of graphene [4]-[6].

1.1.1 General description

Graphene is an allotrope of the carbon and presents an hexagonal structure as presented in Fig. 1.1. The atomic spacing between two neighboring sites is 1.42 Å. This lattice can be viewed as two triangular sub-lattices interpenetrating. The unit cell and the corresponding Brillouin zone are pictured in Fig. 1.1. The lattice vectors are $a_1 = \frac{a}{2}(3, \sqrt{3})$ and $a_2 = \frac{a}{2}(3, -\sqrt{3})$, while the reciprocal lattice vectors are $b_1 = \frac{2\pi}{3a}(1, \sqrt{3})$ and $b_2 = \frac{2\pi}{3a}(1, -\sqrt{3})$. It can already be noticed that two important points in the Brillouin zone appear: $\boldsymbol{K} = (\frac{2\pi}{3a}, \frac{2\pi}{3\sqrt{3}a})$ and $\boldsymbol{K'} = (\frac{2\pi}{3a}, -\frac{2\pi}{3\sqrt{3}a})$. The importance of those points will be explained later.

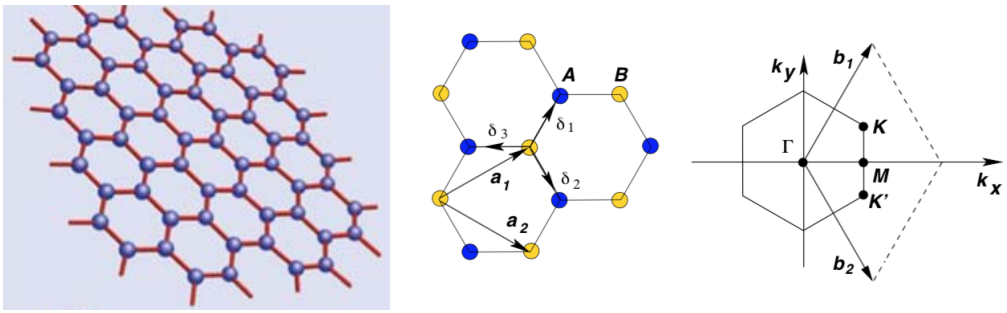

Fig. 1.1. Left: Atomical structure of graphene [6]. Center: Unit cell of graphene with the lattice vectors in the real (a_1, a_2) [6]. Right: The Brillouin zone and the lattice vectors in the reciprocal space (b_1, b_2) [6].

The carbon atoms are hybridized sp^2 and each one makes one single σ bond per three neighboring atoms in-plane. A π orbital appears in the out-of-plane direction. This orbital allows the electronic conduction while the σ ones give extreme mechanical resistance. The discretized energy band for the electron of the bondings is shown in Fig. 1.2. As it can be seen, the π bond is half empty.

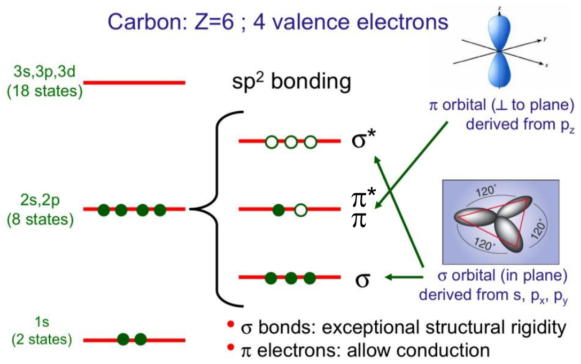

Fig. 1.2. Electronic structure of graphene. *Taken from LMAPR2015 course on graphene.*

A last thing that should be mentioned is that two different edge states appear in graphene: the armchair one and the zig-zag one. Both of them are presented in Fig. 1.3.

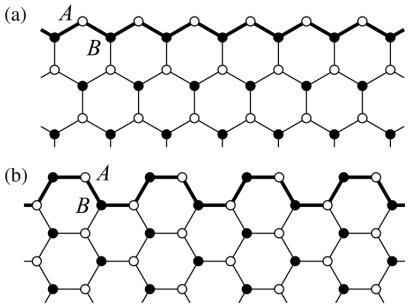

Fig. 1.3. The two different edge states (a) the zig-zag one and (b) the arm chair one [7].

1.1.2 Electronic properties

The electrons on a graphene sheet have a mobility of approximately 20.000 $cm^2/(V \cdot s)$ at room temperature, only limited by phonon-electron interactions. As explained in the previous section, the free electrons come from the π orbitals and create a two-dimensional electronic gas (2DEG) on the graphene layer.

Graphene is a semiconductor with zero band gap. Its conduction and valence bands meet at the Fermi level but no electrons are available in the conduction band at 0 K. As it will be shown later, the electrons propagating in graphene behave like if they were massless.

To compute the band structure, the tight-binding approach can be used. This method attributes to each site a certain energy and a probability for the electron to hop from one site to one of its nearest neighbours. This can be translated into the following formalism:

- 2 atoms per unit cell: A and B (see Fig. 1.4);
- 1 orbital per atom, namely the p_z one: $|p_z\rangle$;
- First neighbour interactions:

$$\langle p_z^A | T | p_z^B \rangle = t$$
$$\langle p_z^A | V + T | p_z^A \rangle = \epsilon.$$

  with T and V being the components of the Hamiltonian: the kinetic energy and the potential respectively. ϵ is the onsite energy.

With those hypotheses, the following dispersion relation can be found:

$$E(\mathbf{k}) = E_F \pm t\sqrt{1 + 4\cos\left(\frac{\sqrt{3}k_x a}{2}\right)\cos\left(\frac{k_y a}{2}\right) + 4\cos^2(\frac{k_y a}{2})}, \tag{1.1}$$

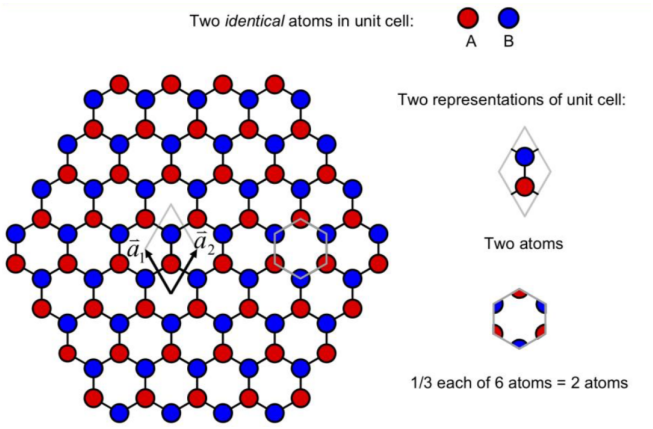

Fig. 1.4. Formalism used for the tight binding calculations with two possible unit cells. *Taken from LMAPR2015 course on graphene.*

where E_F is the Fermi level energy, $t \approx 2.8\ eV$ is the hopping energy, $\mathbf{k}$ is the wave vector and $a \approx 2.46$ Å the lattice parameter (i.e. the distance between two neighbouring sites within a sub-lattice A or B). The $\pm$ signs correspond to the conduction and valence bands respectively. This function is shown in Fig. 1.5.

At 0 K, the valence band is completely filled and the conduction band empty. Both encounter at 6 different points (the $\boldsymbol{K}$ and $\boldsymbol{K'}$ points of the Brillouin zone).

Now, at low energy, a quick analysis leads to the observation of an energy proportional to the momentum of the electrons. This behaviour is a lot alike the one of massless particles like photons. Those particles are known as Dirac fermions and are described by the Dirac equation:

$$v_F \vec{\sigma} \cdot \nabla \Phi(\mathbf{r}) = E\Phi(\mathbf{r}) \tag{1.2}$$

where $v_F = \frac{3ta}{2} \approx 10^6$ m/s is the Fermi velocity, $\overrightarrow{\sigma}$ is the Pauli matrices (σ_x, σ_y) or $(\sigma_x, -\sigma_y)$ and $\phi(\mathbf{r})$ is the wave function of the electron.

The dispersion relation is given at those points by:

$$E(\mathbf{k}) = \pm\hbar v_F \sqrt{k_x^2 + k_y^2} = \pm\hbar v_F |\mathbf{k}|. \tag{1.3}$$

The shape of the band is pictured in Fig. 1.5.

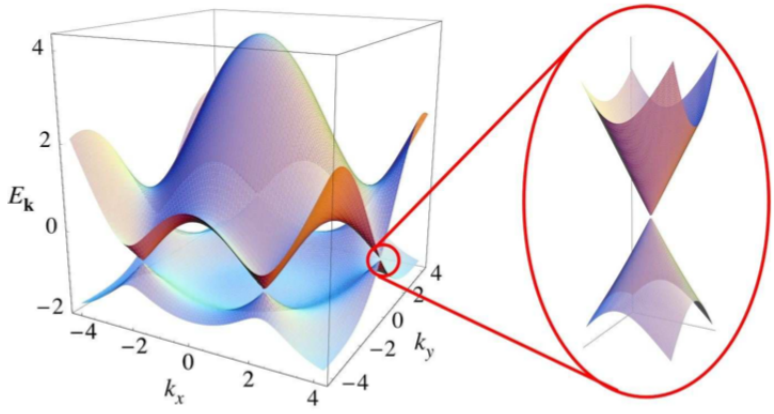

Fig. 1.5. Band structure in the momentum space of graphene and a zoom on the low energy near the $\boldsymbol{K}$ points [6].

In comparison, electrons usually present an energy proportional to the square of the momenta in most materials. Here an inverted cone (known as the Dirac cone) represents this photon-like property. In fact, the effective mass of electrons inside graphene is non-zero but so small that the particles (electrons and

holes) travel at a speed of $0.003 \cdot c$ with c the light celerity.

Those results are confirmed by the cyclotron mass which should be constant if the Schrödinger equation was the one describing the behaviour of the electron but should depend on the density if the Dirac equation is the one that is applied. Using the semiclassical approach [6], it can be found that the cyclotron mass, m^* is:

$$m^* = \frac{\sqrt{\pi}}{v_F}\sqrt{n} \tag{1.4}$$

with n the electronic density. This formula has been found to be in good agreement with the experimental data.

The density of states $D(E)$ is shown in Fig. 1.6. It can be evidenced that this density near the Dirac points is:

$$D(E) = \frac{2A_c}{\pi}\frac{|E|}{v_F^2}, \tag{1.5}$$

with $A_c = \frac{3\sqrt{3}}{2}a^2$ the unit cell area ($a \sim 0.142$ Å being here the carbon-carbon distance in graphene). In a nanoribbon, this density follows a $1/\sqrt{E}$ law due to its edge states (due to the boundary conditions).

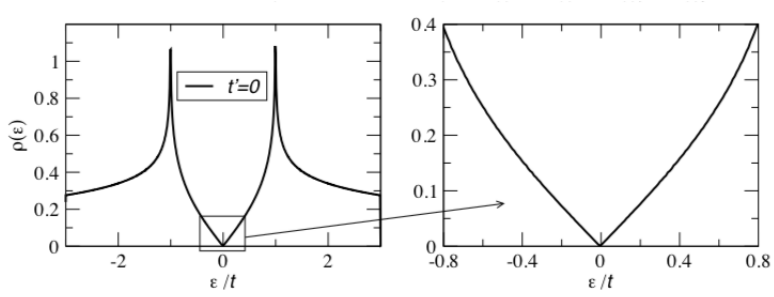

Fig. 1.6. Density of states in graphene with a zoom closer to the linear evolution at low Fermi energy [6].

The wave functions at $\boldsymbol{K}$, Φ_K, and $\boldsymbol{K'}$, $\Phi_{K'}$, are respectively:

$$\Phi_{\pm,K}(\boldsymbol{k}) = \frac{1}{\sqrt{2}}\begin{pmatrix} e^{(-i\theta_k)/2} \\ \pm e^{(i\theta_k)/2} \end{pmatrix} \tag{1.6}$$

and

$$\Phi_{\pm,K'}(\boldsymbol{k}) = \frac{1}{\sqrt{2}}\begin{pmatrix} e^{(i\theta_k)/2} \\ \pm e^{(-i\theta_k)/2} \end{pmatrix} \tag{1.7}$$

with $\pm$ signs corresponding to the eigenenergy $E = \pm v_f \hbar k$. This shows why a distinction have to be made between $\boldsymbol{K}$ and $\boldsymbol{K'}$ points.

The Fermi wave vector k_F is defined as the quantity indicating that all electronic states whose non-interacting momentum eigenstates $q < k_F$ are filled:

$$n = g_s g_v \int_{|\mathbf{q}|<k_F} \frac{dq}{(2\pi)^2} \rightarrow k_F = \sqrt{\frac{4\pi n}{g_s g_v}} \tag{1.8}$$

with n the 2D carrier density, g_s the spin degeneracy equals to 2 and g_v the valley degeneracy also equals to 2 for a monolayer graphene, giving the relation $k_F = \sqrt{\pi n}$. The double valley degeneracy comes from the fact that two symmetrical sublattices exist in the hexagonal structure, thus actually appearing in the $\boldsymbol{K}$ and $\boldsymbol{K'}$ points.

One more thing that could be observed is that, following the edge configuration of the ribbon, the energy spectrum will vary due to their different boundary conditions as indicated in Fig. 1.7. The armchair edges can lead to a non-zero band gap for small width.

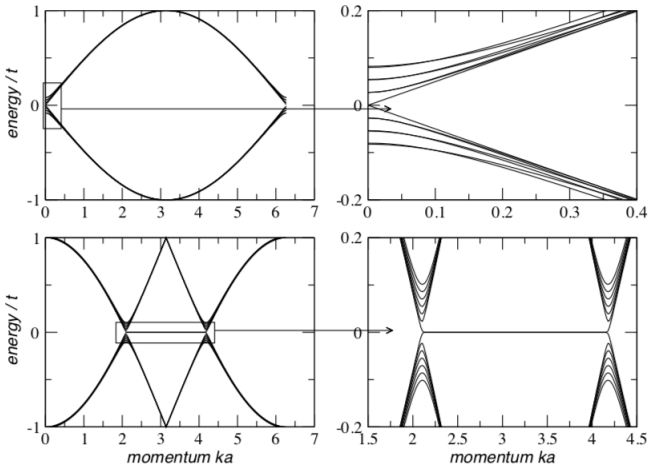

Fig. 1.7. Energy spectrum of a nanoribbon 200 cells wide with armchair (top) and zigzag (bottom) edges with a zoom on the low energy values on the right [4].

Regarding magneto-electric properties, the first thing to notice is that Dirac fermions have a cyclotron frequency $w_c = \sqrt{2}\frac{v_F}{l_B}$ with $l_B = \sqrt{\frac{\hbar}{eB}}$, the magnetic length, which follows a $\sqrt{B}$ law with B the magnetic field. Next to that, non-relativistic particles follow a linear law with B.

The magnetic field can be added to the Dirac equation:

$$v_F[\vec{\sigma} \cdot (-i\nabla + e\mathbf{A}/c)]\Phi(\mathbf{r}) = E\Phi(\mathbf{r}) \tag{1.9}$$

with $\mathbf{A}$ the Landau Gauge and e the electron charge. It can be found that each mode of the 1 harmonic oscillators can be constructed from the ground mode and their energy is proportional to $w_c \propto \sqrt{B}$ and to $\sqrt{N}$ with N the mode number. It has to be noticed that the ground mode have zero energy. The different solutions for the modes are called Landau levels and are four-fold degenerated since the spectrum is the same at $\boldsymbol{K}$ and $\boldsymbol{K'}$ (spin degeneracy is already taken into account). The resulting density of states is shown in Fig. 1.8. The corresponding energy evolution for the Nth Landau level is $E_N = \pm v_F\sqrt{2\hbar eNB}$ with the presence of a peculiar zero mode $N = 0$ in which an equal amount of holes and electron is shared.

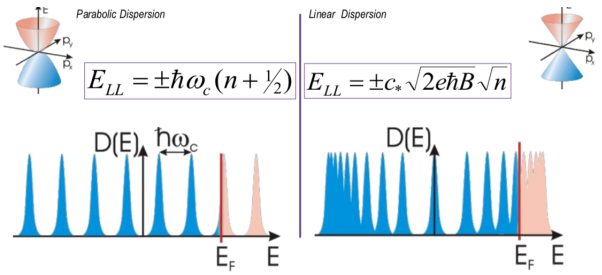

Fig. 1.8. Density of states of graphene under magnetic field (on the right) compared to the one of a material having a parabolic dispersion (on the left). *Taken from LMAPR2015 course on graphene.*

1.1.3 Substrate influence on electronic transport

General

In a practical point of view, the efficient use of graphene for electronic transport in the nanoelectronic usage is actually a complex task. In classical transistors, the most famous dielectric substrate is silicon dioxide SiO_2 which has a good chemical stability and capability of charge storing to limit current flow.

However, the efficiency of graphene devices deposited on SiO_2 is very reduced compared to its expected intrinsic properties. The carrier mobility is limited by scattering process, surface roughness of the substrate as well as the impinged impurities. In addition to that, a non zero conductivity is observed at the Dirac point, i.e. the charge neutrality point (see results in Ref. [1]). This is explained by the appearance of a network of hole and electron puddles which does not make a clean 2D electron gas (2DEG) anymore. Instead, one observes an inhomogeneous 2DEG with associated doping away from the charge neutrality point, caused by some charge trapped in the substrate or at the graphene-substrate interface. The electrostatic landscape featuring these hole-electron puddles at the charge neutrality point produces a residual doping and a finite carrier density which contributes to this peculiar transport characteristic such as a non-zero minimum conductivity value [8]. Alternatives to solve these issues have been found like the method of suspended graphene to improve the carrier mobility but this limits the architecture of the device as well as its functionality [2]. The relevant objective is thus to find a very pure substrate into physical contact with graphene and which could fit the geometry of the latter to avoid the drop of mobility.

The use of hexagonal boron nitride (hBN) as a substrate for graphene is a very good effective way for exhibiting better electronic properties: one can recover the loss of mobility and functionality occurring with the above-mentioned devices. As can be seen in Fig. 1.9, hBN is an hexagonal system of boron and nitrogen atoms occupying one different sublattice (A and B sites) each, leading to a finite band gap ($\simeq 5.9\ eV$) in the electronic structure, unlike graphene which only has carbon atoms at each sublattice. Being atomically flat, the geometry of hBN is similar to graphene and there is only about 1.8 % of lattice constant mismatch of no-strained graphene on hBN [9]. Moreover, hBN is inert, free of dangling bonds and can be fabricated with very low impurity concentrations [10]. All these characteristics of hBN are keys for the fabrication of well-functionalized and more efficient devices involving stack of graphene/hBN van der Waals heterostructures, where the scattering process is substantially reduced (allowing for better mobility).

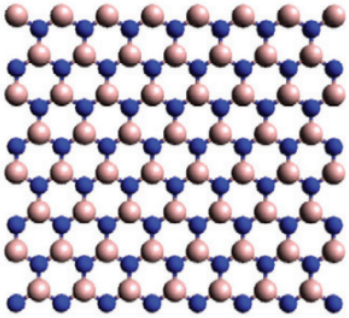

Fig. 1.9. Flat hBN diagram [11].

Examples based on electronic transport measurements and spectroscopy

Transport measurements on a graphene/hBN heterostructure have been done to demonstrate the higher quality of choosing a hBN substrate rather than SiO_2 for graphene [2]. Curves of the resistance and the corresponding conductivity as a function of the backgate voltage V_g or equivalently the carrier density n are displayed in Fig. 1.10 **(a)**. The resistance peaks are very narrow and are located at the charge neutrality point near $V_g = 0\ V$, showing a weak extrinsic doping of graphene and consequently a low impurity concentration (like the charge-carrier inhomogeneities). As charged impurities are actually dominant for the scattering process (long-range scattering or Coulomb scattering due to potential screening from the charge defects [8]) at low carrier densities, this proves their poor contribution. In addition, the narrowness of the peaks gets sharper as the temperature decreases, indicating carrier-phonon scattering process mitigation at very low temperature. All resistance curves saturate towards a single residual resistance at the high carrier density regime where short-range impurity scatterings are dominant. The mobility of such device is density-independent as long as the conductivity curve is linear, which is here only the case close to the charge neutrality point according to the inset in Fig. 1.10**(a)**. The semi-classical Drude model consists in a simple way to extract a mobility value μ only within the linear part of the conductivity curve:

$$\sigma = ne\mu,$$

where e is the electronic charge. Since σ linearly evolves with n (either in the hole side $n < 0$ or the electron-side $n > 0$), computing the derivative $\frac{d\sigma}{dn}$ is enough. The mobility has been computed at $T = 200\ K$ based on the linear part of the conductivity curve: $\mu \simeq 60.000\ cm^2V^{-1}s^{-1}$, which is very high yet not the best knowing that better quality samples like graphene encapsulated in between hBN allow to reach much higher mobility (up to $150000 - 250000\ cm^2V^{-1}s^{-1}$ [5][12]), thus with even better flatness, protection against external impurities and efficient fabrication methods.

To be more comparative, the electronic transport properties characterized by resistivity measurements of another single graphene flake on hBN and on SiO_2 can be studied based on Fig. 1.10**(b)**[1]. The measurements point out that the electronic transport using hBN as a substrate is much cleaner than transport using the SiO_2 substrate. The latter produces a much broader resistivity peak far away from $V_g = 0\ V$ and higher residual resistivity at high densities, which clearly means a strongly reduced carrier mobility compared to graphene/hBN stack. The value of mobility in both cases are: $\mu_{hBN} \simeq 20.000\ cm^2V^{-1}s^{-1}$ and $\mu_{SiO_2} \simeq 2.000\ cm^2V^{-1}s^{-1}$.

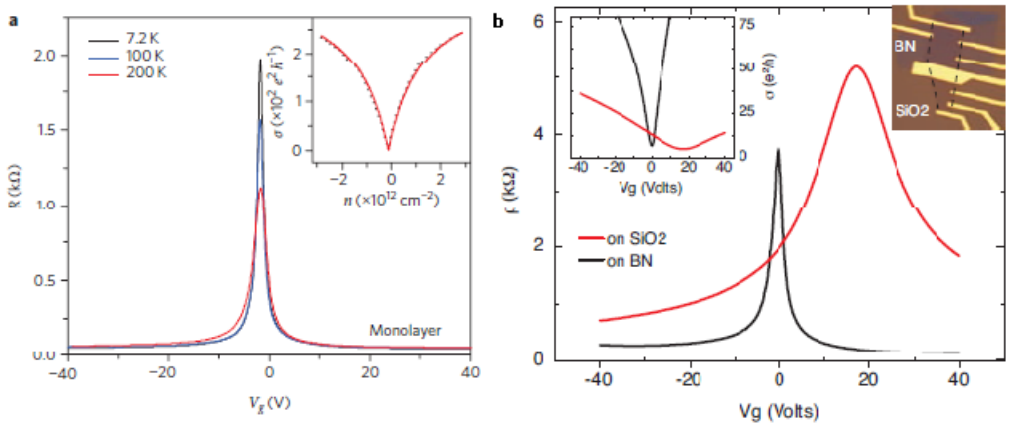

Fig. 1.10. **(a)** Measurement of the resistance and the corresponding conductivity (inset) of a monolayer graphene on hBN at different temperatures. **(b)** Measurement of the resistivity and the corresponding conductivity (left inset) of another single graphene flake both on hBN and SiO_2 (device drawn on right inset) [2].

As can be seen on Fig. 1.11, the mapping of the topography as well as the position-dependent charge densities has been done for graphene on hBN and graphene on SiO_2. The topography maps have been obtained by raster scan with a STM tip in constant current mode whereas the local density of carriers have been obtained by the measurements of the Dirac point energy $E_D(x, y)$ by spectroscopy. When looking at the maps, in addition to seeing a much better roughness for graphene/hBN, the associated charge fluctuations are much more mitigated, leading to a better charge inhomogeneity suppression compared to graphene on SiO_2. This is an indication of better stability, less long-range (Coulomb) scattering events and improved local intrinsic properties of graphene deposited on hBN substrate.

1.2 Quantum point contacts

1.2.1 Definition and main results regarding electronic transport

In the field of quantum transport, *Quantum Point Contacts* (QPCs) are very short and narrow constrictions usually at the nanometer scale connecting two conducting reservoirs defined in high-mobility two dimensional electron gas (2DEG) devices. The low transverse dimension of the constriction, i.e. its width W, is responsible for the quantum confinement of the transverse momentum of the electrons (leading to subbands in the energy dispersion) and for quasi one-dimensional transport with specific channels carrying electronic modes. These modes are also transverse and are characterized by a definite energy spacing ΔE according to W.[2] This spacing leads to conductance quantization in units of the quantum

[1] Found in the « Supplementary information » file from the current reference.

[2] The dispersion relation of the subbands $E_n(k)$ is: $E_n(k) = E_n + \frac{\hbar^2 k^2}{2m^*}$, where k is the momentum of the propagating mode along the conductor, E_n the energy corresponding to the lateral confinement and m^* the effective mass [13].

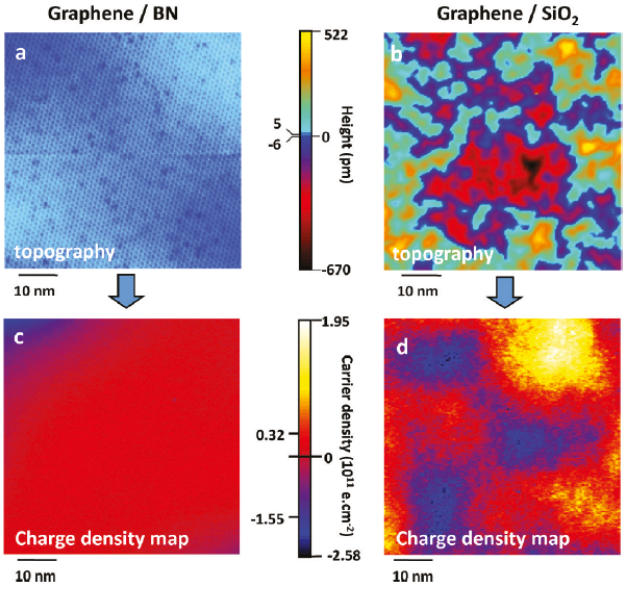

Fig. 1.11. Topography and charge density maps of graphene/hBN (**a**,**c** respectively with bias voltage $V_b = 0.25\ V$ from the STM tip to the sample and gate voltage $V_g = -6\ V$) and graphene/SiO_2 (**b**,**d** respectively with bias voltage $V_b = -0.225\ V$ from the STM tip to the sample and gate voltage $V_g = 15\ V$) heterostructures [3].

of conductance $G_0 = 2e^2/h$, where "2" accounts for spin degeneracy. The conductance G will thus evolve by step of G_0 and will depend on the number N of transmitted modes at a specific Fermi level.

The most famous efficient device that have been fabricated to make a 2DEG with high-mobility of the carriers back to the eighties is a heterostructure featuring a heterojunction where the electrons are confined in a 2D interface layer between AlAs and AlGaAs (III-V heterostructures) using molecular beam epitaxy for a good matching of the lattices. The principle is to engineer the band structure to realize a quantum triangular well where the electrons can be trapped without undergoing scatterings from impurities, giving their high mobility [14]. An image of this kind of device with this interface is shown in Fig. 1.12 (left). A QPC is defined there by the famous technique consisting in repelling electrons underneath a specific region using split gates at the top. In this way, the electronic path at the defined global carrier density is constrained to go through the tiny constriction which is not affected by the electrostatic perturbation from the gates. Higher negative split-gate voltages allow the gradual reduction of the constriction width W. The resulting quantized conductance measurement is shown in right of Fig. 1.12, where G is decreasing as long as the width is diminished by further increasing the voltages toward more negative values. The physical effect is obviously the reduction of transmitted modes due to an improved confinement (the energy spacing ΔE between the subbands associated to the modes increases when W decreases).

The required conditions to well reproduce the expected properties from a QPC is that the Fermi wavelength of the electrons must be comparable to the width of the constriction: $\lambda_F \sim W$ (leading to mesoscopic transport from which the wavy nature of electrons takes part) and that the electronic mean free path l_e must excess the length of the constriction L to allow ballistic transport [15]. These two conditions are keys to clearly observe the quantized values of the conductance associated to quantum confinement by the constriction size and they are based on the quantum ballistic transport being an ideal transport regime to achieve this objective of size quantization observation. The different transverse modes are characterized by a wave function ψ_n associated to the nth mode for each. These wave functions are defined as harmonic oscillators[3] for which a multiple of the half electronic wavelength $\lambda_F/2$ fits in the channel of the constriction, across its width W. Thus the first mode which can be transmitted is corresponding to an electronic wave of wavelength $\lambda_F/2$, then the second λ_F, then $(3/2)\lambda_F$ etc. In this way, each additional step in the conductance evolution will occur when the corresponding Fermi wave number $k_F = \dfrac{2\pi}{\lambda_F}$ times the constriction width W reaches a multiple of π, leading to one more transmitted

[3]It can be analytically computed by the Schrödinger equation using a realistic parabolic confinement.

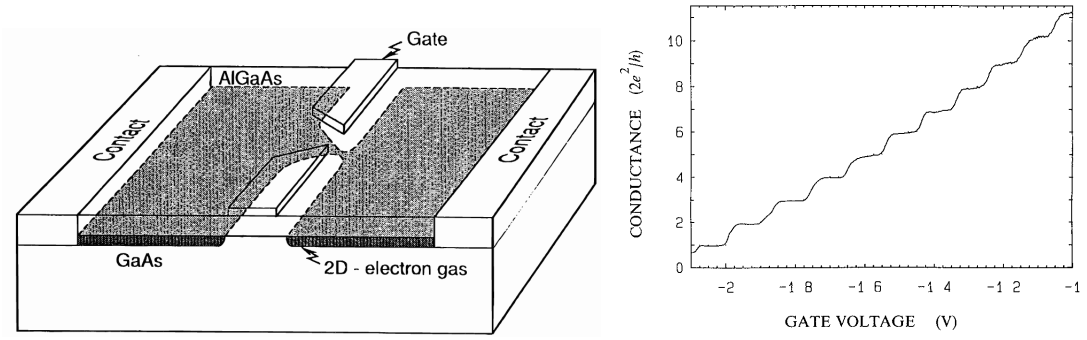

Fig. 1.12. (Left) Schematic cross-sectional view of a quantum point contact, defined in a high-mobility electron gas at the interface of a GaAs–AlGaAs heterojunction. The point contact is formed when a negative voltage is applied to the gate electrodes on top of the AlGaAs layer. Transport measurements are made by employing contacts to the 2D electron gas at either side of the constriction [15]. (Right) Conductance of a QPC as a function of gate voltage, in units of $2e^2/h$. The trace exhibits steps corresponding to conductance quantization [16].

mode:

$$G = G_0 N,$$

where $N = Int[k_F W/\pi]$ is the number of perfectly transmitted modes[4] (cases where transmissions are not perfect will be discussed later). The associated mean evolution of G is width-dependent and can be described as follows:

$$G^{(0)} = G_0 \frac{k_F W}{\pi},$$

for which the evolution is thus faster when W increases, interpreted by less spaced subbands in terms of energy [13].

A QPC is defined to have a length L in the order of its width W: $L \sim W$, instead of being a quantum wire where the length is much larger than the width. Unlike what could be thought, the smooth transitions from plateaus to plateaus observable in right of Fig. 1.12 instead of sharp quantization steps are not resulting from the thermal averaging of the finite temperature but from the small length of the constriction which opens energy windows between the plateaus [14]. The width of these windows are characterized by an energy defined by a longitudinal curvature ω_x, being $\hbar\omega_x$. The curvature is even more pronounced that the length is reduced. The mathematical interpretation of this smoothening is the non-unit transmission coefficient $T_n(E)$ of the transverse modes for which modes above the Fermi energy E_F are not necessarily described by $T = 0$ and modes below E_F are not necessarily described by $T = 1$. So this effect can be present even at zero temperature: it solely depends on the geometry of the constriction. The ideal case for infinitely sharp transitions would be attributed to an infinitely long wire with $\omega_x = 0$. However, the dependence on temperature for the quality of the quantized conductance observation is still valid. As long as the thermal energy and specifically the associated width of the thermal smearing in the Fermi-Dirac distribution $f(E)$ ($\sim 4k_B T$, where k_B is the Boltzmann constant) is getting comparable to the energy spacing between the modes in QPCs, the corresponding thermal averaging starts to obscure the clear steps as can be seen in left of Fig. 1.13.

As temperature is low enough to induce mesoscopic transport (i.e. when the memory phase of the electronic waves is conserved on a relatively large distance compared to the characteristic length of the device), resonances and quantum interferences between electronic paths by coherent backscattering are believed to result in discreet oscillatory structures of the conductance (see top curve in right of Fig. 1.13 at zero magnetic field) [13]. These can blur the clear plateaus obtained in devices featuring QPCs since the associated confined region is more prompted to quantum interferences with reflections and coherent backscattering. To be precise, resonances lead to non-unit transmission coefficients of modes being partly reflected in the entrance and the exit of the constriction, which is by the way more specifically observed in abrupt constriction when $L \sim W$; quantum interferences occur via electron backscattering by collisions with impurities near the opening of the constriction. Very weak increasing perpendicular magnetic fields allow to mitigate this effect without qualitatively changing the electronic states inside the constriction

[4] See Appendix B for computation details about the conductance obtaining within the Landauer formalism in 1D transport through a perfect quantum wire.

and thus flatten the plateaus by partially suppressing the oscillatory structures as can be seen in right of Fig. 1.13.

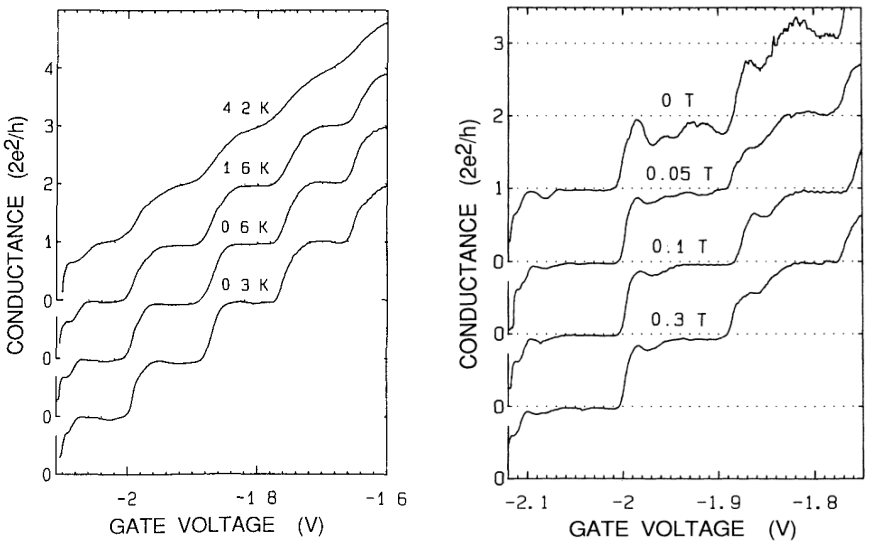

Fig. 1.13. (Left) Breakdown of the conductance quantization due to temperature averaging. The curves have been onset for clarity [16]. (Right) Oscillatory structure observed in the zero-field conductance of a point contact at 40 mK (top curve). Some of the oscillatory structure is suppressed by a weak magnetic field (lower three curves) [13].

When the magnetic field becomes stronger, the intrinsic energy spectrum defined in the constriction can be modified and lead to magnetic population of the 1D subbands. The cyclotron motion caused by the magnetic field B is characterized by the cyclotron orbit at the Fermi energy, also called cyclotron radius: $l_c = \dfrac{\hbar k_F}{eB}$. The modified 1D subbands under sufficiently strong magnetic fields are called *magneto-electric subbands* and their associated cyclotron orbit, and thus the trajectories, are really affected by the lateral confinement in the constriction. Therefore, it is a really specific aspect found in QPCs. If $l_c >> W$ (weak magnetic fields), the electronic trajectories are not much affected by the perpendicular magnetic field and the energy spectrum remains the classical one and the number of N occupied subbands is B-independent (indeed, no change in the plateau widths is observable in right of Fig. 1.13 at weak magnetic field increasing). When B increases and l_c approaches W, the energy spectrum gets modified and is defined by the magneto-electric subbands with a corresponding depopulation of modes so that the N initial transmitted modes through the QPC (at $B = 0\ T$) can be lower at constant k_F. However, the effect remains very weak compared to the next case. When $l_c < W/2$ and thus fits into the channel, the corresponding electronic states in the constriction drastically change by their extension along the boundaries, called *edge states*. They are characterized by more strongly localized wave functions (see the transition in left of Fig. 1.14) and classically correspond to the skipping orbits developing along both edges. Such states are characteristic of the *Landau levels* in classical 2DEGs with the corresponding energy dispersion:

$$E_n = \left(n + \frac{1}{2}\right)\hbar\omega_c,$$

where $\omega_c = eB/m$ corresponds to the cyclotron frequency. The number of transmitted modes in the Landau level quantization regime is approximately $N \sim E_F/\hbar\omega_c$ and the depopulation of the modes thus evolves as $1/B$ (the depopulation of the magneto-electric subbands is less faster but of course occurs when B still increases). The effect of the magnetic field from the quantized 1D subbands towards the formation of edge states described by the Landau levels is shown in right of Fig. 1.13. This shows that the transition is continuous, with plateaus getting less numerous and wider as long as the magnetic field gets higher within similar split-gate voltage ranges defining the width of the constriction. The depopulation of modes is clearly demonstrated.

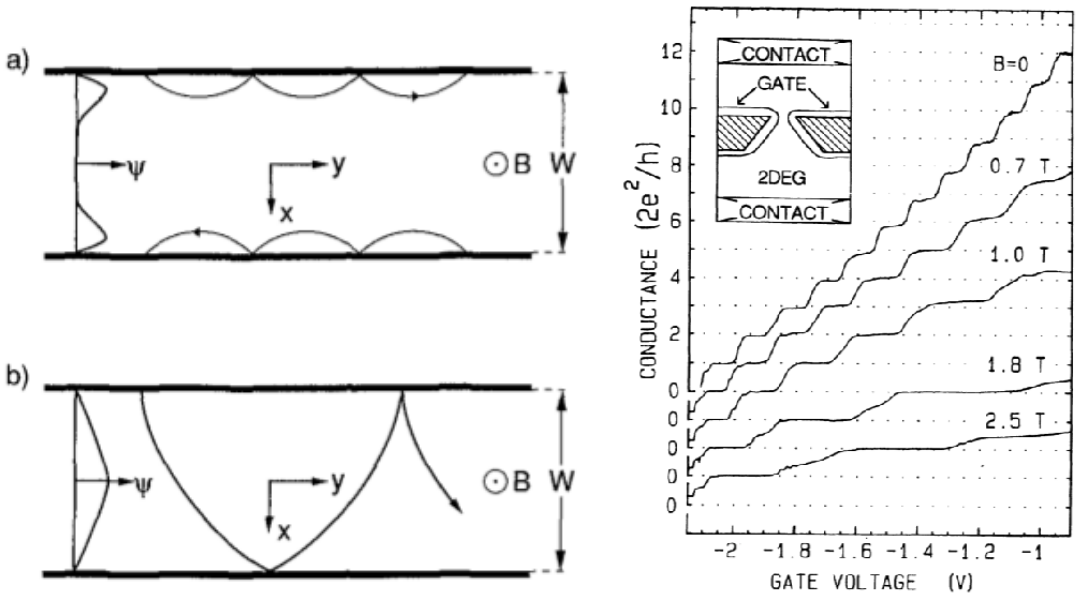

Fig. 1.14. (Left) Trajectories in a narrow channel in a perpendicular magnetic field (right) and the corresponding transverse profile of the wave function Ψ (left). Skipping orbits on both opposite edges and the corresponding edge states are shown in (a), a traversing trajectory and the corresponding bulk state in (b). Note that the wave functions shown correspond to the nodeless $n = 1$ mode [13]. (Right) Transition from quantization in zero field (subbands) to quantization in high magnetic fields (Landau levels), obtained at several fixed values of the magnetic field at 0.6 K. The conductances were calculated from the measured resistances after subtraction of the resistances of the bulk contacts. The curves have been offset for clarity [16].

1.2.2 QPCs in graphene

Since a decade, the research realm has notably focused and progressed on the fabrication and characterization of better and better defined nanowires and nanoconstrictions involved in diverse graphene devices. The transport phenomena which could be expected through these nanostructures have been very challenging to experimentally reproduce due to several important factors like the choice of the substrate under monolayer graphene, the fabrication techniques used for defining the nanowires/nanoconstrictions etc. One of the biggest issues to clearly observe the QPC operation in graphene is its typical gapless band structure because of which an induced depleted region from for instance global electron doping must be hole doped. In contrast with classical semiconductors, this leads to new physics in low-density transport with the presence of two-type carrier conduction via electron-hole puddles particularly in disordered structures [8]. If a QPC in graphene is defined using the split-gate technique, the signature of subband quantization at zero magnetic field is almost impossible due to the typically Klein tunneling phenomena which allow electronic paths to be transmitted through p-n junctions mostly defined by the split-gates with a radial angle of incidence [17]. The work of Katrin Zimmermann was about the QPC operation defined by split-gates in high-mobility hBN-graphene-hBN devices. Her main way to be able to work with an operating QPC is the access to the quantum Hall regime as well as the QPC size tuning with the aim of controlling the transmission of quantum Hall edge channels (see such device in left of Fig. 1.15) [12].

The alternative way to tailor a graphene constriction for quantum confining Dirac fermions is based on the etching process to give a geometrical nanoconstriction width. However, many challenges have faced the researchers over the years to be able to distinguish clear confinement and quantized conductance resulting from size quantization. Indeed, works involving graphene on SiO_2 substrate have revealed strong diffusive regime due to low mobility and disorder-dominant transport in the constriction leading to localization and to a transport gap with associated suppressed conductance and resonances [18]. Indeed, the confinement effect brought by the constriction provokes the rise of a confinement gap which isolates the hole and electron puddles characteristic of a certain disorder potential fluctuation. This corresponds to a landscape of quantum dots along the constriction and which give rise to the Coulomb-blockade transport, contributing to charging effects within the dots. Hence, it does not contribute to

transport but charging events, which explains the transport gap observed around the charge neutrality point. However, in the paper, a new model justifies the localization effects rather occurring on the rough edges instead of inside the nanoribbons. The edge roughness is produced by reactive ion etching (RIE) which also gives the constriction geometry and width and may add additional impurity affecting transport inside the constriction. So, transport seems to be highly dependent on rough edges depending on this fabrication step. The transport regime farther from the low-density range also obscures the genuine quantization due to diffusive conduction. A strong improvement of device quality regarding disorder reduction is the fabrication of suspended graphene above a SiO_2/Si substrate and supported by pillars made into LOR-A polymer, reported by Tombros *et al.* [19]. Their device is shown in right of Fig. 1.15 and features nanoconstrictions in the A and B region actually produced by a current annealing step giving also extremely high mobility (i.e. 600000 $cm^2V^{-1}s^{-1}$ reported in the Tombros' paper) allowing ballistic transport. The electrical measurements have shown clear quantized conductance due to electronic confinement and with step intervals about $2e/h$ suggesting lifting of valley degeneracy. Also, transitions from quantized conductance at 0 T to the quantum Hall regime above 60 mT have been observed in this high quality device. Yet, several issues in such devices exist: they are fragile and lack of control over the dimensions. Especially, the control of the constriction widths is not possible due to the current annealing step forming the constriction geometry [20].

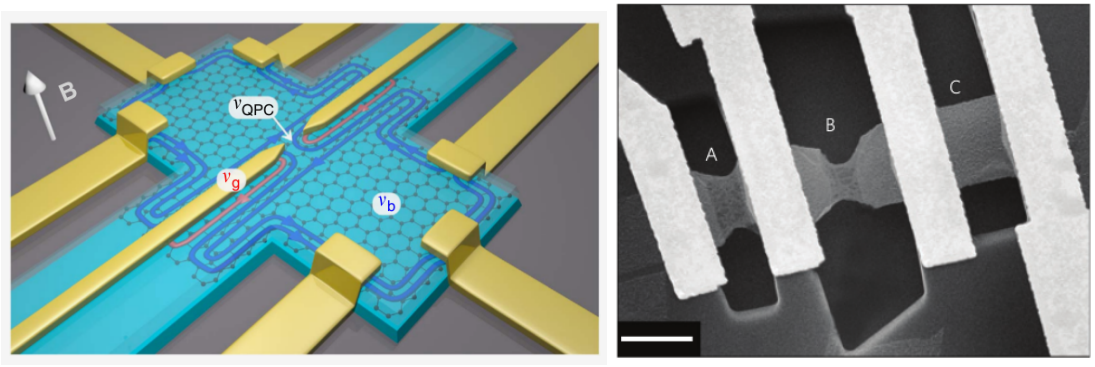

Fig. 1.15. (Left) Schematic of the device showing graphene encapsulated in hBN (top hBN flake semi-transparent) with electrodes contacting the graphene on the edge of the heterostructure. Edge channels formed at high magnetic field are shown as red (hole) and blue (electron) channels [12]. (Right) Scanning electron microscopy picture of a typical suspended high-mobility graphene device showing the formation of graphene constrictions after the current annealing step in vacuum at 4.2 K (regions A and B). The scale bar is 2 µm [19].

So far, researchers had to go back to graphene devices directly on a suitable substrate to expect transport to be governed by at least quasi-ballistic conduction (so that only boundaries, crystal alignment and edge defects limmit transport) instead of domination by disorder [5]. As previously mentioned, the use of hBN as a new substrate compared to SiO_2 is highly adapted for that. Indeed, graphene on hBN nanostructures can notably benefit from carrier mobility one order of magnitude higher than the use of SiO_2 substrate at low carrier density, i.e. $\mu > 45000 cm^2V^{-1}s^{-1}$ reported in Ref. [21]. In the cited paper, different nanoribbons of similar width have been fabricated by dry RIE using mostly argon with few percent oxygen. Surprisingly, the transport characteristics done on these etched nanoribbon graphene on hBN devices have reminded a lot the ones interpreted by localized states and charge puddles in the ribbons like in Ref. [18] for graphene on SiO_2. Therefore, despite the overall better quality device using hBN substrates instead of silicon dioxide, it seems that transport in the constrictions is also mostly dependent on edge disorder produced by RIE. In addition, strong variations in conductance evolution have been reported for different nanoribbons of roughly same width from the same graphene flake, which harder supports this high depedence on RIE producing the rough edges.

The most successful and qualitative device so far which exhibits extremely clean and mostly ballistic conductance evolution belongs to Christoph Stampfer and Terrés's team. It is made of encapsulated graphene between two hBN layers on top of a SiO_2/Si substrate with very short nanoconstrictions produced by RIE in a SF_6 atmosphere (see left of Fig. 1.16) [5]. The sandwiched graphene may have the advantage of more flattening the graphene layer and protecting the bulk from external contaminants. Before the etching process, their initial Hall bar device has been measured for a computed mobility up to $150000 cm^2V^{-1}s^{-1}$, which makes the mean free path higher than the relevant length scales in the constric-

tion devices at $\Delta V_g = 4.6\ V$. This characteristic allows mostly ballistic transport even at very low carrier density. In that case, the evolution of conductance is $\sqrt{V_g}$-dependent and thus $\propto k_F = \sqrt{\pi\alpha(V_g - V_{g0})}$ (α is defined as the capacitive coupling between graphene and the underlying hBN + SiO_2 substrates). In right of Fig. 1.16, the experimental conductance traces in function of k_F are represented by the black and green curves for their 230nm-wide constriction. Like expected, a linear evolution away from the Dirac point is observed showing ballistic transport (indeed, it is parallel to the theoretical linear curve shown in red dashed lines for ideal graphene). However, traces close to the Dirac point are deviations from the linear behavior . This is attributed to transport dominated by trap states at the edges which localize electrons and give rise to charging events instead of pure transport evolution, which is similar to cases in the previously-mentioned graphene devices [18][20]. The green curve gets a wider conductance valley compared to the black one because it was obtained after a cool-down process during which species in air have induced chemical modifications in the graphene edges and have generated more localized states. Although this explanation mostly justifies the deviation from linear evolution (because the ballistic transport highly dominates), electron-hole puddles or charged impurities cannot be fully neglected even if they should be very reduced in these kinds of devices. In the ballistic regime of the experimental conductance traces, conductance steps are found on the drawn red horizontal lines on the electron side with even spacing. These are believed to be steps from size quantization and demonstrate the high quality of the device. In addition, instead of being sharp steps, they appear more like "kinks" which are thought to be attributed by edge disorder with associated backscatterings leading to quantum interferences with resonant paths (like Fabry-Pérot interferences).

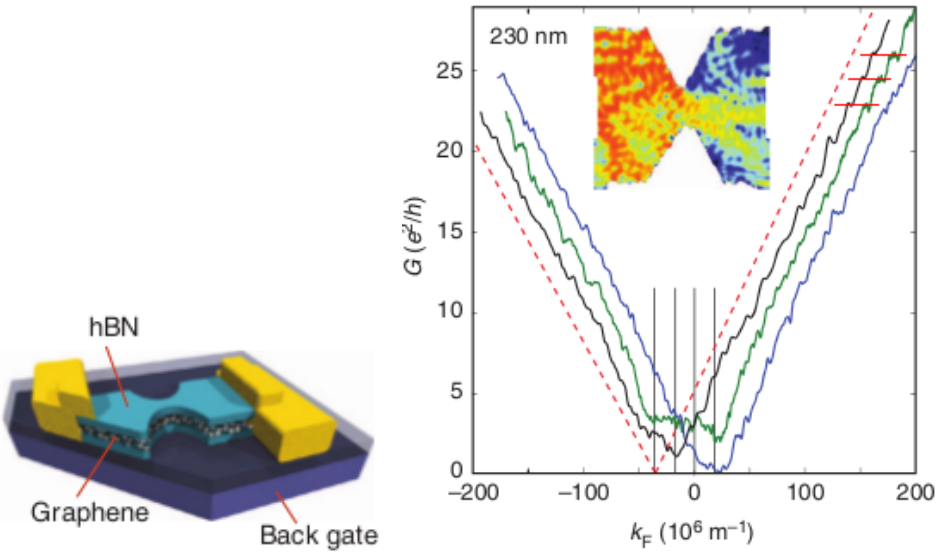

Fig. 1.16. (Left) Schematic illustration of a hBN–graphene sandwich device with the bottom and top layers of hBN appearing in green, the gold contacts in yellow, the SiO_2 in dark blue and the Si backgate in purple. (Right) Experimental conductance trace G as a function of k_F after correction for the density of trap states (black and green curves) and theoretical simulations of the graphene quantum point contact (blue curve). In the experimental curves, the small red horizontal lines on the electron side are evenly-spaced conductance steps reminiscent of quantized 1D subbands. Ideal transmission $\propto k_F$ is shown in dashed red lines as guide to the eye. Curves are offset horizontally for clarity [5].

The Landauer theory describes transmission via ballistic transport. In a constriction with width W, the conductance in this model must increase by additional conductance quantum $(2-4)e^2/h$ whenever Wk_F reaches a multiple of π and, after a Fourier expansion from the native expression (see the latter in Ref. [5] showing the step function), is:

$$G = \frac{4e^2}{h}\frac{c_0 W k_F}{\pi} + \frac{4e^2}{h}\left[\sum_{j=1}^{\infty} c_j \sin\left(2jWk_F - \phi_j\right) - \frac{c_0}{2}\right], \tag{1.10}$$

which thus describes the quantum ballistic transport. The "4" factor accounts for valley and spin degeneracy and this equation neglects minor phase contribution due to details in graphene edges. c_0

is called the limited average transmission of 1D modes and is equals to 1 if the constriction is perfect. The infinite sum corresponds to periodic modulations of the conductance steps and is expected to decay towards infinity (i.e. c_j increases) with random scattering phases $\Phi_j \neq 0$ for a non-ideal constriction with also $c_0 < 1$. This is symptomatic of the "kinks" shown in right of Fig. 1.16. If the linearization from Equation 1.10 is considered, i.e. by subtracting the periodic modulations, one accesses to the average conductance $G^{(0)}$:

$$G^{(0)} = \frac{4e^2}{h}\frac{c_0 W k_F}{\pi} - \frac{4e^2}{h}\frac{c_0}{2}. \tag{1.11}$$

Therefore, the conductance evolution can be on average reduced from the ideal constriction with geometrical width W if $c_0 < 1$ interpreted by limited transmissions of electronic modes. The product $c_0 W$ is thus considered as an "effective width" and is determined by the slope of the linear evolution in the ballistic conductance trace. Comparisons between the real widths and the corresponding effective widths have been done in Terrés *et al.*'s paper and are shown in left of Fig. 1.17 for holes and electrons. The global trend is that c_0 gets reduced as long as the width decreases, which is interpreted by more probable scattering events at the rough edges. The presence of edge disorder and the "kink" structure of the steps has also been consistent with theoretical investigations in the paper. The fact that size quantization can be identified in conductance traces (or other methods) whereas strong scattering at rough edges can dominate is explained by a model based on conduction transport through a constriction and is illustrated in right of Fig. 1.17 [22]. Given the quality in the bulk with highly mitigated scattering by impurities (situation A), the strongest scatterers in well-fabricated hBN/graphene/hBN devices are located at the graphene edges with possible scattering mechanisms at the boundaries of the device (situation B) or of the constricted area (situation C). The collision mechanisms at the edges induce $\boldsymbol{K}$-$\boldsymbol{K'}$ (or intervalley) scatterings and these are actually probing disorder at very small length scales compared to classical III-V heterostructures like GaAs-GaAlAs, notably due to higher momentum and thus smaller Fermi wavelength λ_F[5]. In the classical heterostructures, it is thus easier to identify the conductance steps (see Fig. 1.12). Therefore, the scattering events in graphene devices impact a lot transport. However, the use of the quantum ballistic transport model described by Equation 1.10 is nonetheless valid and is supported by the free defect zone at the center of the constriction which allows ballitic conduction through it. Hence, despite the rough edge impact, identification of clear conductance step originating from size quantization remains possible in high-mobility graphene devices and especially in encapsulated graphene since only the boundaries can be contaminated by external species while allowing ballistic transport of modes through the inner channels of the constriction.

1.3 Quantum Hall effect

Mainly based on Ref. [17].

1.3.1 General description

Before informing about the Quantum Hall effect (QHE), one needs to understand how electrons move in a x-y plane with the presence of an electric field $\overrightarrow{E} = E_x\overrightarrow{e_x}$ and a perpendicular magnetic field $\overrightarrow{B} = B_z\overrightarrow{e_z}$. Without magnetic field the electron moves and accelerates along the x-axis, i.e., in the $\overrightarrow{E}$ direction. With the magnetic field, the electron whose propagation is perpendicular to the field deviates from his trajectory due to Lorentz forces and develops motion into circles. This motion is characterized by the cyclotron frequency $\omega_c = eB/m^*$, where m^* is the effective mass of the free electron in two dimensions. The matrix equation which dictates the motion in such situation links $\overrightarrow{E}$ and current density $\overrightarrow{J} = e\overrightarrow{v_D}n$, where $\overrightarrow{v_D}$ the drift velocity and n the electronic density:

$$\begin{bmatrix} E_x \\ E_y \end{bmatrix} = \begin{bmatrix} \frac{m^*}{e\tau} & -B \\ B & \frac{m^*}{e\tau} \end{bmatrix} \begin{bmatrix} \frac{J_x}{ne} \\ \frac{J_y}{ne} \end{bmatrix} = \rho_0 \begin{bmatrix} 1 & -\mu B \\ \mu B & 1 \end{bmatrix} \begin{bmatrix} J_x \\ J_y \end{bmatrix}.$$

$\rho_0 = 1/(ne\mu)$ is the longitudinal resistivity, $\mu = e\tau/m^*$ the mobility and τ the relaxation time of the carier momentum. By injecting ρ_0 into the matrix containing μB, one obtains the resistivity tensor $\boldsymbol{\rho}$ with elements $\rho_{xx} = \rho_{yy} = \rho_0$ and $\rho_{xy} = \rho_{yx} = B/ne$. This latter definition allows to determine carrier density by identifying linear developments of the Hall resistivity (or resistance R_{xy}) in function of B,

[5] Indeed, as long as λ_F becomes lower than the mean free path l_e, mesoscopic transport comes into play with quantum interferences between coherent electronic paths scattered by impurities and defects.

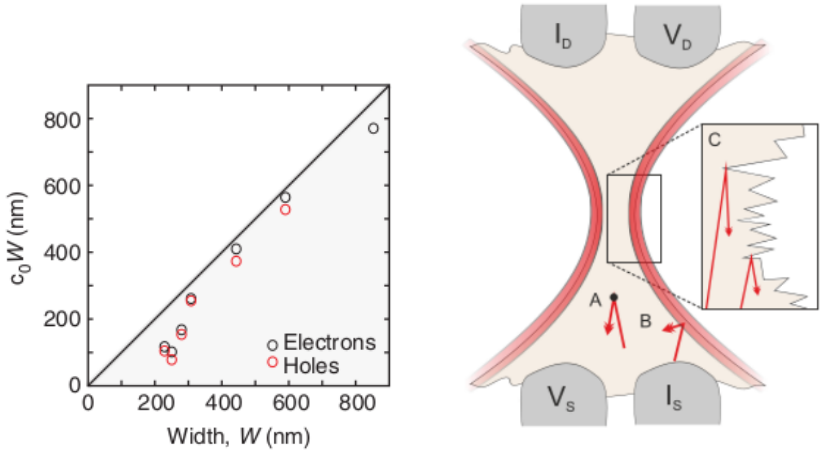

Fig. 1.17. (Left) Comparison of c_0W from the fits on conductance traces with the width W (extracted from SEM images) in samples of Terrés and his team [5]. (Right) Schematic representation of the transport through a graphene quantum point contact. The scattering on a point defect in the bulk is represented in A. The scattering mechanism can also occur at the boundaries of the device (situation B). The scattering phenomena may also happen in the constricted area (situation C). In ballistic graphene devices, the region with a high concentration of scattering centers are the edges of the graphene device (region highlighted in red) [22].

from which the slope $1/ne$ can be extracted. These expressions are described in the low B-field regime, characteristic of the classical Hall effect.

Now if the magnetic field further increases, it may happen that electrons develop orbital motion with several full cycles before being scattered and loosing their momentum. The condition to account for this phenomenon is that $\omega_c\tau = \mu B >> 1$. This is also called the "quantum limit" and is described by the quantization of the kinetic energy of the electrons. The resulting discrete energy levels, also called *Landau levels* like shown in graphene review, can be determined solving the Schrödinger equation under an external magnetic field and by introducing a Landau gauge $\overrightarrow{A}$ (see the base reference of this section). The solving equation is a 1D Schrödinger equation of a free particle in a quadratic potential, which corresponds to the Hamiltonian of an harmonic oscillator in one direction. The eigenvalues give rise to the energy spectrum of the Landau levels

$$\epsilon_N = \hbar\omega_c \left(N + \frac{1}{2}\right),$$

where $N = 0, 1, 2, ...$ are indexes of the levels. The energy spacing is constant between all levels for a fixed magnetic field. Without any applied electric field, the electrons do not move and are spatially localized with development of closed orbits at high magnetic fields: the group velocity is zero. The classical 2D electron gas is characterized by a density of states (DOS) which is constant and independent of kinetic energy. When the magnetic field increases to the Landau level regime, the DOS starts to split up into a series of narrow peaks (see left of Fig. 1.8). At an intermediate level, the peaks are not fully separated and give rise to Shubnikov-de Haas oscillations whose periodicity in longitudinal resistivity ρ_{xx} evolves in $1/B$ (see Fig. 1.18 at roughly 1 T). When the peaks are fully separated, ρ_{xx} drops to zero and the Hall or transverse resistivity shows a plateau. This is the characterization of the quantum Hall effect (QHE) and it is also seen in Fig. 1.18 at high fields with successions of zero ρ_{xx} associated with a plateau in the Hall resistivity and then maxima of ρ_{xx} and a corresponding transition between two plateaus. This paper originates from the work of von Klitzing who won a Nobel prize for the discovery of QHE.

The Landau levels are degenerate with a corresponding density of filling $n_L = eB/h = B/\phi_0$, where ϕ_0 is the quantum of magnetic flux. One can compare this density in proportion to the total density of electrons n defining the filling factor

$$\nu = \frac{n}{n_L} = \frac{1}{g_s g_v}\frac{nh}{eB}$$

, where g_s and g_v correspond to spin and valley degeneracy in case of graphene (typically "4"). Only spin degeneracy is accounted in 2D electron gas.

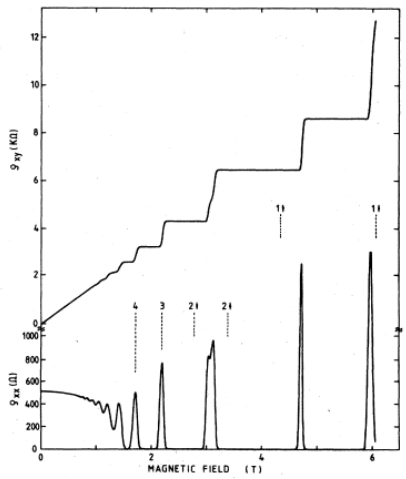

Fig. 1.18. Experimental curves for the Hall resistance $R_H = \rho_{xy}$ and the resistivity ρ_{xx} of a heterostructure as a function of the magnetic field at $V_g = 0\ V$ and at $T = 8\ mK$ [23].

In the presence of edges in a sample, the electrons undergoing strong magnetic fields and subjected to the quantum Hall effect will accumulate towards the edges where the electron density drop exactly to zero. This causes the bending up of the Landau levels due to a potential confinement as can be seen in Fig. 1.19a). If the Fermi energy E_F lies within two Landau levels in the bulk, the QHE model tells that there is conduction of edge channels whose number corresponds to the crossed bent levels with E_F. This aspect is the key for the experimental observation of the QHE. The channels at opposite edges have counter-propagating direction due to the derivative of the potential confinement with group velocity $v_g \propto \dfrac{\partial V(y)}{\partial y}$ with $y = \hbar k_x/(eB)$ the centre coordinate. These separated channels cannot allow backscattering in the QH regime when the bulk is protected from electron transferring: i.e. it is suppressed and this corresponds to the quantized plateau manifestation with dissipationless conduction. The integer QHE is the most common effect and the quantized transverse resistance is described as $R_{xy} = h/(e^2\nu)$.

Physically, bulk disorder gives rise to potential fluctuations with distributed hills and valleys with corresponding fluctuating Landau levels in the bulk (see Fig. 1.20). When E_F crosses this potential; localized states are formed and become small enough to protect the edges from percolation, i.e. filtering edge channels into the bulk. When localized states dominate, conduction is suppressed inside the bulk and edge channels are propagating along the boundaries without backscattering. Hence, a quantized plateau in the transverse resistance occurs (see Fig. 1.20a)). The schematic view of this regime can be seen in Fig. 1.19c) and b) where localized states are actually occupying the valleys of the Landau levels. When carrier density changes, E_F can well lie in a close specific Landau level and this gives rise to percolation of the corresponding edge channel into the bulk with backscattering before reaching the opposite side. This disturbs the quantization process and instead, one lies on a transition between two plateaus (see Fig. 1.20 with corresponding decrease of density or increase in magnetic field) and the longitudinal resistance rises to a maximum. The filling states provoking the percolation events are called extended states and are localized around the peaks of DOS associated with Landau levels (see Fig. 1.19b) and d) for a schematic view of a percolation mechanism). These successions of quantization and loss of quantization happen while tuning either the carrier density or the magnetic field further.

There are explanations which tell why the quantized plateaus get a finite width instead of being a smooth linear evolution of the transverse resistance. The finite width is said to originate from bulk disorder in samples, which gives actually rise to the broadening of the DOS of the Landau levels. Higher disorder more broadens the peaks and makes way for more randomly-distributed potential fluctuations and localized states. In absence of disorder, the Fermi level jumps to Landau level to Landau level in a direct way on changing carrier density or magnetic field. In disordered devices, as electrons can be trapped into equipotential lines generated by these localized states, the Fermi level can be actually pinned and trapped in the gap state in between peaks in the DOS. Since these states are not contributing to transport, the bulk is insulating and the longitudinal resistance zero, and one lies on a quantum Hall plateau in the transverse conductance. Hence, the pinning of the Fermi level is stable for finite ranges of carrier density or magnetic field before being moved towards an adjacent Landau level, which

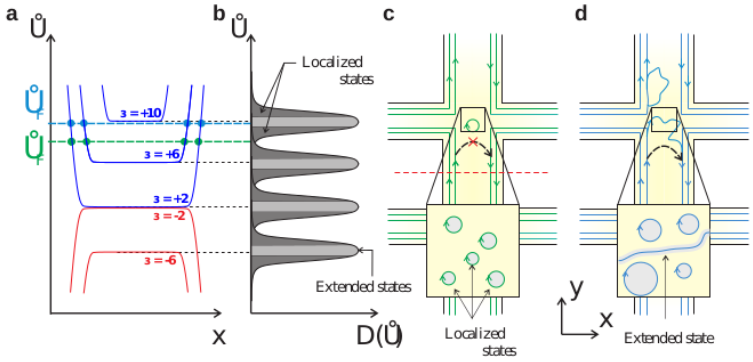

Fig. 1.19. a) Cross-sectional view (red dashed line in panel c)) of the energy spectrum. b) Broadened Landau levels. The states whose Fermi level E_F lies within the light gray region are considered extended. Otherwise, the states remain localized (dark gray region). c) Representation of the localized states within the sample surface. A percolation path to counter-propagating edges state is non-probable. d) The extended states can link counter-propagating edges states [22].

is responsible of the plateau finite width.

The stable edge channels in case of quantization situation (E_F lying in between two bulk Landau levels), 1D conduction transport in the ballistic regime can be used, similarly to the 1D transmission of modes in QPCs. The way the conductance is extracted is similar except that instead of modes, number of edge channels N will matter. If transmission of channels are perfect ($T_r = 1$), then the conductance is simply computed as $G = \frac{2e^2}{h}N$, similar to the Landauer formula in case of fully ballistic transport and thus quantization manifestation. In addition, the Landauer-Büttiker formalism allows to theoretically get back to the transport characteristics associated with transmitted ballistic 1D edge channels in a several-contacted Hall bar. The injection of current and known voltage drops, along with the Landauer formula allows the construction of a conductance matrix from which longitudinal and Hall resistance can be determined, knowing the N flowing edge channels. In addition, the Hall and longitudinal conductance are respectively determined as follows:

$$G_{xx} = \frac{R_{xx}}{R_{xx}^2 + R_{xy}^2}$$

and

$$G_{xy} = \frac{R_{xy}}{R_{xx}^2 + R_{xy}^2}.$$

Katrin Zimmermann has also developed the formalism within split-gated quantum point contacts [17]. This reasoning allows to consider a number of transmitted channels and also backscattered channels close to the QPC. The most useful transport characteristic which only depends on the number of transmitted channels is the diagonal conductance. That way, this leads to a better comprehension of the physics behind backscattered channels in the QPC surrounding. That is how she could work well on the transmission control of channels in her thesis. In the experiments of this master thesis work, no diagonal measurement has been realized, therefore only the number of the total channels can be easily known by direct reading of the quantized Hall conductance.

1.3.2 Half-integer quantum Hall effect in graphene

Where one puts our interest on systems involving Dirac fermions, i.e. in graphene, the quantization results are fundamentally different from classical 2D fermions. In graphene, the linear dispersion and the bipolar charge carriers of holes and electrons are responsible for another type of QHE. Novoselov *et al.* were able to observe the QHE in graphene directly after its discovery [24]. The transverse conductivity and longitudinal conductivity in graphene at 14 T are displayed in Fig. 1.21 (not the inset which is bilayer graphene). As in classical 2D electron gas, successive plateaus in σ_{xy} correspond to drop in ρ_{xx}. But the sequence of the plateaus are totally different and it can be described by writing the transverse

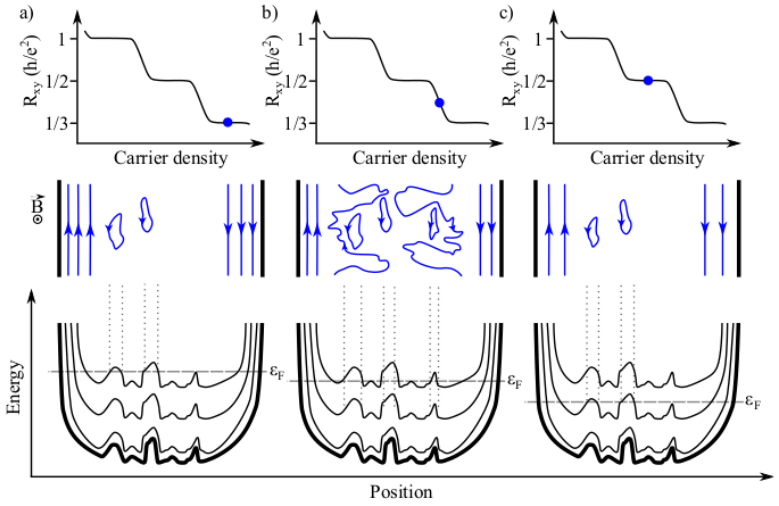

Fig. 1.20. Schematic drawing of the evolution of Landau levels and the corresponding situation of channels in the sample at increasing carrier density from a) to c). a) When the Fermi level lies between two Landau levels, edge channels propagate at both sides of the sample, and backscattering is fully suppressed. The resistance is quantized. b) Once the Fermi level is close to a Landau level, edge channels percolate through the bulk connecting both sides of the sample giving rise to backscattering. The resistance is not quantized anymore but transits between two plateaus. c) The Fermi level lies between two Landau levels and the resistance becomes quantized again [17].

conductance (or σ_{xy})

$$G_{xy} = \frac{e^2}{h}\nu,$$

where $\nu = \pm 4\left(n + \frac{1}{2}\right)$. n is the (relativistic) Landau level index, the factor "4" accounts for spin and valley degeneracy and the sign of ν depends on the polarity of the carriers ("+" for electrons, "-" for holes). One of the biggest particularities is the presence of an electronic state at the Landau level which shares both electrons and holes in equal amounts (i.e., $n = \nu = 0$). It is called the zero mode of the Landau level spectrum and thus, it corresponds to a half-filled Landau level. The sequence of the transverse conductance plateaus in units of $4e^2/h$ evolve according to half-integer values of the filling factor ν accounting for the four-fold degeneracy. Hence the name *half-integer quantum Hall effect* in graphene (or also relativistic QHE).

The corresponding Landau level spectrum found from the transport results in graphene shown in Fig. 1.21 is also very different from the classical fermions. Solving the Hamiltonian under magnetic field and using the Peierls substitution, the energy spectrum of the Landau levels are derived:

$$E_N = \pm v_F \sqrt{2\hbar e N B}.$$

The DOS has already been shown in right of Fig. 1.8. As seen in the energy expression, a solution in $N = 0$ is possible and corresponds to the 0th mode Landau level. The dispersion at zero magnetic field reveals this 0th mode Landau level and the latter is doubly-degenerated in terms of valley, giving a half-filled level. The development of the individual levels are square root-dependent in terms of magnetic field B as well as level index N. Given this dependence and the energy dispersion typical in graphene $E \propto k_F = \sqrt{\pi n}$, the spacing between the maximum of ρ_{xx} in the relativistic QHE is constant over the density axis. This notably useful in a Landau map in a B-V_g where linear fits are easy to make through the maxima in ρ_{xx} from which the gate coupling of the device α can be determined for instance. Another particular aspect in graphene is that the quantum Hall regime was able to be observed even at room temperatures [25]. Indeed, compared to the Landau energy spectrum in conventional 2DEG systems, the cyclotron gap between the 0th Landau level and the 1st levels is quite large in graphene, caused by the square root-dependency. Hence, the thermal averaging possibly leading to filling states far away the Fermi level at room temperature was found to be not sufficient for preventing the formation of quantized plateau.

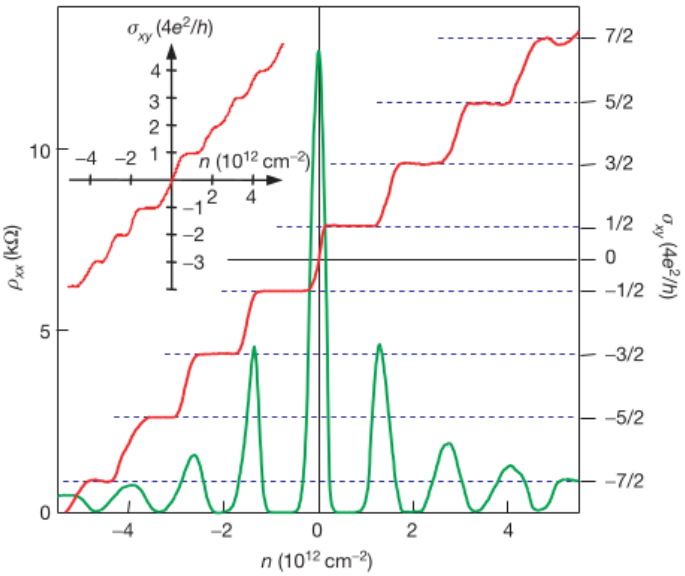

Fig. 1.21. Longitudinal resisitvity ρ_{xx} (green) and Hall conductivity σ_{xy} (red) as a function of carrier density n at $B = 14\ T$ and $T = 4\ K$. The transverse conductivity exhibits quantized plateaus following $G_{xy} = 4(N+1/2)$, where N denotes one Landau level index, while ρ_{xx} drops to zero. The inset shows the QHE in bilayer graphene where the quantization sequence is normal and demonstrates the uniqueness of the half-integer QHE in monolayer graphen [24].

Chapter 2

Samples, experimental setup and measurements

This chapter will focus on the description of the experimental part of the work. First, few words about the samples used for the transport measurements and the way one mounts them to to a sample holder will be given. Then, the working of the experimental system including the VTI and the cryogenic circuit will be described. The last step will be related to the electronic tools used for measuring signals associated with different types of transport characteristics in the devices as well as the parameters to play with in order to get reliable and resolved measurements.

2.1 Description of the samples and mounting on a sample holder

2.1.1 Samples

In order to make a comparative analysis of transport characteristics between encapsulated graphene and "bare" graphene (without encapsulation), two different samples were available for the transport measurements:

- The first device is coming from Aix-la-Chapelle in Germany and fabricated by the group of Christoph Stampfer with a similar fabrication method as in Ref. [5]. It consists of graphene encapsulated in between hexagonal boron-nitride (called sample A) with thickness 30 nm (for bottom hBN) which has been lithographically etched using Argon plasma such that it features a very small constriction of width $W^A = 340\ nm$ (see left of Fig. 2.1). The underlying hBN layer is 30nm-thick. The whole is deposited on top of a larger 300nm-thick insulating SiO_2 substrate, being itself on top a highly doped Si backgate. As can be seen in right of Fig. 2.1, six numbered metallic contacts are then deposited on the edges;
- The other device was fabricated by t he group of Prof. J. van de Vondel from KUL (called sample B) using a process similar to that used to produce the samples in Ref. [26]. It features a 8-contact Hall bar patterned in CVD graphene layer transferred on top of a 300nm-thick SiO_2 layer also on top of a doped Si substrate (see Fig. 2.2). The geometrical dimensions are given and specifically, a constriction is also lithographically patterned; its width is $W^B = 500\ nm$. The green square set at the tips of the Hall bar represents the 8 metallic contacts which are also numbered.

2.1.2 Bonding process

The characterization of the devices requires flowing current through the samples while probing specific potential differences. The bonding process allows to do this, and this step was realized at UCL. The working principle is to link each golden metallic contact deposited on the device edges to an end of a thin metallic wire. On the device side, the contacts are too thin but a corresponding far-off larger well-patterned surface is available for the bonding feasibility. The other end of each wire is bonded to a specific metallic pad of a sample holder used for controlling current injection and voltage probings between desired contacts through the device. The main objective is thus to electronically and physically

Fig. 2.1. (Left) AFM image of the etched hBN-graphene-hBN device with a 340nm-wide constriction (sample A). (Right) AFM image of sample A encompassed in red and showing six numbered metallic contacts (in yellow) each connected to its edges.

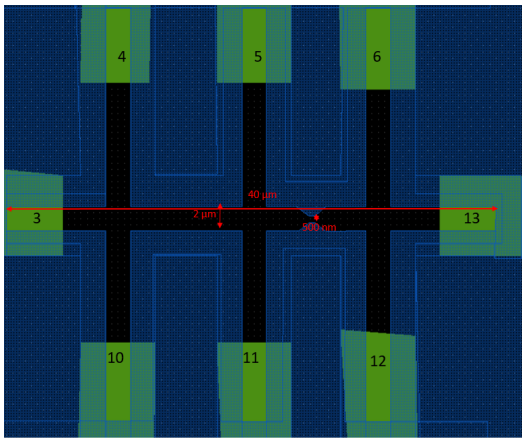

Fig. 2.2. Scheme of a graphene Hall bar device (in black) featuring a 500nm-wide constriction (sample B). The green rectangles located at each Hall bar arm tip correspond to metallic contacts which are numbered.

stick each sample on a chip. Here below is described the succession of steps to achieve the mounting of a sample on a chip using the bonding process:

1) Beforehand, the Si backgate must be also accessible by the chip in order to tune the carrier density in graphene. To do that, the SiO_2 insulator is scratched;

2) Then, the backgate side sample is deposited on the edges of the chip after after coating the latter with a conductive silver paint (paint from "Agar Scientific");

3) Before the actual bonding, it has to be ensured that all pads of the integrated circuit are safe, i.e., they must be at the same potential in order to avoid electrical shocks: a microweld was used to do this, to short-cut all the metal pads of the sample holders using a metal wire;

4) Now, the bonding process can be done. It also uses the microweld: a tip holding a very long and thin metallic wire stands above the support with the sample on the chip. The support is moved thanks to a mobile stage. Using a knob to hold and a microscope to check the tip position compared to the areas to connect, the tip shifts downwards and welds the wire on one contact pad linking between the welded wire on either the desired metallic contact or pad;

5) The tip is going back upwards by releasing the knob while holding the remaining wire linked to the welded part;

6) The same operation as 4) is repeated for the contact or pad corresponding to its already linked part via the wire. The bonding is thus achieved between the contact and the pad through the metallic wire and this is done for the backgate as well as all metallic contacts.

The next big step is the introduction of a single device in the experimental chamber and the establishment of conditions in temperature or/and magnetic field which can be tuned during the electronic measurements.

Before sending the samples into the experimental chamber, there is a need to carefully note the matching of the metallic contacts with their corresponding pad using a specific number. Indeed, each pad is linked with a pin (short metal rod) extended below the chip. All pins constitute a well-organized sequence to fit in an electronic support with a corresponding hole for each, all together making up a system with precise control of pins through which an electrical current can be applied, or a gate voltage and signal voltage be measured. Hence, this is important in order to know through which part of the samples the input signals are sent and the measurements are taken. More details will be explained in Section 2.3.

2.2 Description of the experimental system and setup

The transport measurements of the graphene samples must be operated from room to very low and stable temperatures in order to analyze potential signs of quantum effect such as the transport quantization due to the size of the nanoconstrictions. In addition, weak and strong magnetic fields should also be accessible to study other quantum effects like localization and Landau level quantization in the quantum Hall regime. These requirements can be met by the precise control of the sample temperature within a cryogenic system and by the use of a type-I superconducting magnet which can benefit from temperatures below its transition temperature due to that cooling system. Hereafter, details about the system and the way low temperatures are stabilized are described.

2.2.1 Cryogenic system

The system in which the measurements are done until weak temperatures can be seen in the photo of Fig. 2.3. The corresponding plan for an inside view is also shown on the same Figure. It consists of a large cylindrical vacuum chamber in which a centerpiece can penetrate through a vertical tube to access the magnetic field centre (denoted "FC" in the plan) provided by an integrated superconducting magnet at the bottom, while being cooled thanks to a flow of surrounding vapor ^{4}He at low pressure.

The centerpiece of the system is a *variable temperature insert* (VTI) which is a long cylindrical tubular structure whose one end contains a rod on which one sample can be mounted and inserted at the bottom of the cryogenic system for being measured [27]. The VTI also links the devices with the external electronic tools to control the measurement process. Also, it is highly useful because one can control and stabilize its position while going down until the field centre, which makes a way to probe the characteristics of the samples at different temperatures. These can go from 300 K down to 1.8 K.

In order to keep stable temperatures during the sample measurements, one needs to stabilize the cryogenic fluid's one, i.e., ^{4}He. A cryogenic circuit is defined and established through the system in order to fulfill this objective. The circuit can be seen in Fig. 2.4. As depicted, it is closed to allow fluid's recycling. An important aspect of the cooling process is the cryostat: it consists of a cryogenic bath of the liquid fluid (here ^{4}He) at a very low constant temperature. This part corresponds to the Helium pot in the picture and its base temperature is 1.8 K. It lies inside a large vacuum chamber in order to avoid parasitic heating from the surroundings which could increase the base temperature. Gaseous ^{4}He at high temperature is stored into a vessel on the left with a pressure gauge which can be read to determine whether the amount of fluid needed for the cooling process is sufficient. Then, the gas is injected into the vacuum wall through the Helium inlet prior to going through two heat exchanger stages which are the key part to lower the fluid's temperature down to 1.8 K and transforming the latter into the liquid state. This is how the cryogenic bath is filled in the Helium pot. The next step is the actual cooling of the device mounted on the VTI fully or partially inserted into the vacuum block within the tube. The principle is to cool the sample using cooled ^{4}He vapor rising in the tube before being salvaged by a scroll pump. The vapor is generated using the needle valve which allows the flow of ^{4}He from the Helium pot through the heat exchanger at the very bottom of the VTI sample access. On one hand, the pump is necessary to maintain the ^{4}He flow cycle; on the other hand, its power allows to prevent the temperature of the gas from increasing due to the low vapor pressure for which a decrease lowers the temperature

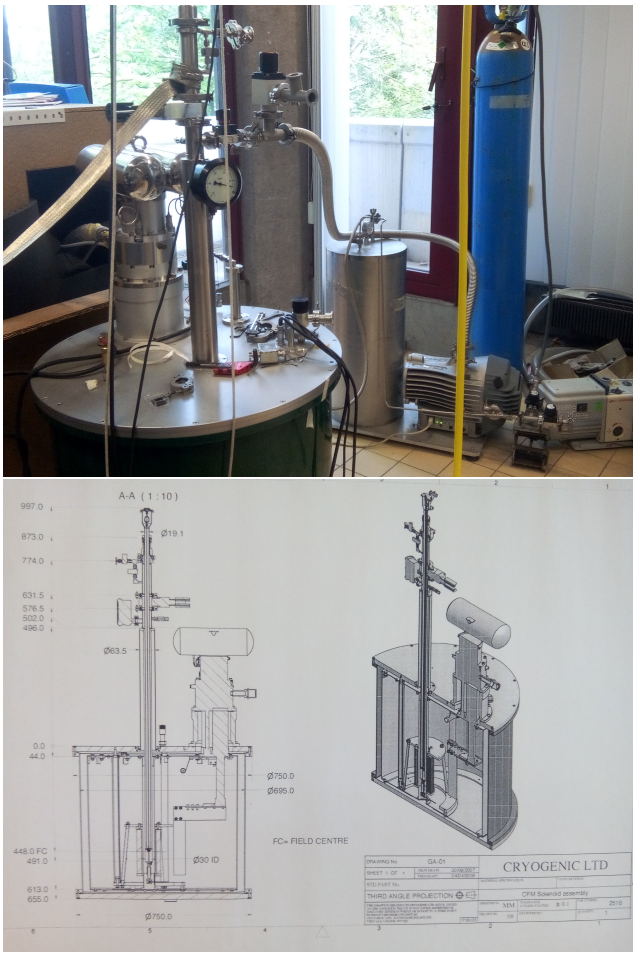

Fig. 2.3. Up: Photo of the cryogenic system. Down: Plan of the cryogenic system.

according to the Clausius-Clapeyron's law. However, the rate of liquid ^{4}He flowing towards the VTI sample access must be also taken into account because it also contributes to the pressure of the ^{4}He gas: the rate is controlled by the needle valve with a high precision. A compromise about this quantity should be established: if it is too low, the Helium pot could be overloaded and the flow not be steady; if it is too high, the pressure of the gas in the VTI sample access would increase, so would do the vapor pressure at the liquid/gas interface which is associated with an increase of temperature. Finally, the stabilization of the temperature of the sample in the tube depends on all these considerations and the parameters can be monitored by looking at the temperature of the pot read on a panel, provided by the thermally-linked Cernox thermometer (see again Fig. 2.4) and at the pressure gauge of the ^{4}He gas connected to the VTI sample access (seen in Fig. 2.3).

2.2.2 Setup

Once the cooling process is launched, the temperature of the pot decreases with time and reaches its base temperature (1.8 K) and the pressure of the ^{4}He gas in the VTI sample access is determined according to the chosen configuration of the needle valve ($\sim$ $mbar$). The VTI with one sample attached to the support pointing downwards can be then inserted into the tube. One pad of the electronic support gives access to the backgate material of the sample and allows the tuning of the carrier density in the hBN-graphene-hBN by applying a backgate voltage V_g using a voltage source control. The measurements (details will be presented in Section 2.3) can already start to get information about the temperature-dependent transport from room temperature to 2 K by sweeping a range of cyclic V_g values. To achieve this, it needs to regularly lower the VTI while recording the data and be sufficiently slow in order to smoothly decrease the temperature in the VTI sample stage read on the same panel as the 1.8K-pot one. The other way around is of course feasible. No magnetic field was applied during this step. Once the sample on the VTI is located within the field centre of the cryogenic system at the lowest reachable

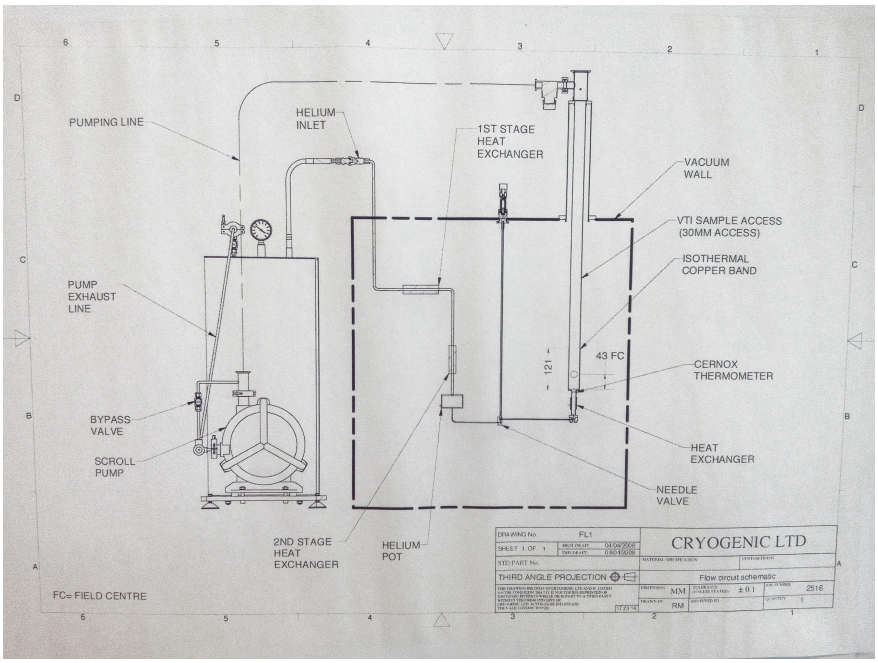

Fig. 2.4. Plan of the cryogenic circuit of flowing ^{4}He to make a cryostat and to allow stable temperatures during the measurements.

temperature (i.e. $T = 2\ K$), the measurement process can stop. After that, a current injection can be sent along the superconductor wire with a careful increment in order to generate an increasing perpendicular magnetic field to the sample plane and then, stabilize the current to keep the field fixed. In practice, a maximal increment of 0.5 T/min was highly advised, otherwise the current increment would have dangerously increased the superconductor temperature too quickly compared to the stabilization brought by the cryogenic fluid and the superconducting state could have been lost for a disaster. A magnetic field strength up to $7 - 8\ T$ for both devices is reached. Finally, from that point, the measurements can start again by a sweeping V_g and an extremely low incremental decrease to zero field (namely -0.008 T/min) is implemented to get sufficiently resolved measurements in magnetic field. The counterpart is just that no measurement at fixed field values was done.

2.3 Electronic tools and measurement system

2.3.1 General operation principles

The measurement system in the lab allows to collect data by probing parameter-dependent (quantum) transport characteristics which can be inherent to the devices and therefore, faithful to their proper electronic properties. Particularly, the QPCs conductance in the mesoscopic regime is important to investigate. All essential electronic devices and tools being for the measurements are shown in Fig. 2.5. From there, refer the text color of the different parts to the corresponding color of each box for their localization.

The working of this system is based on the voltage drop signals V_{ij} measured between two metallic contacts i and j using a controlled current I_{kl} through the devices injected from contact k and evacuated to contact l (towards the ground). The choice of biasing the current instead of the voltage across the measured devices is justified by their expected resistance value range which is in the order of $h/e^2 \sim 26\ k\Omega$. Resistors with much higher resistances ($\sim M\Omega$) are available and if one is put in series with either of the samples, the measured current will be only dependent on the known resistance of the larger resistance. To generate a polarization current with a precise control, a low-frequency (namely 77 Hz) AC voltage with a specific oscillation level V_{AC} (see after) is applied and the current is measured using a lock-in amplifier. The expected current going through the samples is found easily: $I = V_{AC}/R$, where R is the high resistance of the resistor in series with either sample.

The principle of the measurement using the lock-in technique consists in electronically preamplifing and realizing arithmetical operations on input signals to generate output ones. The main characteristic

of input signals is their noisy fluctuations with time. In order to get correct outputs, the lock-in amplifier will multiply the noisy signal(s) by a pure cosine function which has to exactly oscillate at the working frequency with the corresponding amplitude and the result will undergo a low-pass filtering operation in order to get rid of the parasitic frequencies coming from the noise. This principle is a powerful way to read and extract single output values which best correspond to the amplitude of the oscillation associated with the measured quantity, while a variable is applied to the real system (the gate voltage and/or the magnetic field). The time of computing of the lock-in devices can be chosen by modulating their time constant τ_c. It gives a compromise between the real time taken for computing the outputs and the computation accuracy. In addition, a value associated with the sensitivity s allows to amplify the output values sent on a reading panel which will serve to collect and plot the raw data. These parameters cannot be arbitrarily chosen but more will be explained a bit further.

In order to probe intrinsic transport characteristics of the devices, i.e. without involving the contact resistances, the *4-probe method* is used: it allows to to get rid of the contribution of contact resistance by using a combination of four different contacts at least, which is feasible for both samples A and B as shown in right of Fig. 2.1 and Fig. 2.2. In that specific case, the intrinsic transport characteristic such as the resistance $R_{ij,kl}$ equals to the ratio between the corresponding real voltage drop V_{ij} by the current I_{kl}, where $i \neq j \neq k \neq l$ denote 4 different contacts. Possibly, at least 5 available contacts allow to simultaneously probe two distinct transport characteristics still using the 4-probe method. The voltage drop is also measured with a lock-in device.

The resulting measurement configuration (black box in Fig. 2.5) is based on different numbered switches linked to the available contacts. This numbering is important because it must correspond to the same one done for the contacts of the samples, hence the carefulness of mounting the devices in the right orientation to the support of the VTI. That way, it is possible to connect the cables to the right switches to properly measure across the required contacts. A switch going up means that an electronic excitation is sent into or out of the samples, important for detecting the voltage drop signals and injecting current; a switch going down corresponds to the ground, notably important for evacuating the injected current. Anyway, a comparison between the numbered contacts of sample A in right of Fig. 2.1 and switches in Fig. 2.5 can be done to understand what is exactly measured. Note that the 7th switch (not seen in the AFM image of sample A) is linked with the voltage source control and thus connects to the backgate when the switch is up.

In addition, the output signals on the reading panels could display too much noisy fluctuating digits, explained as follows: the electronic system in the VTI linking the measured sample has missed filtering tools which could have been present to efficiently produce cleaner signals before sending them to the lock-in. A solution to that is to use a voltage amplifier that will already filter the output signal (corresponding to the voltage difference in this case) prior to the treatment process through the lock-in amplifier. At low temperatures ($\sim 2\ K$ here), filtering the signal as an input allows to retain information. The filtering can be either low-pass, high-pass or band-pass type with a specified gain g to amplify the measured signal.

The control of the system of measurements is done from a computer using a software called *LabVIEW*, which allows to program through a graphical interface. In this specific context, it is possible to read and write all needed data in files such as temperatures, variables (gate voltage and magnetic field) and the measurements themselves displayed on the reading panels (voltage difference signals). The polarized current can be also computed in order to check its expected steady value. Meanwhile, a real-time interactive view of the raw data (voltage drops) as a function of the gate voltage only is possible to qualitatively describe whether the expected evolution is fulfilled and whether all parameters are well chosen (see downafter for more). As mentioned before, the gate voltage applied on the backgate is tuned by the voltage source control. This is remotely realized using the LabVIEW software itself. Before the start of the measurements, a minimum and maximum values of V_g has to be chosen, with a specific voltage step (in V) and a step time (in s) thus between two successive steps. When V_g is shifted to the minimum value, the program starts and V_g progresses toward the maximum one at the specified rate described by the step and the step time. If desired, the program can stop to get a single sweep. However, when the magnetic field varies, a cyclic sweep is needed: the data recording is temporarily off after one complete sweep. Then the gate voltage can get back to the minimum value at a much higher rate than the one established during the measurements, before starting again the recording using another time parameter. The latter is chosen such as the recording does not restart during the fast gate voltage return. Finally, the program can stop by setting a final reachable value of the varying magnetic field.

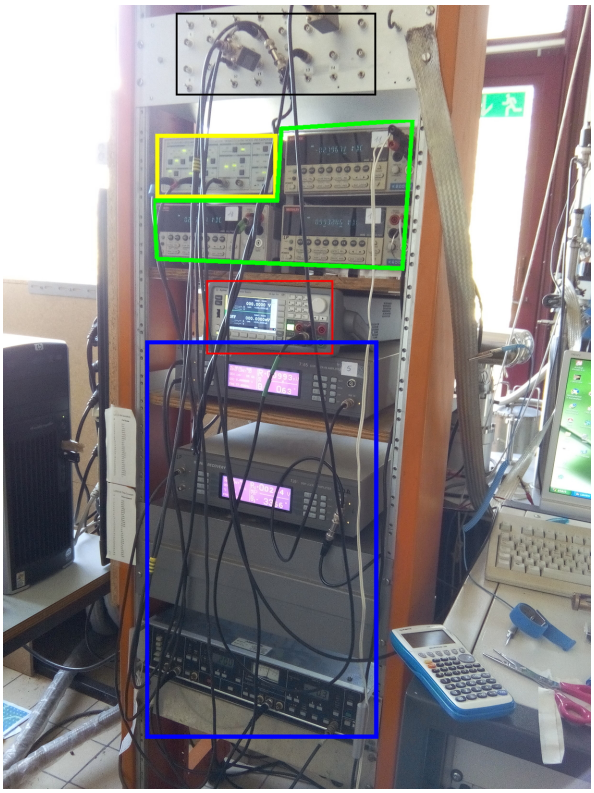

Fig. 2.5. Photo of the electronic devices. Blue box: lock-in devices; red box: gate voltage source control; green box: output reading panels; yellow box: voltage amplifier; dark box + major attached cables to the lock-in: measurement configuration.

2.3.2 Considerations about the measurement parameters

Choosing appropriate parameter sets is very important to get exploitable and reliable data. Brief comments about the the parameter choices are given below.

- The injection current I should not too high for not heating up the cold charge carrier system due to the dissipation heat of the sample described by the dissipation power proportional to I^2: $P_w = I^2 r$, where r is the resistance of the sample. If P_w is lower than the thermal energy kT, then the temperature of the system won't rise. During the measurements using a high resistance of 10 $M\Omega$, the excitation voltage oscillating at a typical frequency of 77 Hz had mainly an amplitude $V_{AC} = 0.2\ V$ to give $I = \frac{0.2\ V}{10\ M\Omega} = 20\ nA$. Smaller values of I should also be excluded to avoid too much noise in the measurements;

- The time constant τ_c of the lock-in amplifiers defines the lock in integration time. There is to be a compromise in order to have not too noisy data while not taking too much time for generating them. In the experiment, τ_c was mainly set to 500 ms;

- The sensitivity s of the lock-in corresponds to the amplification of the signal which will be consequently measured (in V). Its value must be chosen so that the measured signals do not exceed 12 V which is the saturating value of the Keithley voltmeters on which the lock-in output signals are displayed. The sensitivity has to be taken into account for the real value computation. For instance, if $s = 1\ mV$, thus one knows that the measured signal will be the real value times 10^3 (or conversely 10^{-3}). In addition, a factor 10 was also considered because the scale of the lock-in usually worked until 10 V;

- If a signal is already going through a voltage amplifier prior to the lock-in amplifier, the gain g must also be multiplied to the output signals for computing the real values;

- The range of the gate voltages to sweep must be chosen in order to observe various characteristics of electronic transport such as a low-density and high-density regimes as well as several Landau level developments at high magnetic fields;

- The time step between two successive gate voltages should not be too high in order to optimize the total time of data acquisition. But most especially, it should not be too low compared to the time constant τ_c of the lock-in devices. Indeed, each data point successively displayed on the computer screen using LabVIEW corresponds to the chosen time step but the self-closest points must be well correlated between each other in agreement with the time (determined from τ_c) taken for generating the output values from the lock-in amplifiers.

2.3.3 Description of the main transport characteristics

Sample A Referring to the numbering of the metallic contacts as can be noticed in Fig. 2.1, the current injection (20 nA) was made from contact 11 to contact 5. Two different potential difference signals V_{ij}, where i and j denote the indices of the contacts as probes, were simultaneously measured to probe transport characteristics of the device:

- The longitudinal resistance $R^A_{11(5),12(13)} = \dfrac{V_{12,13}}{I_{11,5}} = R^A$ (or $1/G^A$) across the constriction between contact 12 and contact 13. The positive terminal of the voltage is located in the vicinity of the device where the current goes into the sample (so near contact 11). Hence, the voltage reading for the measurements has been set to A-B, where A corresponds to contact 12 and B to contact 13 for getting positive values;

- The transverse (or Hall) resistance $R^A_{11(5),12(10)} = \dfrac{V_{12,10}}{I_{11,5}} = R^A_{xy}$ (or $1/G^A_{xy}$ in the low B-field regime or $G^A_{xy} = \dfrac{R^A_{xy}}{R^{A^2}_{xy} + R^{A^2}_{xx}}$ in the high B-field regime) behind the constriction between contact 12 and contact 10.

Measurements were first realized at zero magnetic field and different temperatures down to $\sim 2\ K$ (R^A_{xy} is irrelevant in this case). Then, mapping of the different resistances were acquired while varying two parameters: the magnetic field and the back gate voltage. Regarding the slow decrease of magnetic field B, it was realized from $B = 7\ T$ to $0\ T$ and meanwhile from $V_g = -5\ V$ to $23\ V$ at $\sim 2\ K$. Each complete gate voltage trace roughly corresponds to a field decrease of $0.2\ T$.

Sample B Referring to the numbering of the metallic contacts as can be noticed in Fig. 2.2 (right), the current injection (20 nA) was made from contact 3 to contact 13. Three different potential difference signals were simultaneously measured to probe transport characteristics of the device:

- The longitudinal resistance $R^B_{3(13),3(11)} = \dfrac{V_{3,11}}{I_{3,13}} = R^B_{HB}$ (or conductance G^B_{HB}) across the Hall bar without the constriction between contact 3 and contact 11. Since contacts 4 and 10 were not working, the measurement is therefore a 3-point one in this exceptional case and thus, the resistance of contact 3 must be taken into account. However, this contact resistance has not been experimentally measured;

- The longitudinal resistance $R^B_{3(13),56} = \dfrac{V_{5,6}}{I_{3,13}} = R^B_{QPC}$ (or conductance G^B_{QPC}) across the constriction between contact 5 and contact 6;

- The transverse (or Hall) resistance $R^B_{3(13),5(11)} = \dfrac{V_{5,11}}{I_{3,13}} = R^B_{xy}$ (or $1/G^B_{xy}$ in the low B-field regime or $G^B_{xy} = \dfrac{R^B_{xy}}{R^{B^2}_{HB} + R^{B^2}_{xy}}$ in the high B-field regime) behind the constriction between contact 5 and contact 11.

Measurements were realized at zero magnetic field and different temperatures down to $\sim 2\ K$ (R^B_{xy} is irrelevant in this case). Then, mapping of the different resistances were acquired like in sample A. Regarding the slow decrease of magnetic field B, it was realized from $B = 8\ T$ to $0\ T$ and meanwhile from $V_g = -10\ V$ to $42\ V$ at $\sim 2\ K$. Each complete gate voltage trace roughly corresponds to a field decrease of $0.25\ T$.

Chapter 3

Analysis of low temperature transport in QPCs

This final chapter will cover the most essential aspects of the work. The main objective here will be to describe, analyze and understand the results extracted from the data coming from the electronic measurements on both samples as much as possible. The collected data are treated such that relevant plots are made to describe the electronic properties of the devices. Given their peculiar features and the experimental conditions (low temperatures and presence of a magnetic field), one will focus on quantum effects. Several theoretical models will be used to evidence the eventual transport phenomena and device characteristics. Comparisons with other works found in literature will possibly help to identify the contributions from different parameters. In addition, some simulations using Kwant software will be provided in order to verify the hypotheses suggested about the understanding of one experimental result.

This chapter will be divided into three main sections. The first one will correspond to the general characteristics of the devices as well as their main resulting electronic properties such as the gate lever-arm, temperature-dependent conductance at zero magnetic field with a better focus at the lowest temperature. Finally, a brief demonstration of the typically-observed quantum Hall effect at high perpendicular fields will be given. The second section will be about a deeper study of the conductance evolution associated to the nanoconstrictions under zero or weak magnetic fields. To be precise, a tentative of finding size quantization signatures will be done. Then, a model dictating the evolution of conductance within a Landauer approach will be employed to investigate the impact of disorder on transport through the nanoconstrictions. The final section will focus on the high field regime and will tell about peculiar features which go beyond the simple description of the half-integer quantum Hall effect in graphene such as degeneracy lifting whose origin should be explained.

3.1 General characterizations

3.1.1 Hall measurements, Landau fans and gate lever-arm extractions

One important device characteristics to determine is the capacitive coupling between the graphene sheet and the underlying backgate used for the carrier density tuning. The application of the gate voltage V_g will basically influence the type and the density of charge carriers contributing to transport. The gate voltage is linearly related to the bulk carrier density n with a proportionality factor which is the gate lever-arm (or the capacitive coupling) α:

$$n = \alpha(V_g - V_{g0}), \tag{3.1}$$

where V_{g0} is the gate voltage at the charge neutrality point (CNP), which corresponds to the exact compensation between electron and hole doping levels. The latter relation will be used to convert V_g to n in following figures.

There are two common ways to experimentally estimate α: one based on the evolution of the Hall (or transverse) resistance at rather weak perpendicular magnetic fields [17] and the other based on the Landau fan development as a function of the gate voltage and magnetic field [22]. Both methods have been employed as well as the following comparison with theoretical values. At the same time as extracting α, discussion based on the low B-field Hall and longitudinal resistance measurements as well as on the Landau fans will be done:

- Within the 2D classical Hall model, the evolution of the transverse resistance R_{xy} in a Hall bar is linear with the magnetic field B and depends on the carrier density n:

$$R_{xy} = \frac{B}{ne}.$$

The principle is to plot the data describing the evolution of R_{xy} as a function of B, for different values of V_g. The different data sets can then be approximated by a linear fit from which one can extract the slope $\frac{1}{ne}$ from the latter relation, and so n itself. Note that it does not apply at $n = 0$ since a divergence is theoretically expected but actually, there is still a finite carrier concentration at the CNP due to electron and hole puddles dominating in the low-density regime. Hence, there must be a continuous sign change from $n < 0$ to $n > 0$. Finally, the different carrier density values can be plotted on another graph in function of the corresponding values of V_g from which the slope thus already corresponds to α_{exp1}, where "1" denotes this first extraction method.

Fig. 3.1 illustrates it for sample A at 2 K. Most of R^A_{xy} data sets are well aligned to be legitimately fitted with a straight line. The linear fit to the extracted carrier densities n in function of V_g gives $\alpha^A_{exp1} = 8.9 \cdot 10^{10}\ cm^{-2}V^{-1}$. Note that two data points corresponding to $V_g = 7$ and 10 V are considered as outsiders as they are not well aligned with the other and correspond to overestimated values of n according to the fitting line. Looking at Fig. 3.2, the values of gate voltage belonging to the outsiders lie in a fluctuating region at the top of the longitudinal resistance R^A at $B = 0\ T$. These (mesoscopic) fluctuations are explained later but one can already try to identify a value of the associated charge neutrality point (CNP), which is defined as the point for which there is exact compensation between hole and electron charges. Since there are pronounced fluctuations which result from an extrinsic characteristics (see later), the CNP is not necessarily at the very maximum value of R^A. One way to extract it is to consider the corresponding conductance $G^A = 1/R^A$ and fit its linear parts far from the CNP on both hole and electron sides. The linear fits can be then extrapolated until their crossing which indicates a good estimation the CNP. Fig. 3.8 illustrates this and the CNP is found to be roughly $V_{g0} \sim 8\ V$. As a consequence, the outsiders lie close to the charge neutrality point (CNP). However, note that the fits were done by linear regression and especially over the quite chaotic evolution on the electron side. Hence, the CNP could not be so precise and not the exact one.

However, the outsiders were determined by Hall measurements and they are linked to R^A_{xy}. In Fig. 3.2, one sees a striking feature: the gate voltage associated with the sign change in R^A_{xy} ($\sim 5\ V$) does not correspond at all to V_{g0} from the CNP previously found. Yet, the sign change in the Hall resistance is also a way to extract the CNP of the device. Therefore, this big difference cannot be neglected and must be explained to understand the results. This is something which was not found in literature but one can state some hypotheses to justify this pronounced shift in sample A. In graphene, the location of the Dirac point (or the CNP) depends a lot on disorder and charge impurities. Notably, the strength of potential fluctuations mostly depend on the density of electron-hole puddles which dominate transport at the low-density regime. A stronger doping in one or the other carrier type will lead to the shifting of the CNP (towards positive voltages for a residual doping in holes, negative for electrons) caused by these fluctuations. If the device has a sufficiently homogeneous potential landscape, the CNP may be found to be identical whatever the way it is obtained. However, if the device is subjected to numerous charge inhomogeneities with different local potential fluctuations and density, it is likely possible that transport won't be affected the same way everywhere, i.e. there is a strong local dependency. In sample A, the presence of inhomogeneities might be responsible of the shift between the sign change in R^A_{xy} and the CNP from R^A. That way, two different CNPs are depicted and one is not necessarily more relevant than the other because a physical explanation behind the collected results can be stated.

In particular, in sample A the measurement of R^A_{xy} depends on electronic paths behind the constriction, whereas the measurement of R^A is realized via paths through the constriction itself. During the measurement period, sample A must have been pulled out of the cooled chamber because of an issue with very low temperature reaching. Unintentionally, the sample was subjected to a cool-down process by being afterwards exposed to air during at least 10 days before being once again inserted in the cryogenic system and being measured. With time, some species could get access to the edges (especially around the constriction) and develop chemical modifications that would change the local residual doping of graphene, as reported in Ref. [5]. The graphs that are mostly shown (except the ones taken at higher temperatures than 2 K) correspond to the measurements after

the cool-down. Hence, the extra addition of charge impurities around the constriction compared to the surroundings and combined with the fact that carriers are notably strongly interacting near the edges in relatively small constriction may explain farther CNP associated with R^A instead of the CNP with R^A_{xy} (i.e. at the sign change), because of inhomogeneities which result in different strength of interactions close to the CNP depending on the probing transport.

In Fig. 3.3, several traces of R^A_{xy} at different magnetic fields (including the trace in Fig. 3.2) each also show a pronounced shift of their own CNP/sign change compared to the CNP of R^A but with a surprisingly observation: as the magnetic field increases, the CNP of R^A_{xy} moves to the right and closer to the CNP corresponding to R^A. Again, such case did not have been found in literature and another suggested hypothesis can be settled. As long as the perpendicular magnetic field increases, the cyclotron radius $l_c \propto 1/B$ (at constant density n) of the carriers decreases and with the induced Lorentz forces, the carriers flow in more reduced zones along with accumulation towards the edges mostly in the wider region than in the constriction. Since higher electronic density is believed to be located near the edges (mainly caused by the cool-down process) than in the bulk, a local shift of the CNP is possible due to inhomogeneities distinguished at the boundaries in comparison to the bulk. However, the residual doping near the edges out of the constriction is believed to be less important than in the constriction where interactions with the edges are more dominant. In addition, Fig. A.1 shows the evolution of the shift of the CNP associated with R^A_{xy} at increasing magnetic fields up to $\sim 7\ T$. One sees that the CNP moves until to be stabilized just below $V_g = 7\ V$ for the highest magnetic fields. More precisely, it is observed that the displacement stops around $B = 3\ T$.

Back to the classical Hall effect, Fig. 3.3 shows that the B-field dependence is linear at constant V_g with lower spacing as V_g (or n) is farther away from the sign change location, except around the sign changes themselves, which is explained by finite carrier density caused by residual doping at the associated CNP (and domination of electron-hole puddles). Thus, instead of computing zero density in the case of a divergence, a finite density may be determined with also a lower even spacing of R^A_{xy} as B linearly increases. Yet, it has to be noticed that these density close to the CNP do not physically reflect the dominating type of carriers as a two-type carrier transport is favoured in the low-density regime [8]. Anyway, it nonetheless demonstrates the slope being proportional to $1/n$. Also, the two outsiders which were mentioned and shown in right of Fig. 3.1 are not close to the CNP of R^A_{xy} despite their overestimated computed density. The fact that they rather lie close to the CNP corresponding to R^A can anyway explain this result. Indeed, one common contact is shared between both transport characteristic measurements (i.e. contact 12 in right of Fig. 2.1). Hence, common electronic paths from both contributions at weak magnetic fields might give some similar results in the low-density regime like residual doping. In addition, note that the sign of the increasing transverse resistance with B is positive on the left, which should give positive values of n (corresponding to electrons) whereas one lies on the hole side. But the measurement conditions can produce the reversed results due to the choice of the two terminals across which the voltage difference is probed. Hence, these results are the real ones just with the opposite sign.

The same procedure has been applied regarding sample B in Fig. A.5. There is one outsider (at $V_g = 19\ V$) close to the CNP of R^B_{HB} (and R^B_{QPC} being very close, i.e. at 17.5 V) which lies at $\sim 17\ V$ as can be noticed in Fig. A.6. Unlike in the sample A case, one can see there that the sign change in the transverse resistance is well lying with the CNP of the corresponding longitudinal resistances, suggesting highly reduced charge inhomogeneities in the sample. This makes the carrier density extraction using this method more adapted since the zero carrier density following the fit in right of Fig. A.5 corresponds to the CNP. Finally, the gate lever-arm in this case amounts to $\alpha^B_{exp1} = 7.48 \cdot 10^{10}\ cm^{-2}V^{-1}$;

- The development of Landau levels at high magnetic fields under the shape of a Landau fan is also another way to extract the capacitive coupling α_{exp2}, where "2" denotes this second method. To discover the details of its extraction, refer to Appendix B which explains in addition a suggestion to improve the method described in the inspired article (Suppl. Notes of Terrés *et al.* article [5]).

  Starting with sample B, Fig. 3.4 presents colormaps of R^B_{HB} (left) and R^B_{QPC} (right) as a function of V_g and B. Since the measurements were taken at simultaneous varying gate voltage and magnetic field, an interpolation function has been implemented to create a full grid of data points (as if one sweeps one variable while the other is fixed and so on for other fixed values) generating these images. In both cases, a Landau fan is clearly observed, with linear dispersions along minima and maxima of resistance at high magnetic fields. The white lines whose origins are located at the Dirac

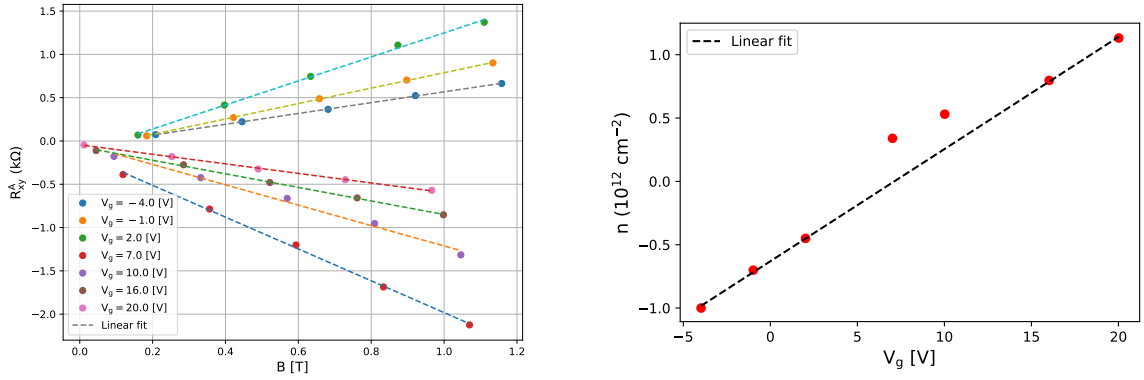

Fig. 3.1. (Left) Evolution of the Hall resistance R^A_{xy} with magnetic field B for different back-gate voltage values V_g. The dashed lines are linear fits according to the Hall resistance expression in 2D (see main text) in order to determine the carrier density n. (Right) Data set collected from the computed carrier density from the left plot with respect to each back-gate voltage value (sample A). The linear fit only goes through the most reliable dots. The steepness gives one of the two experimental values of the gate lever-arm α^A_{exp1}.

point roughly follow maxima of resistance at the Landau levels. Between the strips of resistance maxima, eye-guide small blue lines indicate the filling factors through the darker strips (i.e. minima corresponding to fully filled Landau levels in case four-fold degeneracy). An approximate value of the gate-lever arm α^B_{exp2} between the graphene sample and the backgate is determined by fitting the white straight lines as best as possible to the loci of maxima through the relation

$$B = \frac{h\alpha}{4eN}(V_g - V_{g0}),$$

where N is the Landau level number and V_{g0} the gate voltage at the charge neutrality point ($\sim$ 17 V). The approximate experimental value is identical in both cases and is $\alpha^B_{exp2} \approx 7.5 \cdot 10^{10}\ cm^{-2}V^{-1}$.

Regarding sample A, corresponding Landau fans are pictured in Fig. 3.5 with notably the red fitting lines (left map) best located at the resistance maxima for the first four Landau levels on each side (excluding the 0th mode). Using the B-field dispersion at the Landau level locations in function of V_g, one finds $\alpha^A_{exp2} = 1.1 \cdot 10^{11}\ cm^{-2}V^{-1}$. The right Landau level map is a better view[1] than the left one in the B-n plane and with the corresponding filling factors between Landau levels. One well sees the three first Landau levels plus the 0th one. The thick red circle is showing a peculiar aspect of the Landau fan but it will be discussed in a coming section.

The capacitive coupling is physically depending on the substrate dielectric materials and their thickness under the 2DEG since, as its name means it, a gate voltage applied on the backgate attracts charges from the 2DEG at the surface of the plate of the dielectric material into contact, inducing a capacitive effect. A theoretical expression of the gate lever-arm exists and can be also applied to two different juxtaposed dielectric materials on the plate surface into contact (equivalent to capacitors in series):

$$\alpha_{th} = \frac{\epsilon_0}{e}\frac{1}{\frac{d_{mat1}}{\epsilon_{mat1}} + \frac{d_{mat2}}{\epsilon_{mat2}}},$$

where ϵ_0 is the vacuum permittivity, e the electronic charge[2], d_{mati} the thickness of material i and ϵ_{mati} the relative permittivity of material i [28].

Considering the 300nm-thick SiO_2 dielectric layer as well as the 30nm-thick hBN dielectric layer between graphene and the backgate in sample A, the corresponding dielectric constant $\epsilon_{SiO_2} = 4$ and

[1] It is produced by a mathematical trick by generating the map in the logarithmic scale along with a more suitable colorbar.

[2] $\epsilon_0 = 8.854 \cdot 10^{-12}\ A^2s^4kg^{-1}m^{-3}$ and $e = 1.602 \cdot 10^{-19}\ C$.

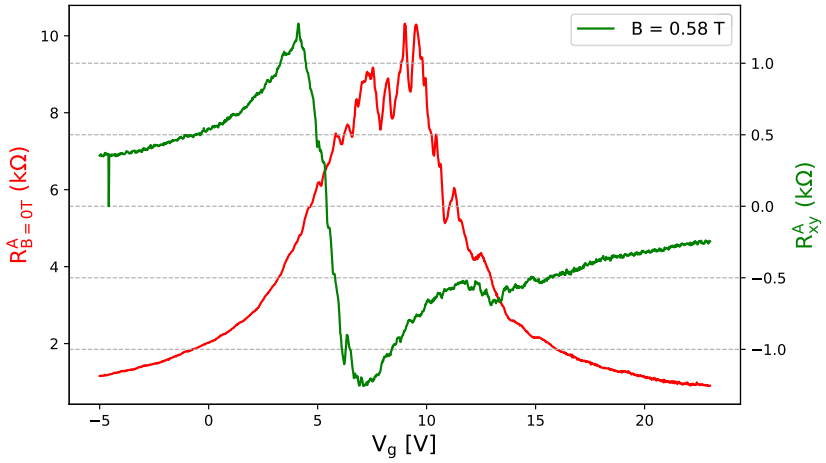

Fig. 3.2. Transverse resistance R^A_{xy} under non-zero magnetic field and longitudinal resistances R^A at zero field plotted as a function of gate voltage V_g. One sees a clear shift of the sign change of R^A_{xy} at the left compared to the CNP characteristic of the longitudinal resistance ($\sim 8\ V$). The B-label is the real value at the middle of the trace close to the CNP.

$\epsilon_{hBN} = 3 - 4$ [2] (say 3 here), the theoretical value is

$$\alpha^A_{th} = \frac{\epsilon_0}{e}\frac{1}{\frac{d_{SiO_2}}{\epsilon_{SiO_2}} + \frac{d_{hBN}}{\epsilon_{hBN}}} = 6.36 \cdot 10^{10}\ cm^{-2}V^{-1}.$$

In the case of sample B, there is only the 300nm-thick SiO_2 substrate and the corresponding gate leve-arm is $\alpha^B_{th} = \frac{\epsilon_0}{e}\frac{\epsilon_{SiO_2}}{d_{SiO_2}} = 7.37 \cdot 10^{10}\ cm^{-2}V^{-1}$.

All computed values of the capacitive coupling are reported in Table 3.1. The most striking observation is the really good concordance of all α values between experiment and theory in sample B, whereas a clear generalized discrepancy can be noticed in the case of sample A.

	$\alpha_{exp1}(cm^{-2}V^{-1})$	$\alpha_{exp2}(cm^{-2}V^{-1})$	$\alpha_{th}(cm^{-2}V^{-1})$
Sample A	$8.9 \cdot 10^{10}$	$1.1 \cdot 10^{11}$	$6.36 \cdot 10^{10}$
Sample B	$7.48 \cdot 10^{10}$	$7.5 \cdot 10^{10}$	$7.37 \cdot 10^{10}$

Table 3.1: Values of the experimental and theoretical capacitive couplings α for both samples.

To understand this specificity, one can attempt to make hypotheses based on the influence of source and effect of disorder in graphene on substrate like discussed before. A strong indicator may be seen in the quality of the Landau maps, for which the Landau level strips are more resolved in sample B than in sample A (Figs. 3.4 and 3.5 respectively). More over, the pronounced shift between the sign change of R^A_{xy} and the corresponding CNP is insignificant in case of sample B, which translates less domination of transport by inhomogeneities. Even though sample A represents encapsulated graphene using a hBN stack on Si/SiO_2, it already features technically less stable and conventional transport signatures mainly due to charge impurities and marked inhomogeneities at different edge regions (in and out of the constriction) and in the bulk.

For these reasons, the discrepancy of the gate lever-arms α^A_{exp1} and α^A_{th} in sample A can be argued even if no deeper explanation has been currently found. Also, the discrepancy associated to the highest value, i.e. α^A_{exp2} (Landau fan method), from the other ones is also quite difficult to concretely explain. But this use of value will be globally consistent with the right locations of the filling factor ν in the quantum Hall regime as explained a little bit further. This shows the correctness of the corresponding extraction method. To go further, capacitive couplings found regarding the different ballistic constriction-featured hBN-graphene-hBN devices in Terrés' thesis [22] vary from $5.4 \cdot 10^{10}$ to $7.15 \cdot 10^{10}\ cm^{-2}V^{-1}$, clearly closer to the theoretical value α^A_{th} with rather similar dielectric thicknesses. Hence, it does not seem that the

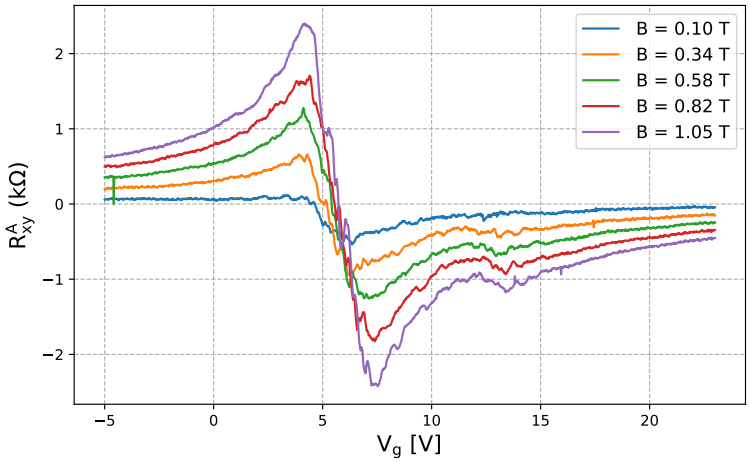

Fig. 3.3. Transverse resistance R^A_{xy} plotted as a function of gate voltage V_g at increasing magnetic fields B. The magnetic field labels indicate the real values at the middle of the traces (close to the CNP at $\sim 9\ V$).

etched underlying hBN layer along with the simple definition of the constriction is responsible for the deviation from the theoretical value in sample A.

Regarding sample B, all α^B values are in very good agreement with each other. The Landau maps in the constriction and Hall bar cases are much better resolved and qualitatively identical in terms of the Landau level evolution (Hall bar and constriction cases), which shows that the gate lever-arm is not necessarily affected by the presence of the constriction. More over, the insignificant shift between CNP for R^B_{xy} and CNP for R^B_{QPC}/R^B_{HB} in sample B suggests to more safely rely on the gate lever-arm extraction using the Hall measurements, confirming the good concordance with α_{exp2} using the Landau development method.

To conclude, the above-mentioned hypothesis of inhomogeneities possibly responsible of the peculiar CNPs shift in sample A have been used to make simple simulations. The simulations using Kwant software can be done to confirm or infirm this hypothesis but most importantly, a critical discussion of simulation results must be done before going too fast into the conclusions. The simulation part can be found in Section 3.4.

3.1.2 Temperature-dependent transport and mobility extractions

The zero-magnetic field characteristic of the device regarding electronic transport can be seen in Fig. 3.6, depicting the conductance $G^B = 1/R^B$ vs. carrier density n at different temperatures in both Hall bar and constriction cases. The thermometer used to measure the temperature of the device had a calibration issue: the intermediate temperatures are adapted with approximate values.

In the Hall bar case, the charge neutrality point undergoes an unexplained shift toward the left from room temperature to $100K$ and stabilizes further towards lower temperatures. Moreover, the associated minimum of conductance is decreasing with the temperature decrease, suggesting a non-metallic behavior of carrier conduction at the charge neutrality point (like mentioned in Ref. [29]). When looking at higher carrier density, a wide linear dependence can be observed on the hole side at any temperature. There is only a tiny increase in the G^B_{HB} vs. n slope as the temperature decreases from 290 K, suggesting that electron-phonon scattering mechanism is not very effective and the global transport is weakly temperature dependent. The mobility μ of the carriers can be determined by the semi-classical Drude model in this linear regime:

$$\mu = \frac{1}{e}\left|\frac{dG}{dn}\right|.$$

For the lowest temperatures, the mobility computed within the linear part on the hole side is $\mu_p \approx 7000\ cm^2V^{-1}s^{-1}$. However, a very slight curvature of the traces can be observed at even higher carrier density, i.e. below $n \approx 1 \cdot 10^{12}\ cm^{-2}$: the Drude model is no longer valid and the evolution of G^B_{HB} becomes sublinear (see the black dashed lines in the Figure), which is appreciable since the transport

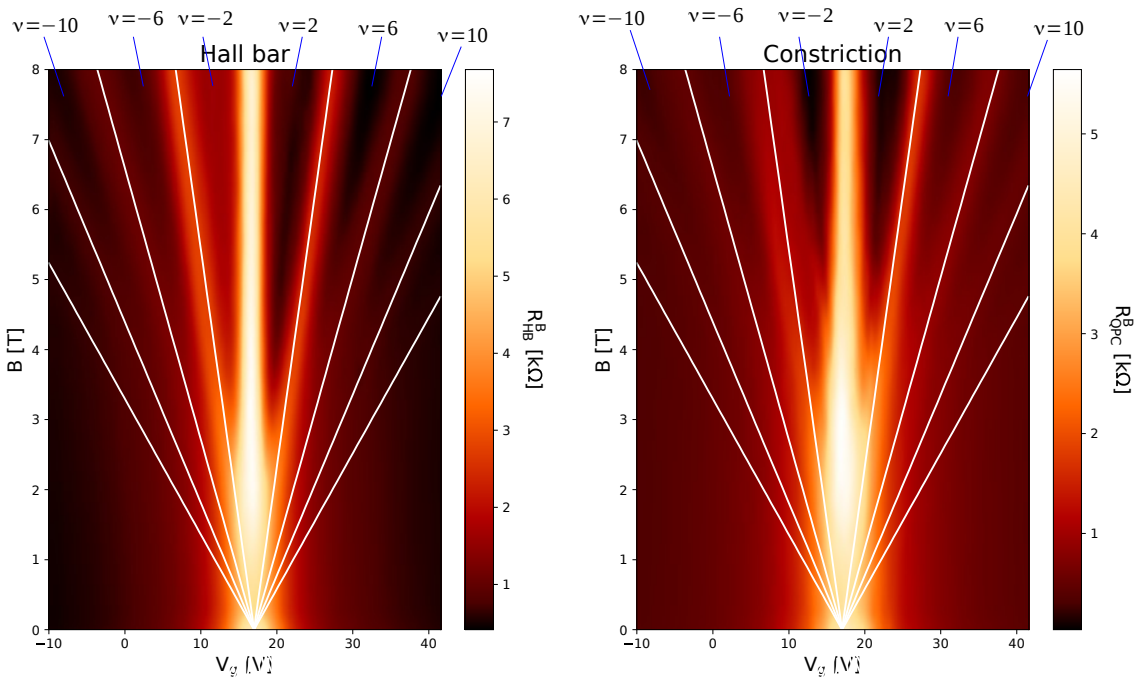

Fig. 3.4. Map of the longitudinal resistance R^B vs. (B, V_g) in the Hall bar as well as through the constriction at 2 K. The shape of a Landau fan is clearly visible in both cases. The white straight lines indicate the best fit to the loci of maxima in the resistance.

shifts from a less diffusive regime to a more ballistic one (without necessarily be fully ballistic). Indeed, ballistic transport is essential to facilitate the study of the constriction consequences in terms of average conductance evolution or size quantization observation [20]. However, this value of mobility is rather weak and results in a mean free path of the carriers l_e of $l_e = \frac{\hbar\mu_p}{e}\sqrt{\pi n_p} = 77.4\ nm$ at $n_p = 0.9 \cdot 10^{12}\ cm^{-2}$ which is found to be the limit between the linear part and the start of the slight curvature on the hole side. This l_e value does not exceed the relevant length of the device between the two probing contacts (contact 3 and 11). However, one needs to be careful and suggest that, since the measurement is of type 3-probe, the contact 3 resistance could contribute a lot to the reduction of the intrinsic conductance of the device and thus the associated slope in the linear regime. Hence, the mobility could be really higher than the one computed above. The contact resistance has not been measured, so an intrinsic mobility cannot be determined. This potential higher mobility would thus explain the observable onset of sublinearity at low carrier density in the conductance evolution found in Fig. 3.6 compared to lower values for which one would still only identify diffusive transport.

On the electron side, the evolution of G^B_{HB} vs. n becomes nonlinear at a lower carrier density than on the hole side. The different electron mobility values μ_n within the linear parts are more quickly varying with temperature than previously: it spans from $\mu_n(290K) \approx 5450\ cm^2V^{-1}s^{-1}$ to $\mu_n(2K) \approx 7350\ cm^2V^{-1}s^{-1} > \mu_p$. At 20 and 2 K, there are fluctuations with approximately regular spacing suggesting weak inelastic scattering events from electron-phonon and electron-electron interactions associated with mesoscopic transport. As a consequence, the fluctuations might result from

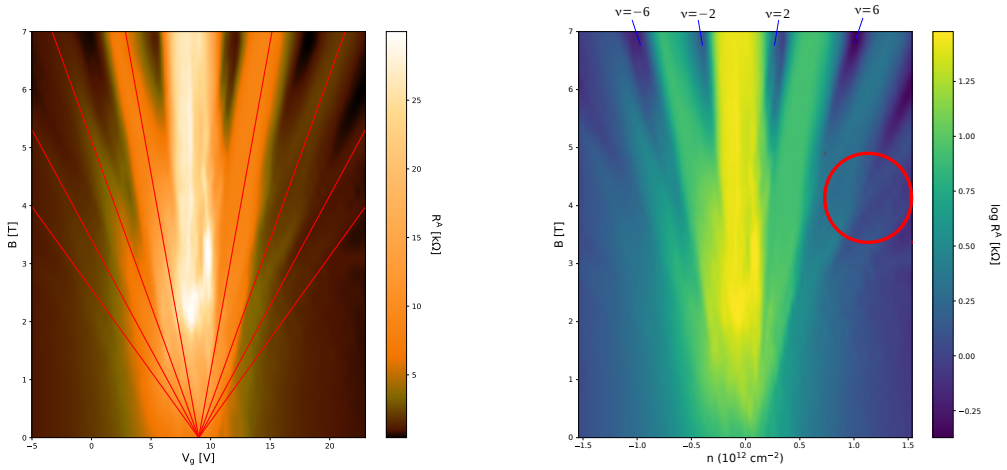

Fig. 3.5. (Left) Map of the absolute longitudinal resistance R^A vs. (B, V_g) at 2 K. The shape of a Landau fan is visible. The red straight lines indicate the best fit to the loci of maxima in the longitudinal resistance exhibiting observable Landau levels. (Right) Same map but with a logarithmic scale applied on R^A and using another colorbar in the B-n plane. The Landau levels are clearer than observed in the Landau map at the left.

transmitted discrete electronic modes from contact 3 where the polarized current is injected and where it is also used as a one of the voltage probes for the conductance G^B_{HB} determination. A much clearer amplitude of these fluctuations is observed for the lowest temperature, probably meaning enhanced quantum transport in the mesoscopic regime. The fluctuations of conductance can be better evidenced by subtracting the data by linear fits within a specific density ranges. This was done on the hole side and the resulting fluctuating conductance δG^B_{HB} can be found in Fig. 3.7 for different temperatures more accurately measured. One sees that despite the noisy data, more robust and pronounced fluctuations are observed as long as temperature decreases. These coherent fluctuations tend to appear starting from 9 K and stay robust as temperature goes down to 2 K. Indeed, within that range, the fluctuations seem to share common peaks and drops associated with a characteristic periodicity reminding the bare-eye evenly-spaced steps in left of Fig. 3.6. This demonstrates the genuine onset of mesoscopic transport at low temperatures along with associated conductance fluctuations whose periodicity according to the density axis may justify transmission modes from contact 3.

In the 500nm-wide constriction case of sample B , the global trends seem identical to the Hall bar case. At 2 K and 20 K, mesoscopic fluctuations are also visible but more pronounced, which may either be related to Universal Conductance Fluctuation effects (coherent interferences between electron semi-classical paths) surely enhanced around the constriction (due to resonances and quantum interferences of electrons back-scattered by impurities [13]), or to signatures of conductance quantization (this still has to be clarified). No mobility values should be extracted there since it does not represent an intrinsic property of the device: it is likely that the geometry of the constriction limits conducting electronic modes and may generate additional backscattering due to the edges [5], thus which does not represent the actual carrier mobility in the sample bulk. In addition, compared to the Hall bar case, the conductance values here are higher for any carrier density except maybe near the CNP. This can be counter-intuitive given the reduced average conductance predicted through a nanoconstriction but the conductance measurement is a 3-point one in the Hall bar case. Hence, the contact resistance through which the current enters into the graphene sheet contributes to the limitation of conductance, which can be sufficient to make a such observation.

On the other hand, Fig. A.2 shows the dependency on temperature of the zero-field conductance through the 340nm-wide constriction in sample A, with quite limited gate voltage range. The temperature values were taken on average due to the finite cooling rate of the VTI stage. Not much information can be extracted here. The minimum of conductance is still globally decreasing and the CNP also shifts as the temperature decreases but in the opposite direction than in sample A. Though, the shift associated to the lowest-T curve in purple is too important compared to the other curves. It is unambiguously explained by a new cool-down of the sample after its release from the cryogenic system which has been

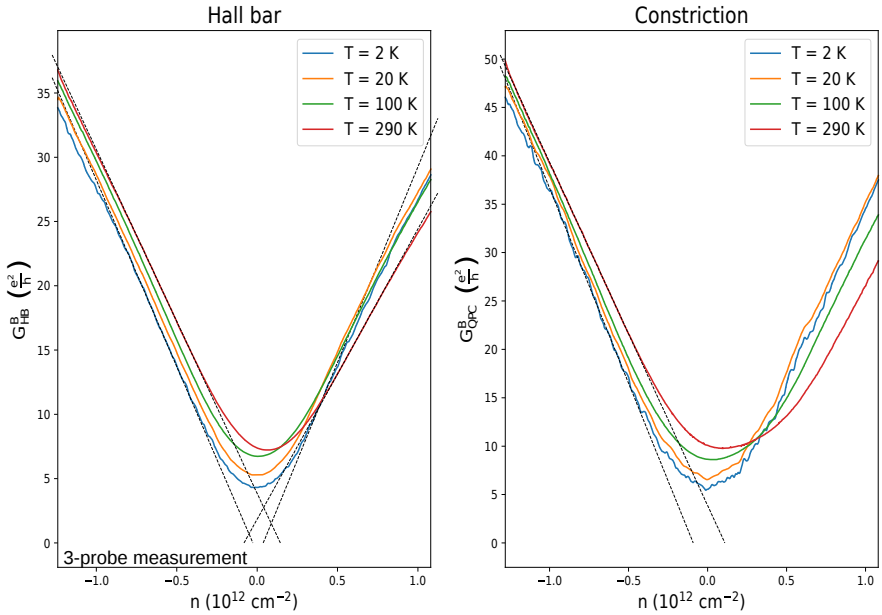

Fig. 3.6. Temperature-dependent zero-field conductance G^B vs. carrier density n in the Hall bar (3-probe measurement) and constriction cases. The thin black dashed lines are linear straight lines as a guide to the eye for observing eventual onset of sublinearity.

restarted to solve a temperature issue. Device was exposed to air for a couple of days (at least ten) before its insertion in the cryogenic system. With time, some species could get access to the edges and develop chemical modifications that would change the residual doping of graphene. The conductance measurement at 2 K was realized after that cool-down effect (also reported in Ref. [5]) unlike the previous ones. This additional doping translates the pronounced shift of the CNP at 9 V of the purple curve in Fig. A.2, a higher minimum of conductance than the measurement at 9 K and also a wider valley of conductance around the CNP. As for sample B, the temperature drop does not much affect the global conductance evolution suggesting that disorder giving rise to elastic scatterings instead of inelastic ones by electron-phonon (or electron-electron) interactions is dominant. Still, mesoscopic transport and quantum interferences are characterized by smooth fluctuations arising below 60 K from which on can deduce that the coherence length of the electronic waves becomes on the order of the characteristic length of the device (2 μm being the width of the Hall bar in Fig. 2.2). At 9 and 2 K, the quantum fluctuations due to mesoscopic transport are even more pronounced and they also very likely originate from resonances and coherent back-scattering of carriers around the constriction and also at the possibly rough constriction edges.

A higher range of gate voltages has been swept to make the conductance trace at 2 K. The extrapolation to even higher carrier densities can be seen in Fig. 3.8. The wide conductance valley in the vicinity of the CNP is well visible. The global evolution at the highest carrier densities clearly shows a more robust linear regime than in sample B within similar ranges, highly supported by the black dashed lines which are linear fits in good agreement with the evolution. Therefore, the absence of sublinear evolution which could have lead to $G \propto \sqrt{n}$ characteristic of a ballistic transport (since in intrinsic graphene, G linearly evolves with $k_F = \sqrt{\pi n}$) evidences a diffusive transport. Note that there is a more chaotic behaviour on the electron side with a weird saturation onset of G^A at $n = 1.0 \cdot 10^{12}$ cm^{-2} and then a sudden step of conductance. There are as well a lot of noisy oscillations. But the associated linear fit is still consistent since the evolution of G^A on this side would have been still well linear without this "saturation" issue. The more pronounced linear evolution suggests less appropriate transport characteristics to observe size quantization for instance since too many coherent scattering events brought by the diffusive transport around the constriction can well obscure the genuine conductance steps. Words about it will

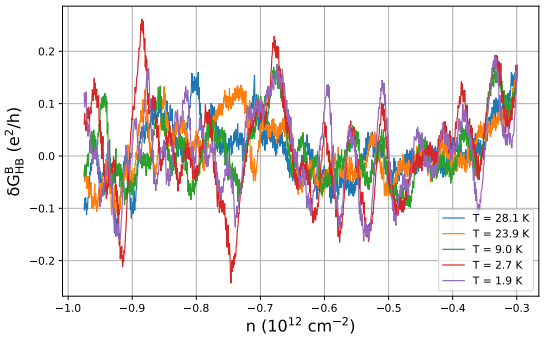

Fig. 3.7. Conductance fluctuations δG^B_{HB} obtained after subtracting the G^B_{HB} data by linear fits on the hole side at different temperatures.

be nonetheless given in the next section.

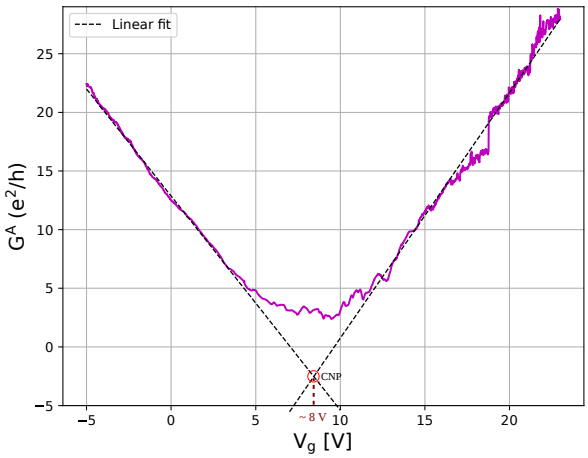

Fig. 3.8. 4-terminal conductance G^A vs. carrier density n at $T = 2\ K$. The two black dashed straight lines are linear fits to the conductance evolution on each type of doping (holes and electrons). The crossing between the fits give an idea of the corresponding CNP which is $V_{g0} \sim 8\ V$.

In consequence, it is thought that trying to observe and find quantized subbands from the quantum confinement in the nanoconstriction might be easier in sample B than in sample A, despite the usually much better devices that involve graphene encapsulated between hBN stacks than graphene directly on SiO_2 substrate.

3.1.3 Electronic signature within the quantum Hall regime

The Laudau fans previously described already show the development of the quantum Hall effect at large perpendicular magnetic fields. The evolution of quantized values of the Hall conductance G^B_{xy} regarding the Landau levels through the traces in longitudinal resistance is displayed in Fig. 3.9 at 8 T (round value since the field was slowly decreasing during the measurements) and as a function of carrier density n (up). The graph shows successions of quite well-defined peaks and drops in R^B_{HB} and R^B_{QPC} but lower amplitude of theses peaks are more observed on the hole side as well with it, a more pronounced differences between the Hall bar and constriction cases. G^B_{xy} is computed from the Hall resistance and the longitudinal resistance:

$$G^B_{xy} = \frac{R^B_{xy}}{R^{B^2}_{HB} + R^{B^2}_{xy}}. \tag{3.2}$$

The trend is such that the plateaus evolve according to half-integer values $-\frac{5}{2},-\frac{3}{2},...,\frac{5}{2}$. This is a clear signature of the typical half-integer quantum Hall effect in graphene. The quantized values in the Hall conductance in that case are

$$G_{xy}^{B} = g(N + 1/2)\frac{e^2}{h},$$

where $g = 4$ is the four-fold degeneracy in graphene (from spins and valleys) and N is the number of the Landau level mode which also includes the 0th mode [24].

The plateaus in G_{xy}^{B} are globally quite well aligned with the minima in the longitudinal resistances but small shifts between the middle of the plateaus and the corresponding minima can be identified. Anyway, these alignments indicate equilibrium at the edges without strong scattering through the bulk of the device, translating quantum Hall quantization. Another intriguing observation is that, contrary to theory, several values of R^B in Hall bar case do not reach zero or even close despite their location under a quantized plateau. These are especially evidenced on the hole side between the 0th and the 1st Landau level and also between the 1st and 2nd ones on the same side. It could be attributed to either the 3-probe measurement which adds an additional resistance probed by R_{HB}^{B} and whose contribution lowers as one goes further away from the CNP, or the passage of the edge channel(s) beneath the defective contact 10 between contacts 3 and 11 measuring this transport characteristic. In addition, the change of sign in G_{xy}^{B} coincides well with the highest peak in R^B for the constriction case but not in R^B for the Hall bar one. This comes from the centering of the density associated with the R_{QPC}^{B} trace according to Equation 3.1, which takes into account the gate voltage at the CNP. A slight difference ΔV_{g0} is observed between the R_{HB}^{B} ($V_{g0} = 17\ V$) and R_{QPC}^{B} ($V_{g0} = 17.5\ V$), explaining this relative shift. However, it is not significant and do not visually alter the true signature of the half-integer QHE. In addition, the plateaus are characterized by a significant finite width which translates the disordered structure in graphene on SiO_2 and the pinning of the Fermi energy preventing direct transitions from Landau level to Landau level. The finite width of the Landau level strips in Fig. 3.4 also tells about the disorder characteristic: indeed, bulk disorder is believed to be responsible of the broadening of the DOS associated with the Landau levels with a stronger effect if the bulk disorder is more important [17].

In Fig. 3.9 (down), the graph is similar except that the x-axis represents the filling factor $\nu = \frac{n}{n_L}$, which is the proportion of the total carrier density n (electrons or holes) in comparison to the carrier density in one single Landau level $n_L = \frac{eB}{h}$, taking into account the four-fold degeneracy in graphene. Yet, the 0th Landau level mode is an exception since both electrons and holes occupy the corresponding electronic state. The quantized values in the Hall conductance should correspond to $G_{xy}^{B} = \nu\frac{e^2}{h}$, where $\nu = 4(N + 1/2)$. This is clearly observable in the data since the succession of $\nu = -10, -6, -2, ..., 10$ all correspond to the same quantized value of $\frac{e^2}{h}$ in G_{xy}^{B}. Moreover, the set of ν values corresponds quite well (not perfect though) with the minima in the longitudinal resistance for both the Hall bar and constriction cases as depicted by the vertical black lines. The perfect alignment between the filling factors and the corresponding minima may be reached at even higher magnetic fields

According to the same justifications as done previously, the signature of the half-integer QHE is also demonstrated in sample A, looking at the two graphs in Fig. 3.10 at $B = 7\ T$ (round value). The Hall conductance G_{xy}^{A} here has not been computed according to Equation 3.2: it is rather equal to $1/R_{xy}^{A}$, evidenced by the divergence in the G_{xy}^{A} trace at $R_{xy}^{A} = 0$. The formal expression has not been employed here because of the shift between the sign change of R_{xy}^{A} and the maximum peak around $n = 0$ which would cause a falsified analysis. The same shift as discussed before is still present even in the quantum Hall regime. The way of computing G_{xy}^{A} here does not prevent the observation of the right localized Hall conductance plateaus according to the signature of the half-integer QHE. Typically, the term of the longitudinal resistance R_{xx} appearing in Equation 3.2 can be neglected in front of R_{xy} as it should correspond to a minimum when one lies on a plateau (interpreted via the dissipationless conducting edge channels leading to zero longitudinal resistance), amounting to the simple relation $G_{xy} = R_{xy}/R_{xy}^2 = 1/R_{xy}$ (so on the plateaus, it should be correct, but not at the transitions between plateaus).

In comparison to sample B, peaks in R^A are all much higher and some are much less narrower especially at the 0th mode of the Landau levels and on the electron side.

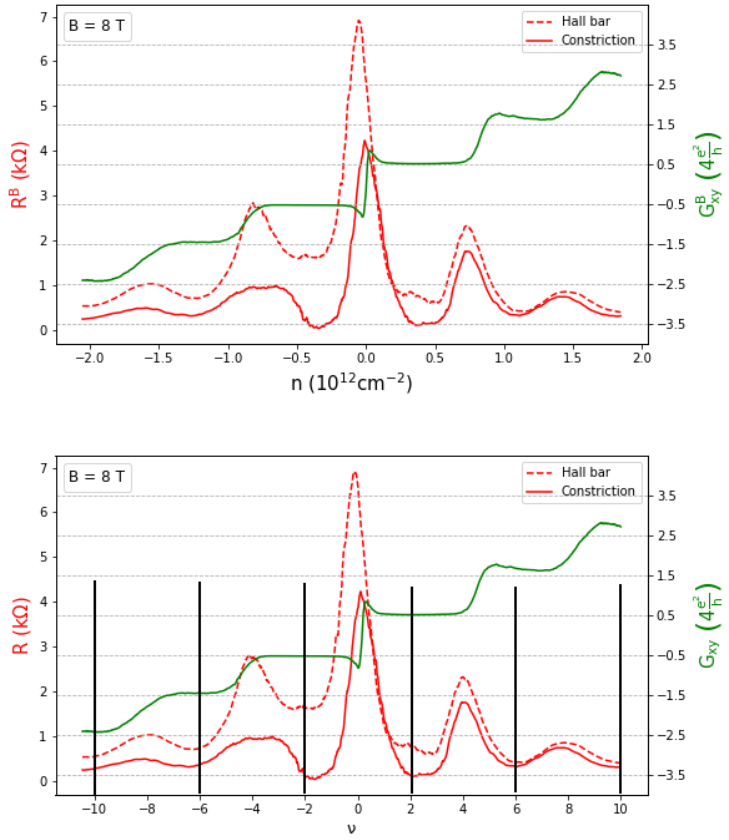

Fig. 3.9. Hall conductance G^B_{xy} and longitudinal resistance R^B vs. carrier density n (up) or filling factor ν (down) in the Hall bar and through the constriction at $B = 8\ T$ (round value) and $T \sim 3.5\ K$. The succession of plateaus in the Hall conductance demonstrates the signature of the half-integer quantum Hall effect in graphene. Vertical black lines originate from the filling factor values which show each the minima in longitudinal resistance, in agreement with the half-integer QHE.

3.2 Low B-field regime

3.2.1 Discussion about size quantization

As already discussed in Chapter 1, the current big challenge for observing conductance steps or kinks originating from size quantization in a lithographically-defined nanoconstriction is the quality of the device edges at the QPC boundaries. The edge roughness in such kind of devices is believed to be mainly the limiting aspect of electronic transport in the quasi-ballistic regime which is now easily accessible at low carrier density in graphene with the improvement of fabrication technology [5][20]. This is really important for hBN-graphene-hBN devices (as sample A) regarding the fabrication step involving the etching to give the constriction geometry and the associated edge roughness. In the case of graphene on SiO_2 (as sample B), the main challenge before considering the influence of the edges on transport is the transition from a diffusive regime to a quasi-ballistic one by significant reduction of disorder and enhancement of carrier mobility.

In this section, one focuses on the possibility of observing conductance steps possibly resulting from size quantization. The first convenient method that was exposed in Chapter 1 relies on the transition from the quantized subbands at zero magnetic field to the corresponding Landau levels at high fields. If the cyclotron radius l_c of one specific mode becomes smaller than the half constriction width $W/2$ at a critical field B_c, the position of the corresponding conductance plateau must be B-dependent with a smooth transition to a perfect linear evolution regarding the B-n plane (i.e. the Landau level development). As $B < B_c$, the plateau should be robust enough to be detected within similar carrier densities until the critical field is reached. The evolution of B_c can be seen in black dashed lines plotted on the Landau maps corresponding to the derivative of conductance through the constriction with respect to carrier

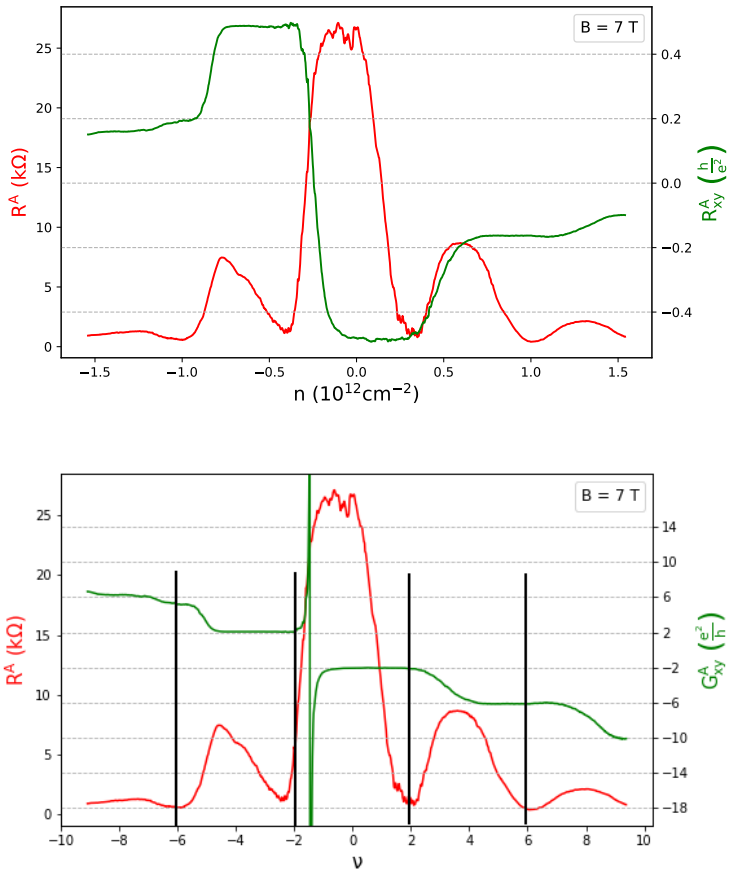

Fig. 3.10. Hall resistance R^A_{xy} vs. carrier density n (up) and Hall conductance G^A_{xy} vs. filling factor ν (down) through the constriction at $B = 7\ T$ (round value) and $T = 2\ K$. The succession of plateaus in the Hall conductance demonstrates the signature of the half-integer quantum Hall effect in graphene. Vertical black lines originate from the filling factor values which show each the minima in longitudinal resistance, in agreement with the half-integer QHE.

density $\partial G/\partial n$ for both samples (see Fig. 3.11). Applying the first derivative allows to probe eventual plateaus with a zero derivative. Using the partial derivative with respect to B is not convenient because of the quite high steps of field between successive measurements, thus no resolved information could have been obtained in this context. The critical field evolution was computed as $B_c = 2\hbar k_F/eW$ coming from the transition condition $2l_c = 2\hbar k_F/eB_c = W$ [22], which translates the square root evolution as can be seen on Fig. 3.11. In a reverse way, the evolution may also be used to find back the constriction width W by fitting the curves into the observed transitions according to the W value. However, this requires very clear data, which is not the case here. That is why the real geometrical widths associated to both samples ($W^A = 340\ nm$; $W^B = 500\ nm$) were already considered.

In case of sample A, the map clearly exhibits too much fluctuations at low fields and does not show any information about any possibel transition of quantized conductance from 1D subbands to Landau levels. The latter are still observable looking at the indicated filling factors ν but very wide white parts at Landau levels $N = 0, 1$ appear like corresponding plateaus in the real conductance G^A. This can also be observed in the longitudinal resistance trace shown in Fig. 3.10 which does not show narrow peaks but more highly broadened maxima for these levels.

In case of sample B, this appears more interesting since the results are much less "plagued" by fluctuations. In the Hall bar case, the data are smooth, indicating that the evolution of the conductance G^B_{HB} is less fluctuating than the constriction case where coherent transport is much more present due to the constriction itself. The fluctuations in the constriction case are much more resolved and indicate a cleaner sample than sample A in this context. However, it remains difficult to identify the genuine conductance steps or kinks looking at the transition. One can see narrow white strips on both electron

and hole sides emerging from the Landau levels and going down to smaller magnetic fields but they vanish before reaching possible plateau features at $B = 0\ T$. Therefore, the conductance steps or kinks cannot be likely identified as a result of size quantization. It seems that from 0 to 3 T, the coherent phenomena occurring in the constriction are too much dominant and obscure the signature of the presence of these conductance plateaus.

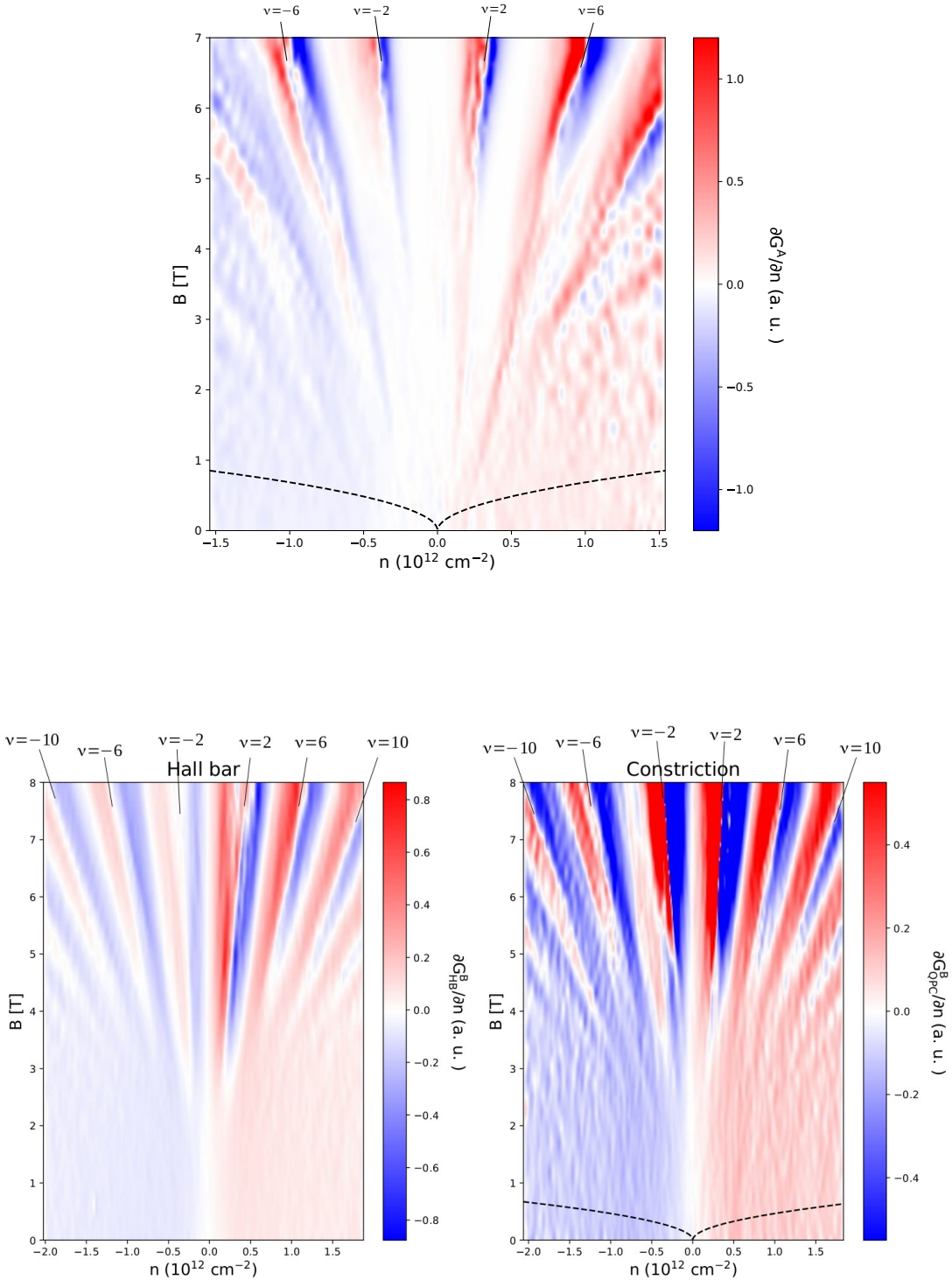

Fig. 3.11. Map of the derivative of conductance with respect to the carrier density $\partial G/\partial n$ in the B-n plane in sample A (up) and sample B (down) for Hall bar and constriction cases. The black dashed lines represent the critical field B_c at which the quantized subbands (at $B = 0\ T$) should theoretically transit to the Landau quantization regime (i.e. the establishment of edge channels) as long as $2\sqrt{2N}l_B$ becomes lower than the constriction width ($W^A = 340\ nm$; $W^B = 500\ nm$). *Inspired from Ref. [5].*

As shown before, the low temperatures are mostly responsible for the enhancement of resonances and coherent backscattering. If the measurements are taken at higher temperatures than 2 K, the associated phenomena would be reduced and true signature of size quantization can be possibly found. Indeed, Terrés and its team have plotted a temperature-dependent conductance evolution (see Fig. 4**c** in Ref. [5]) and they have observed signatures of specific conductance plateaus when temperature has exceeded $\sim 17-18$ K in their 230nm-wide constriction ballistic device. However, the initial kinks of the plateaus at the lowest temperatures have been transformed into smoother ones, probably due to the mitigation of mesoscopic effects limiting the Fabry-Pérot like oscillations responsible for the kink appearance [22]. The temperature dependence on the shape of the plateaus is thus significant but the quantized conductance is weakly temperature-dependent as long as the energy spacing between the subbands is wider than the thermal energy.

In sample A, the gate voltage ranges were too limited within the context of temperature-dependent transport to analyze the possible persistence of conductance plateaus in temperature. However, this is possible in sample B. In Fig. 3.12, two traces of the conductance through the corresponding 500nm-wide constriction at quite different temperatures are shown on the left (actually the same as in Fig. 3.6 except that the curve at 2 K does not come from the same measurement but it qualitatively shows similar features). The $20K$ curve is naturally smoother due to mitigated mesoscopic fluctuations. However, it shows quite some interesting discrete oscillations whose similarity is likely found in the $2K$ trace. This is emphasized inside the blue box and the corresponding zoom on the right. Indeed, the colored horizontal lines show positions of plateaus which are clear in the $2K$ curve but very smooth in the other one although they can be still observable. The different colors indicate the similarity between the plateaus on both curves and they appear roughly at the same carrier density level at both temperatures. In addition, the spacing between corresponding features in both traces is quite even and amounts to approximately $\Delta G^B_{QPC} \simeq 3e^2/h$. In lithographically-patterned nanoconstriction devices, the conductance steps from size quantization are not necessary the classical quantum of conductance in graphene (i.e. $4e^2/h$) but can be smaller. This aspect is believed to originate from strong scattering at the rough edges in the constriction at low temperatures with a reduced average transmission of modes [20]. More will be explained into the next discussion, mainly about sample B, for which the best data were measured. For now, one can assume that the plateaus shown in right of Fig. 3.12 are indeed associated with 1D quantized subbands since the corresponding steps in the $20K$ trace can be still attributed to size quantization in agreement with the results and discussion from Terrés' work. The shape is reminiscent of kinks with periodic modulations occurring in non-ideal constrictions.

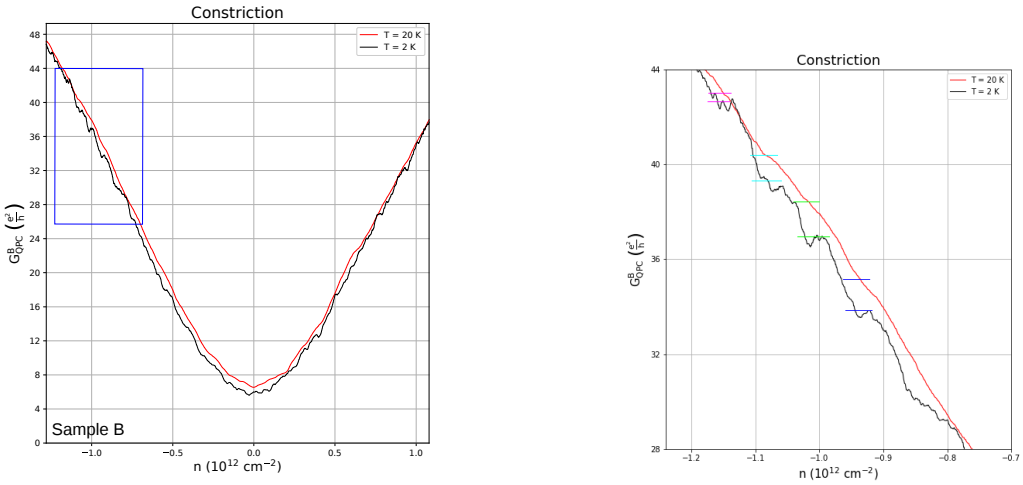

Fig. 3.12. (Left) Zero-field conductance G^B_{QPC} in function of carrier density n at ~ 20 and 2 K. (Right) Zoom from the graph corresponding to the part encompassed by the blue box seen on the full plot at the left. Some significant conductance plateaus at both temperatures with quite even spacing are evidenced by colored horizontal lines.

Another data treatment was realized to evidence the signature of size quantization found in conductance steps and is represented in Fig. 3.13. The x-axis represents the dimensionless quantity whose one unit increment should increase the conductance by one additional quantum of conductance $4e^2/h$ (i.e. the transmission of one new mode) in an ideal (non-disordered) constriction and depends on the width of the latter. For $W^B = 500\ nm$ in sample B, one sees that each successive plateau on the hole side and shown with black arrows (actually, those which were found previously) crosses successive integer values, in good agreement with the model of parabolic or square confinement potential (stating that one additional mode is transmitted when $k_F W$ reaches a multiple of π [13]). On the electron side, other four successive plateaus are emphasized and the same reasoning also applies. However, they were not identified using Fig. 3.12 because of less accuracy of the conductance trace at 20 K. They can be found around carrier densities a little bit greater than $n = 0.5 \cdot 10^{12}\ cm^{-2}$ in the same figure. The spacing between them is actually less than on the hole side and is roughly $\Delta G^B_{QPC} \simeq 2e^2/h$. This difference between both sides will be explained below using the model of quantum ballistic transport within the Landauer theory. Finally, from these aspects, one can state that these plateaus might result from size quantization as well.

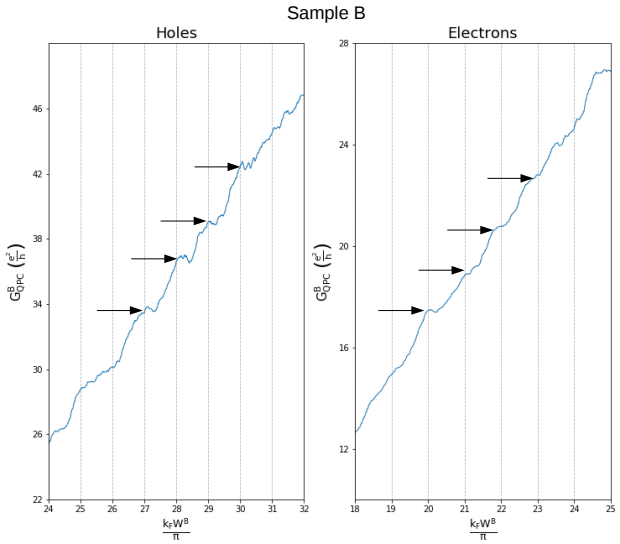

Fig. 3.13. Zoomed parts of the zero-field conductance evolution G^B_{QPC} at 2 K in function of the dimensionless quantity $k_F W^B/\pi$, with $W^B = 500\ nm$. The arrows indicate plateaus which could be consistent with the manifestation of size quantization in sample B.

A possible new method which can be employed is to more precisely analyze the weak magnetic field-dependent conductance traces as a function of carrier density and identify the conductance steps which must be theoretically robust as long as the field increases in the weakest ranges, while non-including the transition from the quantized subbands to the Landau levels. However, this was found to be too hazardous since nothing really concrete has been observed. The Landau maps in Fig. 3.11 well proves the difficulty of this procedure. The traces were too fluctuating without saving specific conductance steps like if they were blurred by mesoscopic interactions, even for the observed plateaus in sample B at zero field. In addition, it must be reminded that the magnetic field was not fixed but has slowly decreased during each gate voltage sweep. This can result in universal conductance fluctuations at low temperature, possibly hiding the genuine steps from size quantization.

3.2.2 Effects from size and edge roughness on the average (ballistic) conductance evolution

Now, the analysis will mainly focus on the conductance evolution with respect to the Fermi wavenumber $k_F = \sqrt{\pi n}$ both on hole and electron sides (without magnetic field). Based on this, the main objective will be to discuss about the impact of the constriction width and the edge roughness on transport through the constriction channel in the samples. As mentioned in Chapter 1, the average conductance $G^{(0)}$ expressed in Equation 1.11 does not account for the periodic modulations and only accounts for the linear behaviour with a characteristic slope depending on the constriction width W and the limiting coefficient transmission c_0 (considered as energy- or mode-independent for simplicity). A linear evolution in function of k_F requires that transport must be ballistic, in accordance with the Landauer theory. Determining c_0 in the ballistic regime can give some information on the edge quality and their effective low or strong scattering power which limits the average transmission of the modes.

In sample A, the conductance traces in function of k_F can be seen in Fig. A.3 and they do not show a clear and robust linear evolution even for the highest k_F values, which is associated with a diffusive regime as seen previously in Fig. 3.8 for the accessible carrier density ranges. Hence, a reliable determination of the "effective width" $c_0 W^A$ via the slope is not possible. To go further, a comparison of the conductance curves with respect to carrier density n has been done between sample A and the encapsulated graphene device with a 230nm-wide constriction data from the Stampfer's team. This is represented in Fig. 3.14. Compared to Terrés *et al.*'s sample (curves in black and also in green obtained after a cool-down process), one notices that the conductance associated with sample A (G^A in blue) evolves slower than the conductance of the 230 nm-wide constriction at low carrier density $|n| < 1 \cdot 10^{12}\ cm^{-2}$, without taking into account the flat part of the green curve. Then at higher carrier density, due to the $\sqrt{n}$-dependence seen in Terrés' sample, characteristic of ballistic transport (the solid red curves denote the ballistic evolution that is experimentally reached outside the shaded regions), G^A starts to evolve faster since the long-range scattering mechanism is still dominant before reaching the ballistic regime at higher carrier densities. The constriction width of sample A, i.e. $W^A = 340\ nm$, is ~ 48 % larger than the 230nm-wide constriction belonging to the Stampfer's team. Therefore, G^A should evolve much faster and consequently be higher according to the Landauer formalism and to the expression of the average ballistic conductance $G^{(0)}$ including the width itself, which still confirms the diffusive regime in the present case. If the ballistic regime could have been reached for sample A, one could have determined the slope of the linear evolution with respect to k_F and precisely c_0^A. Looking at Fig. A.3, one can still evaluate the local slope at the very end of the curves: it should constitute a lower bound of c_0^A since the extrapolation towards higher density should exhibit the linear evolution associated with at least a higher slope than the local computed slope. The lower bound is determined by a linear fit to the end of the curves (not shown in the current figure) and amounts to roughly $[c_0^A W^A]_l \simeq 200\ nm$ for both sides actually. This gives a lower bound of the average coefficient transmission $[c_0^A]_l = 0.59$. In comparison, using Fig. 1.17 for other devices from Stampfer's team, their closest device in terms of constriction width is the 310nm-wide one which is characterized by $c_0 \simeq 0.9$ [5]. This is much higher than the lower bound for sample A although the width of the latter is roughly 10 % wider, which could suggest a lower quality of the constriction edge roughness defined by reactive ion etching in sample A. However, the genuine c_0^A value could be higher and possibly bias this value.

Finally, the lack of ballistic transport observed in sample A can be explained by favouring one among two main hypotheses. Either the transport is limited by the bad quality of the transfer of hBN onto graphene which has generated an important amount of impurity charges at the interface or it is limited by the stronger scattering events occurring at highly rough and dirty edges around the constriction brought by the etching process. The first hypothesis is favoured. Indeed, the lower bound value of c_0^A (0.59) is still

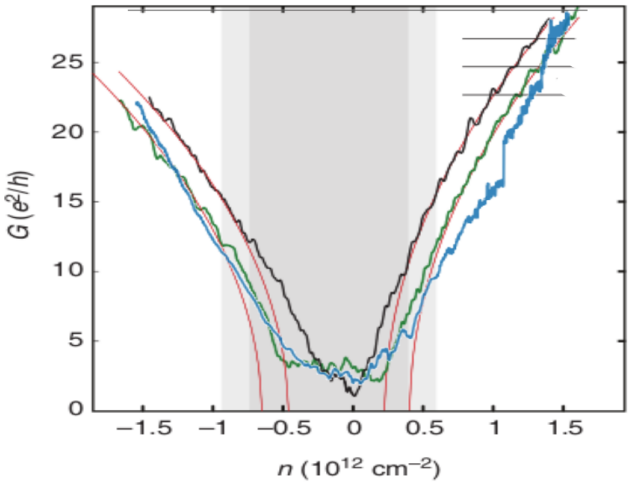

Fig. 3.14. Comparison of conductance traces G vs. carrier density n from sample A (blue) and the 230nm-wide constriction encapsulated graphene device from Stampfer's team (black and green) [5].

higher than values found in the devices from Stampfer's team featuring the narrowest constriction widths, i.e. around $c_0 = 0.5$. These were still featuring ballistic transport at low carrier densities (as noticed in Fig. 3.14 for $W = 230\ nm$) even if the edge disorder is noticeably more responsible of reduced average conductance $G^{(0)}$. The coexistence between rough edges considerably affecting electronic transport with backscattering[3] and a nonetheless ballistic conduction is explained by the constriction centre free of defects while disorder is dominating near the edges (as previously discussed via Fig. 1.17). Hence, partial transmissions of modes ($c_0 < 1$) through the constriction remains possible within the quantum ballistic regime of transport with inner electronic paths which are not scattered along the constriction [22]. This could also happen in sample A but its diffusive characteristic cannot be thus explained by this second hypothesis, favouring the first one, even though one cannot fully neglect the contribution from the edges.

Switching to sample B the conductance evolution G^B as a function of k_F can be seen in Fig. 3.15 in the Hall bar and constriction cases. One can see that the onset of linear evolution seems to happen at lower density in the constriction case than in the other one as well as in sample A. The linearization of G^B_{QPC} fortunately allows to apply the Landauer formalism to compute the "effective width" $c_0^{B^{(h,e)}} W^B$ from the average conductance $G^{B^{(0)}}_{QPC}$, where h, e denotes electrons and holes respectively and $W^B = 500\ nm$. The green curves are the linear fits to the linear evolution and give $c_0^{B^h} W^B \sim 340\ nm$ and $c_0^{B^e} W^B \sim 280\ nm$. These give $c_0^{B^h} = 0.68$ and $c_0^{B^e} = 0.56$. The discrepancy between the electron and hole sides can be explained by a non-uniform distribution of charge impurities at the edges defining the constriction geometry. The closest device in terms of constriction width from the Stampfer's team is the 440nm-wide one. As seen in Fig. 1.17, the corresponding average transmission coefficient is roughly $c_0 \simeq 0.9$. In this case, sample B features lower values and thus undergoes much less probable transmitted modes. As discussed in Terrés' work, the transmission coefficient is likely to decrease as the width decreases because of more probable reflections at the edges. Though, the 500nm-wide constriction in sample B has similar c_0 values as the 230 and 280nm-wide devices from Stampfer's team. This means that its edges are much rougher and strongly limit transmission compared to its constriction width with the other. The geometry of the constriction can also explain these rather small c_0^B values: comparing left of Fig. 2.1 and Fig. 2.2, sample B features a smoother modulation of constriction width than sample A featuring a sharper modulation, similar to Stampfer's team devices. Hence, the edge roughness which can affect transport is extended on a more larger distance than in the other devices and reflection events are more numerous, which heavily limits the transmission probability of modes.

To further support the genuine aspect of the conductance plateaus found in sample B looking at Figs. 3.12 and 3.13, one can refer to the average spacing between the steps and linking it to the computed transmission coefficient. In an ideal constriction, each successive step of conductance adds an additional

[3]Typically intervalley backscattering in graphene which allows to probe disorder on very short length scales, due to the high momenta at the **K** points and therefore, to typical low Fermi wavelengths. This gives rise to more fluctuations than in III-V heterostructures for which the Fermi wavelengths are not small enough to probe disorder at such length scales (explaining the easier observations of quantized conductance for such heterostructures) [22].

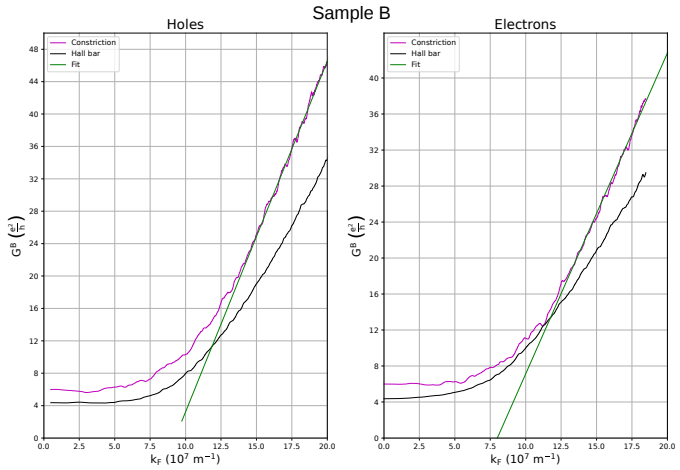

Fig. 3.15. Evolution of the zero-field conductance G^B on the hole and electron side as a function of the Fermi wavenumber k_F (computed as $\sqrt{\pi n}$) in sample B for the Hall bar (3-probe measurement) and constriction cases at 2 K. The fits approximate the average conductance $G^{B(0)}_{QPC}$ linearly evolving at high carrier densities. The product $c_0 W^B$ can be thus extracted from the fits on the hole and electron side.

quantum of conductance $4e^2/h$ in graphene (with spin and valley degeneracy). If limited transmission is taken into account by edge disorder, then the spacing $\Delta G \simeq c_0 \dfrac{4e^2}{h}$. On the hole side in sample B, the spacing was said to be roughly $3e^2/h$ (with some variations) and the computed spacing is $\Delta G^B_{QPC} = 0.68 \cdot \dfrac{4e^2}{h} = 2.72 \cdot \dfrac{e^2}{h} \simeq \dfrac{3e^2}{h}$. On the electron side, the spacing was roughly $2e^2/h$. The computed spacing is $\Delta G^B_{QPC} = 0.56 \cdot \dfrac{4e^2}{h} = 2.24 \cdot \dfrac{e^2}{h} \simeq \dfrac{2e^2}{h}$. The spacing relative to each side is thus in quite good agreement with the computed limited transmissions and demonstrates the genuine 1D quantized subbands provided by these steps. In addition, the deviation of the product $c_0 W$ from the geometrical width proper to each sample using the quantum ballistic model allows to reliably get back to the real width and make a good correspondence between experiment and theory.

3.3 High B-field regime: peculiar features within the quantum Hall regime

In the high field regime, new features beyond the half-integer quantum Hall effect in graphene may appear. In this section, some unconventional observations found in the measured samples will be described.

First, one thing to notice is the peculiar feature in the Landau fan in Fig. 3.5 encompassed in red circle. It seems that a Landau level emerges from beneath the 2nd one on the electron side. This could be attributed to degeneracy lifting but it is not the case. This Landau level is already known from the left graph and was subjected to the fitting lines to extract the experimental gate lever-arm α^A_{exp2}. More over, a graph of the Hall conductance steps is shown in Fig. A.4 for magnetic fields at the same order than their corresponding values in the red circle of the Landau fan. Clearly, the steps down to $-14e^2/h$ follows the half-integer QHE sequence typical in graphene. No other observed plateau should thus suggest a degeneracy lifting.

In Fig. 3.10, there is also a suspicious region that can be observed for sample A. Indeed, It is located on the maximum trace of R^A corresponding to the first peak to the left, above $\nu = -4$. The trace tends to draw a discreet local drop which is reminiscent of degeneracy lifting by Landau level splitting. The good alignment with $\nu = -4$ enhance the legitimacy to mention this peculiar feature. One efficient way to evidence a potential degeneracy lifting is to plot a Landau map of the partial derivative of the longitudinal resistance and to check whether a consistent data appears at the searched location. Left of Fig. 3.16

illustrates such kind of map. One sees that despite the clear identification of the expected filling factors in graphene, there is a strip lighter than the surroundings which seems to follow a consistent path to the Landau level developments. To go deeper, the same Landau fan can be done again but with replacing the x-axis by the filling factor which in addition, is dependent on the y-axis, i.e. magnetic field. Such kind of map has a particular shape at the low field regime because the filling factor is not well defined out of the quantum Hall regime. However, focusing at higher fields makes the filling factor relevant and the information on the map will be more straight, since the gaps between the Landau levels must stay aligned with ν. Right of Fig. 3.16 shows the same quantity but as a function of filling factor and magnetic field. One sees that the vertical purple line is aligned with $\nu = -4$ and quite well corresponds to the lighter strip previously observed. Hence this must be more than likely a signature of degeneracy lifting.

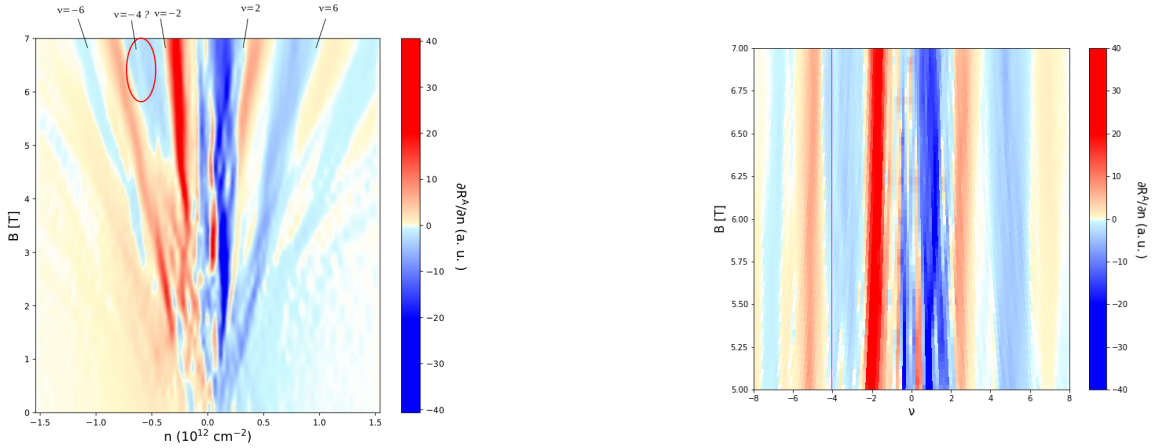

Fig. 3.16. (Left) Landau map (B-n plane) of the derivative of the longitudinal resistance with respect to carrier density $\partial R^A/\partial n$. A zone encompassed in red shows an additional local drop of resistance which starts at $\sim 6\ T$ and seems to follow a certain consistent path maybe associated with the filling factor $\nu = 4$. (Right) Same map with a zoom except that the carrier density n was replaced by the filling factor ν. A magenta line associated with $\nu = -4$ crosses and is well aligned with the lighter strip corresponding to the peculiar drop of resistance.

The same process has been applied for sample B for which it is also expected that a degeneracy lift occurs. Here directly is shown the Landau maps in both Hall bar and constriction cases as a function of ν and B. In the Hall bar, nothing striking has been observed but in the constriction itself, another vertical strip identified by the red oval is appearing also well aligned with $\nu = -4$, using the vertical black line as a guide. So this surprising feature proves signature of degeneracy lifting, exactly as in sample A.

There is probably something to learn about these local drops of longitudinal resistance that are found exactly at the same filling factor for both samples. In addition, it was only found in the constriction case instead of the Hall bar case in sample B. Hence the origin of this common degeneracy lifting could be explained by the presence of the nanoconstrictions. However, no current explanation about it is provided as well as there is no idea whether these Landau splittings are relative to spin or to valley degeneracy. A lot of experiments involved for instance tilting magnetic fields for which the possible lifting relative to spin does not depend on the perpendicular component of the field but on the total field [30]. So other experiments than measurements with perpendicular magnetic fields would be suitable to get more information on this.

3.4 Numerical simulations in Kwant

As mentioned in this chapter, a pronounced shift between the Hall resistance transition and the corresponding maximum longitudinal resistance within the 0th Landau level in sample A has been observed (seen in Fig. 3.10). The stated hypothesis based on this observation is charge inhomogeneities in the device at different locations for which transport is not affected the same way. A simple means to investigate such case is to make numerical simulations. The software which is used for the calculations is *Kwant*, a python package for computing quantum transport based on a tight-binding model. For understanding the presented case below, lots of needed information can be read in Appendix C (it is better to read it before going into this section) and the official paper is also available to know all details [31]. Notably,

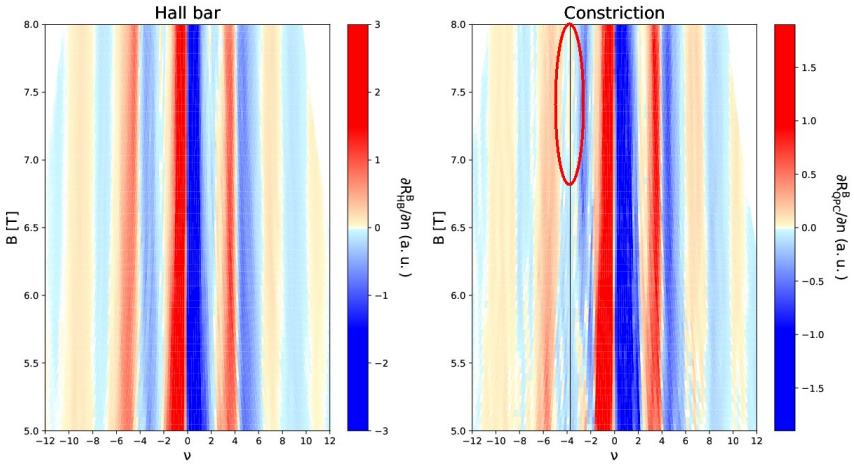

Fig. 3.17. Landau map of a zoom on the derivative of the longitudinal resistance with respect to carrier density $\partial R^A/\partial n$ in a B-ν plane. A black vertical line crosses a local development of a new Landau level suggested by the vertical warm strip encompassed in red and quie well aligned with $\nu = -4$.

Appendix C explains: Kwant in general; a brief description of how the problem is put up within the tight-binding model and the conditions for feasible simulations; the main parameters of the studied system in graphene; a description about a scalable tight-binding model for saving computation time while keeping the properties from a real graphene system [32]; the way of how the transmission/conductance is computed is based on the scattering matrix.

3.4.1 Physical conception of the problem

Before landing onto the simulations themselves, one has to think about the concept to address the issue, i.e. to think about a physical situation linked to the starting hypothesis. One needs to simultaneously evaluate the longitudinal resistance R_{xx} and the Hall resistance R_{xy} (or conductance G_{xy}) in a four-probe measurement like in the experimental case. In addition, one should imagine inhomogeneities in the potential landscape plus potential disorder in order to observe wide enough Hall plateaus. Both contacts probing the longitudinal resistance can for example feel a different potential magnitude than the ones probing the Hall resistance to make inhomegeneities appearing in the results. However, this deviates from the explanation of the hypothesis of strong charge impurities especially located at the constriction edges in sample A, but this is really a simple model which actually neglects disorder on edges. However, it would be nonetheless interesting to know which results it gives. In sample A, one common contact was used to measure both transport characteristics. In the physical concept, one could also consider a common contact while setting a different potential landscape close to the other contacts. To do so, a model based on a global spatial potential step ΔV can be considered. The step is continuously established along the device and creates a pn junction at the centre, in the constriction with a sufficiently small junction width in order to homogenize the potential across each contact (being far from the constriction itself). For example, at the very left of the device, a negative potential "-pot" can be defined while a positive one "+pot" (symmetrical and such that 2*pot = ΔV) is defined at the very right. To make a rigorous investigation, different values of ΔV should be considered. One could also compare the results at different magnetic fields while conserving the potential step or at different disorder potentials.

3.4.2 Tight-binding system in Kwant and parameters

Now that the concept is finished, one can think about the implementation of the model using Kwant. Note that the results will be interpreted in a qualitative manner rather than quantitative. The geometry and dimensions of the scattering region will always be the same during all simulations as well as the scaling factor s_f within the scaled tight-binding model. The system is represented in left of Fig. 3.18. The largest width is 1 μm while the length is 1.5 μm. The width of the constriction is identical to sample A, i.e. 340 μm. Six different leads are attached to the region and are labelled according to their order

of definition in the codes. Their width is similar to the constriction width. The first two leads act as current source and drain and the transmitted current will flow from the first one the the second one. Their direction is conform to the triangular Bravais lattice which is generated by a linear combination of the basis vectors of graphene with integer coefficients [28]. The 3rd, 5th and 6th leads are used as voltage probes, with the 6th one being common for computing the desired transport characteristics R_{xx} and R_{yx}. Given the configuration represented with the direction of arrows, the 6th lead will set the reference potential to $V_6 = 0$ for a reason explained below. In addition, the system is scaled with a constant scaling factor $s_f = 15$. The lattice constant is thus $a = 15a_0$ with $a_0 = 0.142\ nm$ the carbon-carbon distance in real graphene and $t = t_0/15$ with $t_0 = 2.8\ eV$ the nearest neighbour hopping energy in real graphene [32]. Hence, the graphene band structure is conserved and the Fermi energy of the scaled system can be considered as the one characterizing the real system (i.e. it can be expressed in eV). The main limitation on the usable energy ranges is the condition of the tight-binding model validity which is more restrictive as long as s_f increases[4].

The onsite potential associated to each site, i.e. the potential landscape, can be seen in right of Fig. 3.18 in agreement with the imagined physical concept. It comes from two added contributions:

1. The global potential step ΔV showing the different shades along the device. It will vary during the simulations to compare the results. The negative part will always lie on the left side and the positive part on the right side. The potential step evolves continuously according to a hyperbolic tangent function: to be precise, the corresponding onsite for each site is pot$*tanh(x/W_{pn})$ with x the position of one site along the device and $W_{pn} = 100\ nm$ the fixed pn junction width. Comparing the labelled leads on the left and the potential step on the right in the current Figure, inhomogeneities are effectively created with the 6th and 5th leads measuring R_{yx} and not feeling the potential step, and with the 6th and 3th leads measuring R_{xx} and feeling the full potential step;

2. Potential fluctuations associated with Anderson disorder. It is easily implemented and generate uncorrelated disorder with a random gaussian distribution of potential specific of each site. In the case of graphene, it does not consist of a realistic model of disorder since the latter is not correlated unlike the electron-hole puddles which are typically observed in experiment (like seen in Fig. 1.11). This could have been an improvement on the simulation part compared to uncorrelated disorder but charge puddles were not included. Be that as it may, the configuration of disorder globally remains identical for all simulations except once for comparison and is observable under the shape of the blurred surface in right of Fig. 3.18.

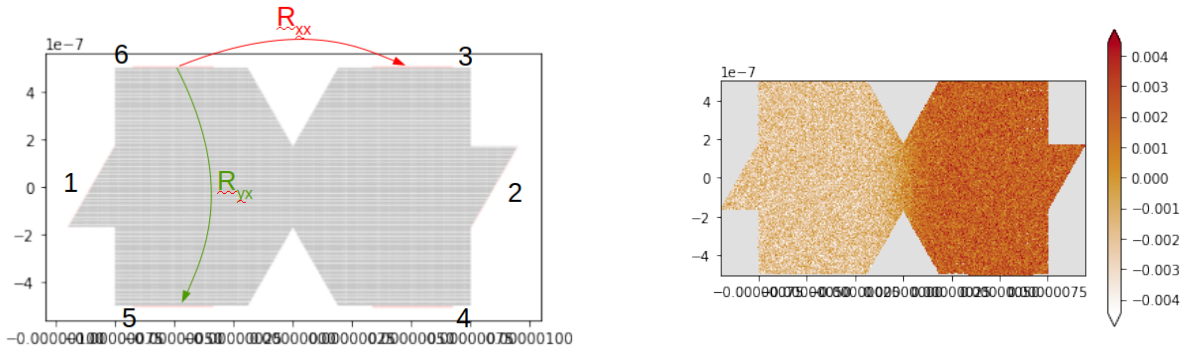

Fig. 3.18. (Left) Geometry of the studied graphene system with a 340nm-wide abrupt constriction. Six labelled semi-infinite leads are attached to it. The simulations compute the four-probe longitudinal resistance R_{xx} and the Hall resistance R_{yx} with the 6th lead for which the reference potential is set to $V_6 = 0$. (Right) Same geometry but with a chosen potential landscape defined by Anderson disorder and by a potential step resulting in simple inhomogeneities over both sides of the constriction.

The computations also require the adding of a perpendicular magnetic field. To describe the effect of the magnetic field, a so-called Peierls substitution is employed in the "tight-binding" model (learnt in

[4]Because the condition states that $E < t = t_0/s_f$.

Kwant courses). The magnetic field induces Lorentz forces and an associated phase shift proportional to the vector potential $\boldsymbol{A}$ during hopping t_{ij} between sites i and j:[5]

$$t_{ij} \rightarrow t_{ij} \times \exp\left(i\frac{e}{\hbar}\int_{\mathbf{x}_j}^{\mathbf{x}_i}\mathbf{A}(\mathbf{x})d\mathbf{s}\right).$$

For a field along the z-axis in the two-dimensional model, the integral becomes:

$$\exp\left(i\,\frac{e}{\hbar}B\frac{(y_i+y_j)}{2}(x_i-x_j)\right)$$

$$\exp\left(i\,2\pi\frac{\phi}{\phi_0}\frac{(y_i+y_j)(x_i-x_j)}{A}\right)$$

with $\phi = BA$ the magnetic flux through a unit cell of graphene ($A = 3\sqrt{3}a^2/2$ with a the carbon-carbon distance) and $\phi_0 = h/e$ the quantum flux.

3.4.3 Computation of the transport characteristics

The most simple way to determine the resistance or conductance in Kwant is the determination of the electronic transmission based on two single leads connected via the scattering region, which consists of a 2-terminal computation (more details are explained at the end of Appendix C). If 4-terminal resistance/-conductance (or nonlocal resistance/conductance) is desired, a different implementation in the code is necessary (instructions inspired from a discussion found in a forum about Kwant):

1. Usually, as for a two-terminal computation, calculate the scattering/S-matrix of the system with the six leads + the scattering region according to the defined parameters (E_F, B, onsite potential etc.);

2. From the S-matrix, create the conductance matrix G_{ij} by computing each transmission from lead i to lead j (then if 6 leads, the matrix will contain $6^2 = 36$ elements thus including the reflection parts for $i = j$);

3. The conductance matrix must be then corrected from subtracting all its elements by the sum of the diagonal ones because transmission returned by Kwant is the norm of the corresponding block of the scattering matrix, including the reflection blocks. Indeed, all rows and columns must sum to zero;

4. In order to determine nonlocal resistance/conductance with a unique solution, one needs to eliminate one row and one column from the conductance matrix associated to the lead for which the corresponding voltage is set to zero. It is the reason why the 6th lead in the Kwant system in Fig. 3.18 is the last one and common for both transport characteristics with $V_6 = 0$; because it was easier in the code to remove only the last row and column of the conductance matrix corresponding to this lead. Also, by current conservation, the current I through the drain terminal (2th lead here) can be calculated;

5. Finally, on imposes current to be "1" in the 1st lead (source), "-1" in the 2th lead (drain) and, on one hand calculate the voltage in the 3rd lead (directly $V_3 - V_6$ since $V_6 = 0$) for probing $R_{xx} = V_3/I$, on the other hand calculate the voltage in the 5th lead (directly $V_5 - V_6$ since $V_6 = 0$) for probing $R_{yx} = V_5/I$. This is done using a solver regarding linear algebra.

The corresponding Hall conductance G_{yx} is still computed according to Equation 3.2. In the results, G_{xy} is displayed whereas it is actually the real $G_{yx} = -G_{xy}$ but it just corresponds to the opposite sign similarly to the experimental results in sample A.

[5] $\boldsymbol{B} = \nabla \times \boldsymbol{A}$ with $\boldsymbol{A} = (-By,0,0)$ in order to conserve translational symmetry along the axis of transport (i.e. x-axis here).

3.4.4 Simulation results and discussion

Different results from the simulations are displayed for several different parameters. Given $t = t_0/sf = 0.187\ eV$, the investigated energy ranges is $E = [-t/2, -0.002]\ eV$ on the hole side and $E = [0.002, t/2]\ eV$ on the electron side with $N = 140$ computed points for each. The unexplored gap between -0.002 and 0.002 eV is to avoid the singular matrix issue for energy close to 0 eV.

The first parameter to play with and which is the key for determining the plausibility of the starting hypothesis potentially explaining the peculiar shift in sample A is the potential step ΔV. Plots of R_{xx} and G_{xy} according to the configuration in left of Fig. 3.18 at $B = 7\ T$ and different potential steps including the absence of step are displayed in Figs. 3.19 and 3.20. The given Anderson disorder potential with the gaussian distribution is $0.05/s_f = 0.003\ eV$. A straightforward observation is that the transition between plateaus in G_{xy} at the sign change level (i.e. at the 0th Landau level) is visible everywhere while R_{xx} of the corresponding Landau level is non-zero over the same transition width. This observation allows to confirm that the hypothesis of such kind of implemented inhomogeneities is not valid for explaining the relative shift seen in sample A, even the explanation of this shift gave previously still holds. Nonetheless, the qualitative interpretation of the results is still interesting because it is actually consistent with theory in terms of transport within the quantum Hall regime, especially in the case of disorder and spatial potential step. Yet, an exception occurs in the case of no implemented potential step, which does not feature non-zero R_{xx} around $E_F = 0\ eV$ while an effective transition occurs in G_{xy}. It is attributed to numerical errors due to singularities of the physical problem corresponding to the skipped part of points close to $E_F = 0\ eV$: technically, there should be at least a peak in R_{xx} showing the 0th mode of the Landau level.

To go further, one sees pronounced fluctuations in R_{xx} instead of smoother peaks as what was seen in the experimental results. This is certainly attributed to the uncorrelated disorder. Indeed, this results in strong fluctuating potential over possibly very small distances compared to the Fermi wavelength λ_F, which kills quantum phenomena regarding disorder probing in the mesoscopic regime. That way, information within the quantum Hall regime can be lost and bring these fluctuations instead of well-defined peaks which should arise in disorder configuration similar to electron-hole puddles. These aberrations are even perceptible with negative values of R_{xx} in case of zero potential step. Another observation is that as long as the potential step increases, the transition width in G_{xy} along with the associated fluctuations in R_{xx} is proportionally larger (a better view for the non-zero potential steps can be seen in Fig. 3.21 with G_{xy} only displayed). Therefore, in case of higher steps, percolation of edge channels into the bulk are more likely to occur and the well-defined plateaus are sooner left. For $\Delta V = 0\ eV$, one sees that the transition width between plateaus corresponding to $G_{xy} = 2e^2/h$ and $-2e^2/h$ is visibly non-zero but given the numerical errors, it should be actually zero. However, the other transitions have a finite width, which must be explained by a model involving the potential step ΔV. Surprisingly, while the first two plateaus appear in all cases (still with a smaller width as the step is higher), only the following ones appear in the case of the smallest steps, i.e. $\Delta V = 0.13\ eV$ and $0\ eV$ (plateaus encompassed with blue ovals with the corresponding zero longitudinal resistance and also one encompassed in red in left of Fig. 3.21 for $\Delta V = 0.13\ eV$). All other cases already show instability and this seems to be really depending on the step value. A final observation is the natural overall increase/decrease of the Hall conductance as long as the Fermi energy increases on either side.

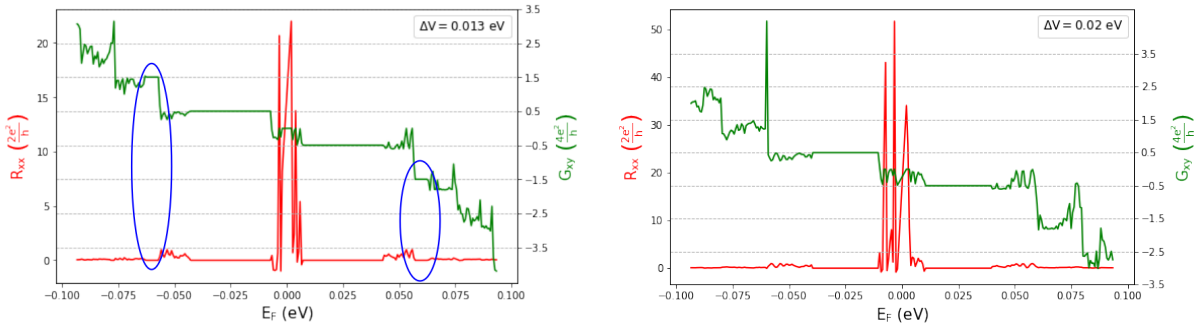

Fig. 3.19. (Left) Hall conductance G_{xy} and longitudinal resistance R_{xx} in function of the Fermi energy E_F at 7 T for $\Delta V = 2 * 0.1/s_f = 0.013\ eV$. (Right) Hall conductance G_{xy} and longitudinal resistance R_{xx} in function of the Fermi energy E_F at 7 T for $\Delta V = 2 * 0.15/s_f = 0.02\ eV$.

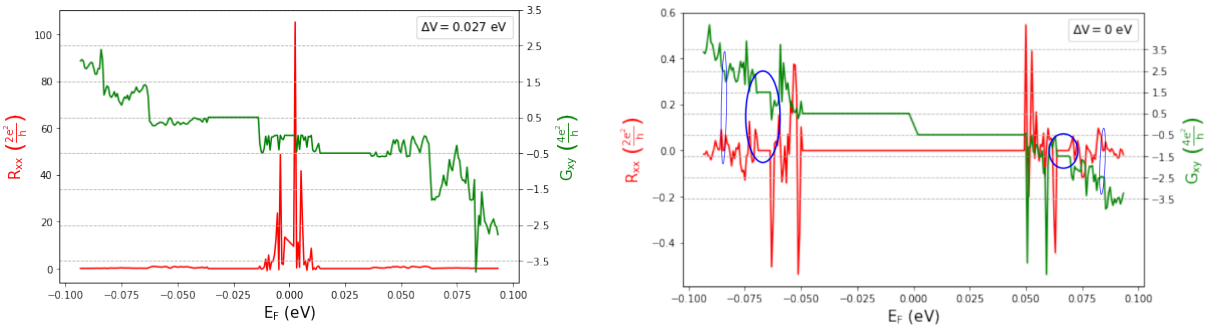

Fig. 3.20. (Left) Hall conductance G_{xy} and longitudinal resistance R_{xx} in function of the Fermi energy E_F at 7 T for $\Delta V = 2 * 0.2/s_f = 0.027\ eV$. (Right) Hall conductance G_{xy} and longitudinal resistance R_{xx} in function of the Fermi energy E_F at 7 T for $\Delta V = 0\ eV$.

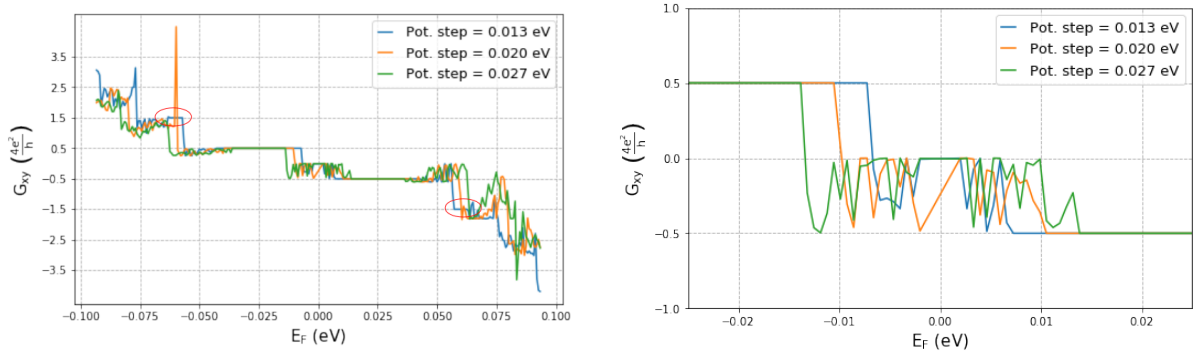

Fig. 3.21. (Left) Potential step-dependent Hall conductance G_{xy} in function of the Fermi energy E_F. (Right) Zoom of the left graph closer to $E_F = 0\ eV$.

In addition, another comparison has been made between G_{xy} with two different magnetic fields and a constant step of $\Delta V = 0.013\ eV$ as observed in Fig. 3.22. One sees that the Hall conductance associated with the highest field features much wider and stable plateaus in G_{xy} at 1 T surely in accordance with a higher energy gap ΔE_N between Landau levels. However, coming from $E_F = 0\ eV$, the first plateaus appear at the same energy level in both cases, which proves the presence of the 0th Landau level unchanged with varying magnetic field and the constant potential step thus does not affecting the onset of plateau unlike what has been seen above. Also, G_{xy} at 1 T never develops plateaus after the first thin ones and linearly evolves on average faster than the other cases at 7 T (note that the energy scale is much lower in left of Fig. 3.22).

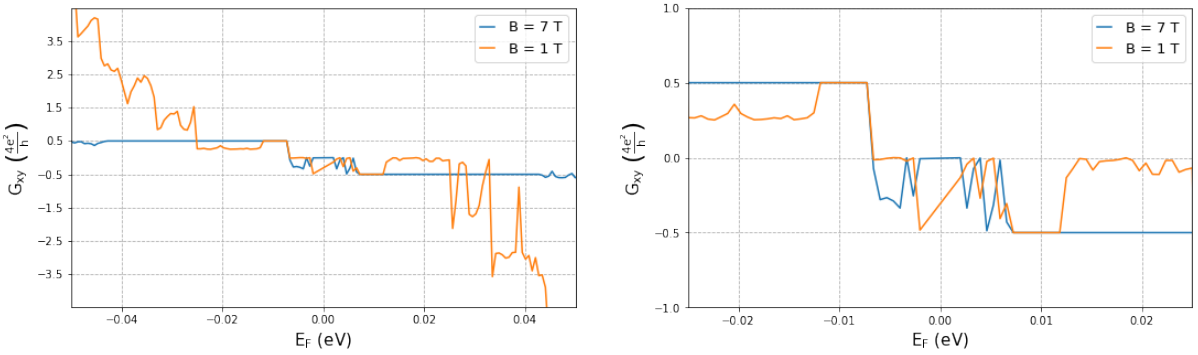

Fig. 3.22. (Left) B-dependent Hall conductances G_{xy} in function of the Fermi energy E_F for a potential step $\Delta V = 0.013\ eV$. (Right) Zoom of the left graph closer to $E_F = 0\ eV$.

Based on all observations, a new emerging model can be described to explain those depending on the spatial potential step ΔV and also on the magnetic field B inducing specific energy spacing ΔE_N

between Landau levels. This model is explained based on the schemes in Fig. 3.23 showing the potential change along the x-axis in accordance with the Kwant system. The very first aspect to consider is that the onsite potential spatially modified by the step will induce shifts of the Landau level spectrum corresponding to the local potential (in eV) defined by the hyperbolic tangent function (seen as the blue curves). To be precise, as seen on the current Figure, the Landau level energy spectrum (shown in yellow) is shifted downwards with the corresponding negative potential value "-pot" at the left end, while at the right end the spectrum shifts upwards according to the opposite value "+pot". In between, the shifts are less prominent but continuous and it is even zero at the middle. The 0th Landau level depicted on the schemes precisely follows the hyperbolic tangent function along the x-axis and the same applies for the other Landau levels. Physically in the quantum Hall regime, if the Fermi energy lies within a Landau level, conduction states are available in the bulk to flow and the induced perturbation of the voltage probes leads to a non-zero longitudinal resistance and to a transition between plateaus in the Hall resistance/conductance. If anywhere along the direction of the potential change, there are available states at the position x, then local percolation of conductive channels into the bulk occur at the same position and will induce non-zero R_{xx}. Therefore, it is relevant to consider the importance of the potential step ΔV and the specific energy spacing between Landau levels ΔE_N (i.e. also the magnetic field B) as well as their relation. Two conditions should be thus considered:

1. If $\Delta V > \Delta E_N$ between Landau levels N and $N\pm1$, then along x-axis there will be always conducting states in the bulk between the Nth level at the left end and the $(N-1)$th one at the right end[6]. This will never result in a plateau and non-zero longitudinal resistance. The assumption is still valid for higher Landau levels since the energy spacing is even more reduced but possibly the lower ones might not be affected by the potential step value for never reaching plateaus. In left of Fig. 3.23, the condition is already fulfilled with the 0th and (-)1st Landau levels since an overlapping is present due to the higher potential step ΔV. So, in this case, no plateau at all should be featured in a R_{xy} curve, which never happens in the simulated Kwant system by the way. Finally, increasing the magnetic field must thus relieve the problem of constant percolation into the bulk since the gap evolves as $\propto \sqrt{B}$;

2. If $\Delta V < \Delta E_N$, then the step is too small for featuring available states between the Nth and $(N-1)$th Landau levels and an associated plateau and zero value in R_{xx} will across on a small gap (see the red region on right of Fig. 3.23. This specificity unambiguously holds for lower Landau levels with even higher energy spacing. The case at higher levels will depend on the following energy spacing compared to the constant potential step.

These conditions allow to understand the profiles in Fig. 3.21: the first plateaus appear sooner from $E_F = 0\ eV$ as long as the potential step is smaller because the gap state in the spatial Landau level spectrum will be wider as can be imagine in right of Fig. 3.23. Also, these plateaus are less wider and start to sooner fluctuate towards higher energy if the step is higher because the same gap state gets more squeezed from both sides in terms of energy scale. The following plateaus only clearly appear for the lowest step (i.e., 0.013 eV) because the energy gap between the (-)1st and (-2)nd Landau levels is still higher than ΔV and is lower for the other cases with higher steps. However, in the case of no step in right of Fig. 3.20, there seems missing the third plateaus lying at $(-)10e^2/h$ whereas it should not be hidden since $\Delta V = 0 < \Delta E_N$. But the effect of uncorrelated disorder is not a good realistic model to fit with experiment to clearly see further wide enough plateaus. With a more precise view, these plateaus are still actually present with associated zero R_{xx} with identical width, as depicted inside the very thin ovals.

In Fig. 3.24, an additional curve has been added with two different values characterizing the potential Anderson disorder. One sees full qualitative similarities in both cases, from which it can be stated that this kind of disorder implementing is not really affecting much quantum Hall transport.

In conclusion, the starting hypothesis and the physical concept imagined behind it cannot explain the pronounced shift found in the experimental results in sample A using Kwant simulations. However, nice qualitative results were observed and have shown a lot of features. These were interpreted based on a new suggested model reliably explaining the transport phenomena in the quantum Hall regime with simple charge inhomogeneities implemented along the studied device. This work does not contradict the initial explanation about differences in CNPs in Hall and longitudinal resistances found in sample A since no specific edge disorder has been implemented to verify it.

[6]Given the current direction of the potential step. If it was reversed, then the Nth and $(N+1)$th levels would be involved.

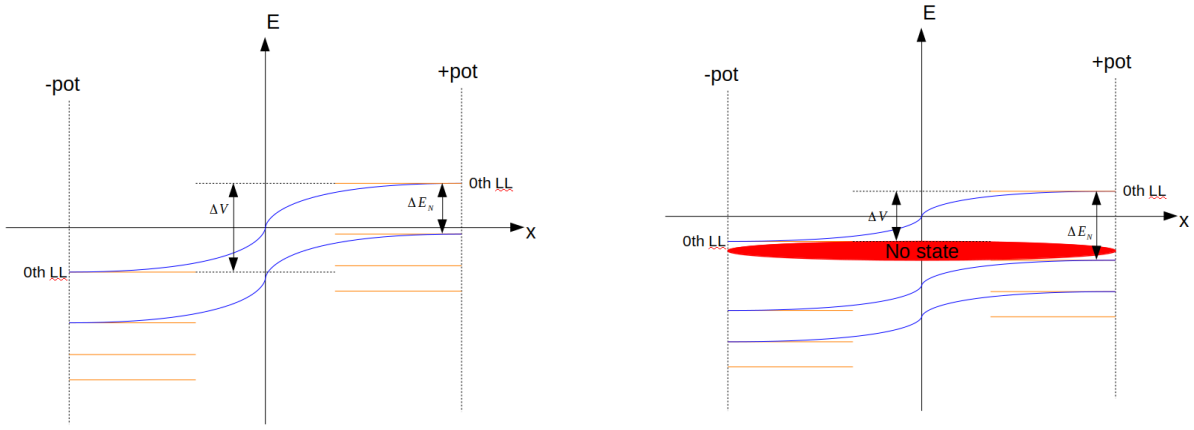

Fig. 3.23. (Left) Scheme of the spatial potential landscape defined by the step $\Delta V = 2 * \text{pot}$ and displayed Landau levels with the energy spacing ΔE_N between the 0th one and first one. Since $\Delta V > \Delta E_N$, there is no global gap in the DOS and percolation of edge channels into the bulk always occurs. (Right) Scheme of the spatial potential landscape defined by the step $\Delta V = 2 * \text{pot}$ and displayed Landau levels with the energy spacing ΔE_N between the 0th one and first one. Since $\Delta V < \Delta E_N$, there is a global gap in the DOS between the 0th Landau level at the left and the 1st one (hole side) on the right. The gap is depicted by the red region and percolation of the single edge channel into the bulk does not occur for Fermi energy within the gap, leading to quantized plateau in G_{xy}.

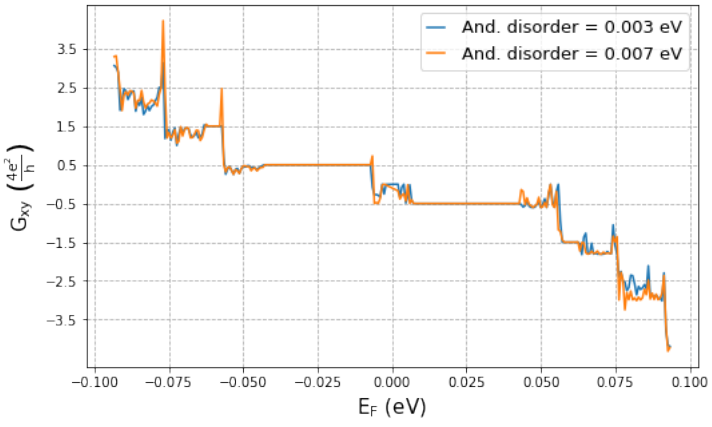

Fig. 3.24. Hall conductance G_{xy} in function of the Fermi energy E_F for two different Anderson disorder potential values at 7 T and for $\Delta V = 0.013$ eV.

Conclusion

The main goal of this master thesis project was to dive into many fields of electronic transport involved in graphene and in the presence of nanoconstrictions. It has been observed that despite the expected better properties from graphene encapsulated by hBN like in sample *A*, the sample with graphene directly on Si/SiO_2 have presented the most successful results. Indeed, more resolved Landau fan(s), better potential landscape with high lack of inhomogeneities, genuine signatures of size quantization and the possibility to have employed the model of quantum ballistic transport proves the high quality of this sample. Other previous works with graphene on SiO_2 featuring nanoconstrictions did not have the characteristics of ballistic transport due to a less suitable substrate than hBN. They have rather shown diffusive transport along with clear confinement in the nanoconstriction (notably reported in Ref. [18]). These samples were notably fabricated by mechanical exfoliation from graphite and the formation of the ribbons have induced strong disorder at the edges. Sample *B* is made of graphene grown by chemical vapor deposition and the associated fabrication process has been published rather recently [26]. Even if the details of the fabrication steps are not known, one can think about the great achievement for having examined and observing such good data even considering the SiO_2 substrate. Therefore, even if better substrates are theoretically and experimentally confirmed, the overall focus on good fabrication method can bring unexpected very good results.

Bibliography

[1] K. S. Novoselov, A. K. Geim, S. V. Morozov, D. Jiang, Y. Zhang, S. V. Dubonos, I. V. Grigorieva and A. A. Firsov. *Electric Field Effect in Atomically Thin Carbon Films.* Science **306**, 666 (2004).

[2] C. R. Dean, A. F. Young, I. Meric, C. Lee, L. Wang, S. Sorgenfrei, K. Watanabe, T. Taniguchi, P. Kim, K. L. Shepard and J. Hone. *Boron nitride substrates for high-quality graphene electronics.* Nature Nanotech. **5**, 722-726 (2010).

[3] R. Decker, Y. Wang, V. W. Brar, W. Regan, H.-Z. Tsai, Q. Wu, W. Gannett, A. Zettl and M. F. Crommie. *Local Electronic Properties of Graphene on a BN Substrate via Scanning Tunneling Microscopy.* Nano Lett. **11**, 2291-2295 (2011).

[4] S. D. Sarma, S. Adam, E. H. Hwang and E. Rossi. *Electronic transport in two dimensional graphene.* Rev. Mod. Phys. **83**, 407 (2011).

[5] B. Terrés, L.A. Chizhova, F. Libisch, J. Peiro, D. Jörger, S. Engels, A. Girshik, K. Watanabe, T. Taniguchi, S. V. Rotkin, J. Burgdörfer and C. Stampfer. *Size quantization of Dirac fermions in graphene constrictions.* Nature Communications **7**, 11528 (2016).

[6] A. H. Castro Neto, F. Guinea, N. M. R. Peres, K. S. Novoselov and A. K. Geim. *The electronic properties of graphene.* Rev. Mod. Phys. **81**, 109 (2009).

[7] N. A. Poklonski, E. F. Kislyakov, S. A. Vyrko, O. N. Bubel´ and S. V. Ratkevich. *Electronic band structure and magnetic states of zigzag graphene nanoribbons: Quantum chemical calculations.* Nanophotonics **6**, 061712-1 (2012).

[8] M. Wojtaszek. *Graphene: a two type charge carrier system.* Rijksuniversiteit Groningen, 2009.

[9] W. Jigang, M. Fengcai and S. Mengtao. *Graphene, hexagonal boron nitride, and their heterostructures: properties and applications.* RSC Adv. **7**, 16801 (2017).

[10] T. Taniguchi and K. Watanabe. *Synthesis of high-purity boron nitride single crystals under high pressure by using Ba–BN solvent.* Journal of Crystal Growth **303**, 525-529 (2007).

[11] A. Pakdel, C. Zhi, Y. Bando and D. Goldberg. *Low-dimensional boron nitride nanomaterials.* Materials Today **15**, 256-265 (2012).

[12] K. Zimmermann, A. Jordan, F. Gay, K. Watanabe, T. Taniguchi, Z. Han, V. Bouchiat, H. Sellier and B. Sacépé. *Tunable transmission of quantum Hall edge channels with full degeneracy lifting in split-gated graphene devices.* Nature Communications **8**, 14983 (2017).

[13] H. van Houten, C. W. J. Beenakker and B. J. van Wees. *Quantum Point Contacts.* Semiconductors and Semimetals **35**, 9-112 (1992).

[14] B. Brun. *Electron interactions in mesoscopic physics: scanning gate microscopy and interferometry at a quantum point contact.* Université de Grenoble, 2014.

[15] H. van Houten and C. W. J. Beenakker. *The quantization of ballistic electron transport through a constriction demonstrates that conduction is transmission.* Physics Today **35**, 22 (1996).

[16] B. J. van Wees, L. P. Kouwenhoven, E. M. M. Willems, C. J. P. M. Harmans, J. E. Mooij, H. van Houten, C. W. J. Beenakker, J. G. Williamson and C. T. Foxon. *Quantum ballistic and adiabatic electron transport studied with quantum point contacts.* Phys. Rev. B **43**, 12431 (1991).

[17] K. Zimmermann. *Quantum point contact in high mobility graphene.* Université Grenoble Alpes, 2016.

[18] J. Güttinger, F. Molitor, C. Stampfer, S. Schnez, A. Jacobsen, S. Dröscher, T. Ihn and K. Ensslin. *Transport through graphene quantum dots.* Rep. Prog. Phys. **75**, 126502 (2012).

[19] N. Tombros, A. Veligura, J. Junesch, M. H. D. Guimarães, I. J. Vera-Marun, H. T. Jonkman and B. J. van Wees. *Quantized conductance of a suspended graphene nanoconstriction.* Nature Physics **7**, 697-700 (2011).

[20] S. Somanchi, B. Terrés, J. Peiro, M. Staggenborg, K. Watanabe, T. Taniguchi, B. Beschoten and C. Stampfer. *From Diffusive to Ballistic Transport in Etched Graphene Constrictions and Nanoribbons.* Ann. Phys. **529**, 1700082 (2017).

[21] D. Bischoff, T. Krähenmann, S. Dröscher, M. A. Gruner, C. Barraud, T. Ihn and K. Ensslin. *Reactive-ion-etched graphene nanoribbons on a hexagonal boron nitride substrate.* Appl. Phys. Lett. **101**, 203103 (2012).

[22] B. Terrés. *Ballistic transport in graphene nanostructures.* RWTH Aachen University, 2016.

[23] K. von Klitzing. *The quantized Hall effect.* Modern Physics **58**, 3 (1986).

[24] K. S. Novoselov, A. K. Geim, S. V. Morozov, D. Jiang, M. I. Katsnelson, I. V. Grigorieva, S. V. Dubonos and A. A. Firsov. *Two-dimensional gas of massless Dirac fermions in graphene.* Nature **438**, 197-200 (2005).

[25] K. S. Novoselov, Z. Jiang, Y. Zhang, S. V. Morozov, H. L. Stormer, U. Zeitler, J. C. Maan, G. S. Boebinger, P. Kim and A. K. Geim. *Room-Temperature Quantum Hall Effect in Graphene.* Science **315**, 1379 (2007).

[26] J. E. Scheerder, T. Picot, N. Reckinger, T. Sneyder, V. S. Zharinov, J.-F. Colomer, E. Janssens and Joris Van de Vondel. *Decorating graphene with size-selected few-atom clusters: a novel approach to investigate graphene–adparticle interactions.* Nanoscale **9**, 10494-10501 (2017).

[27] American Magnetics. Low temperature inserts. `http://www.americanmagnetics.com/inserts.php`.

[28] D. Cabossart. *Coherent transport and scanning gate microscopy in graphene devices.* Université catholique de Louvain, 2016.

[29] Y.-W. Tan, Y. Zhang, H.L. Stormer and P. Kim. *Temperature dependent electron transport in graphene.* Eur. Phys. J. Special Topics **148**, 15-18 (2007).

[30] Y. Zhang, Z. Jiang, J. P. Small, M.S. Purewal ans Y.-W. Tan, M. Fazlollahi, J.D. Chudow, J.A. Jaszczak, H.L. Stormer and P. Kim. *Landau-Level Splitting in Graphene in High Magnetic Fields.* Phys. Rev. Lett. **96**, 136806 (2006).

[31] C. W. Groth, M. Wimmer, A. R. Akhmerov and X. Waintal. *Kwant: a software package for quantum transport.* New Journal of Physics **16**, 063065 (2014).

[32] M.-H. Liu, P. Rickhaus, P. Makk, E. Tóvári, R. Mauran, F. Tkatschenko, M. Weiss, C. Schönenberg and K. Richter. *Scalable Tight-Binding Model for Graphene.* Phys. Rev. Lett. **114**, 036601 (2015).

Appendices

A Supplementary plots

Sample A

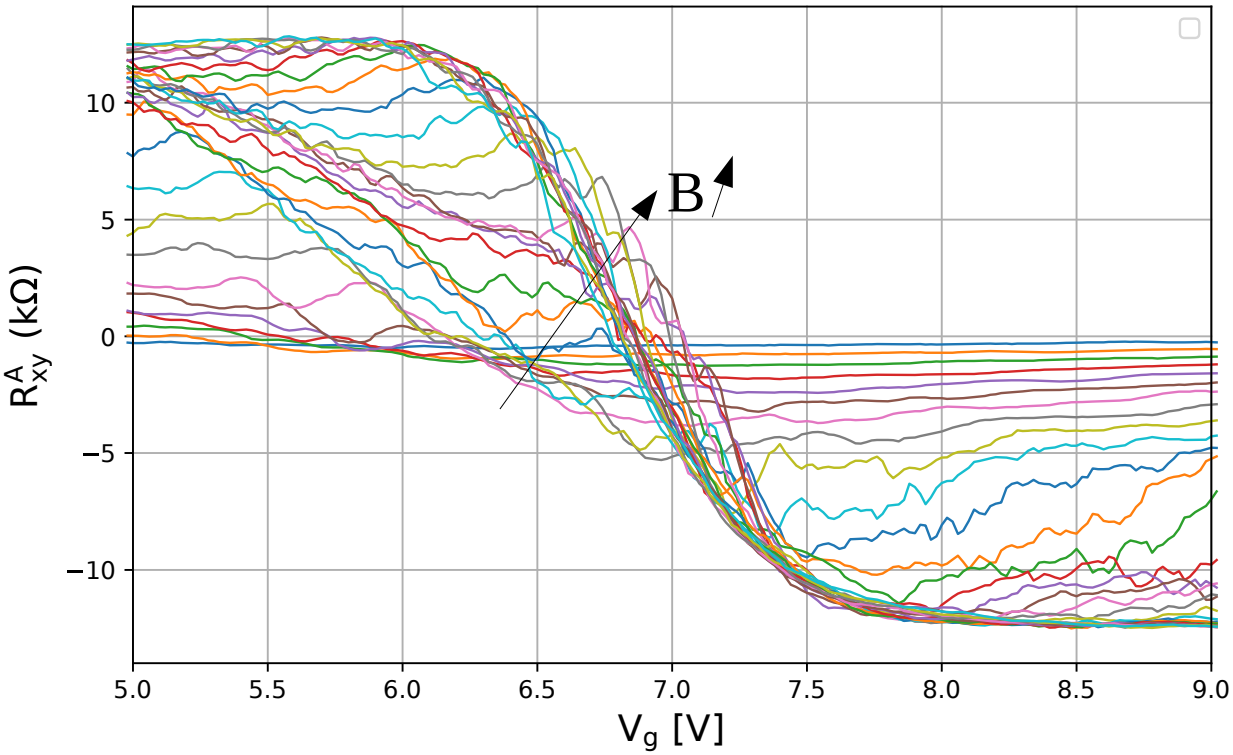

Fig. A.1. Hall resistance traces R^A_{xy} in sample A in function of gate voltage V_g for all swept magnetic field values with the longest arrow indicating the evolution of curves whose sign change location shift towards to the right as B increases.

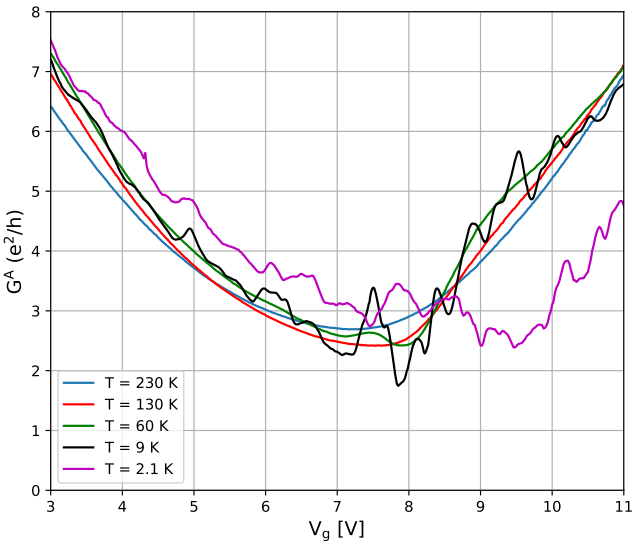

Fig. A.2. Dependency of the longitudinal conductance G^A on temperature T in function of the back-gate voltage V_g. The CNP associated with the minimum conductance of the lowest T curve (in purple) is clearly shifted to the right compared to the other curves. This is experimentally explained by the corresponding measurement realized after an unwitting cool-down process of sample A, which was due to another cooling procedure of the VTI+cryogenic system that has been restarted. The other measurements according to the temperature-dependence transport were anterior.

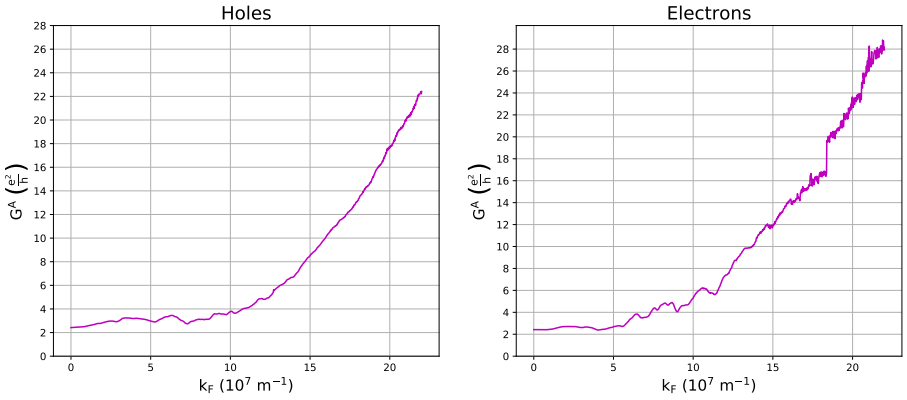

Fig. A.3. Evolution of the zero-field conductance G^A on the hole and electron side as a function of the Fermi wavenumber k_F (computed as $\sqrt{\pi n}$) in sample A at 2 K.

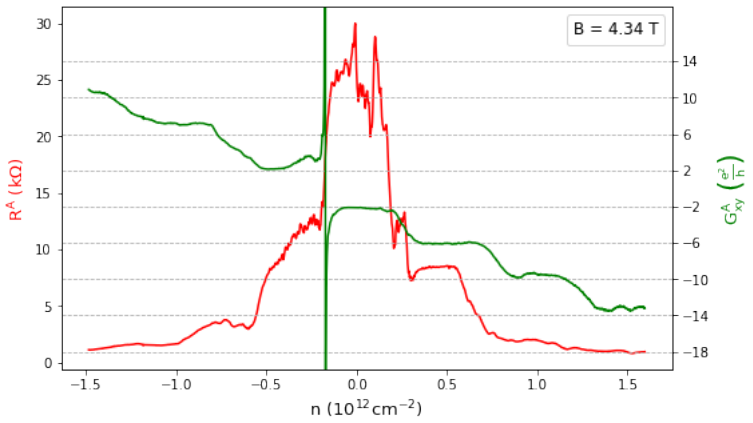

Fig. A.4. Hall conductance G_{xy} showing successive plateaus down to $-14e^2/h$ at $B \sim 4.3\ T$.

Sample B

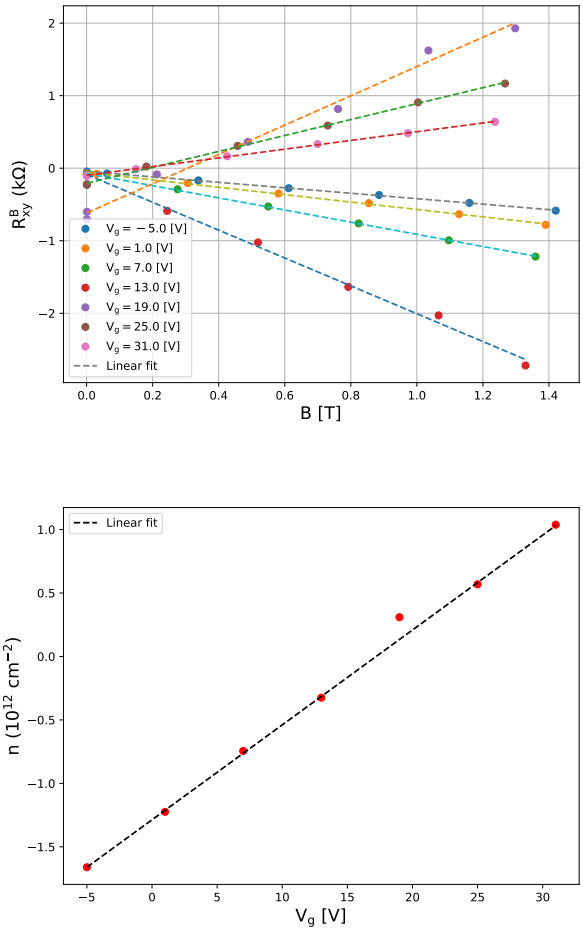

Fig. A.5. (Left) Evolution of the Hall resistance R^B_{xy} with magnetic field B for different back-gate voltage values V_g. The dashed lines are linear fits according to the Hall resistance expression in 2D (see main text) in order to determine the carrier density n. (Right) Data set collected from the computed carrier density from the left plot with respect to each back-gate voltage value (sample B). The linear fit only goes through the most reliable dots, the outsider one being close to the Dirac point ($\sim 17\ V$). The steepness gives one of the two experimental values of the gate lever-arm α^B_{exp1}.

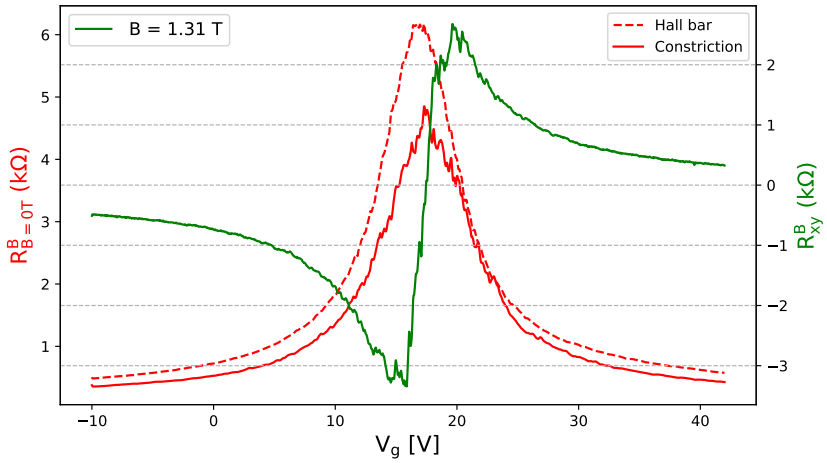

Fig. A.6. Transverse resistance R^B_{xy} under non-zero magnetic field and longitudinal resistances R^B_{HB},R^B_{QPC} at zero field plotted as a function of gate voltage V_g. One sees a very good superposition of the sign change of R^B_{xy} and the CNP characteristic of both longitudinal resistances ($\sim 17\ V$). The B-label is the real value at the middle of the trace close to the CNP.

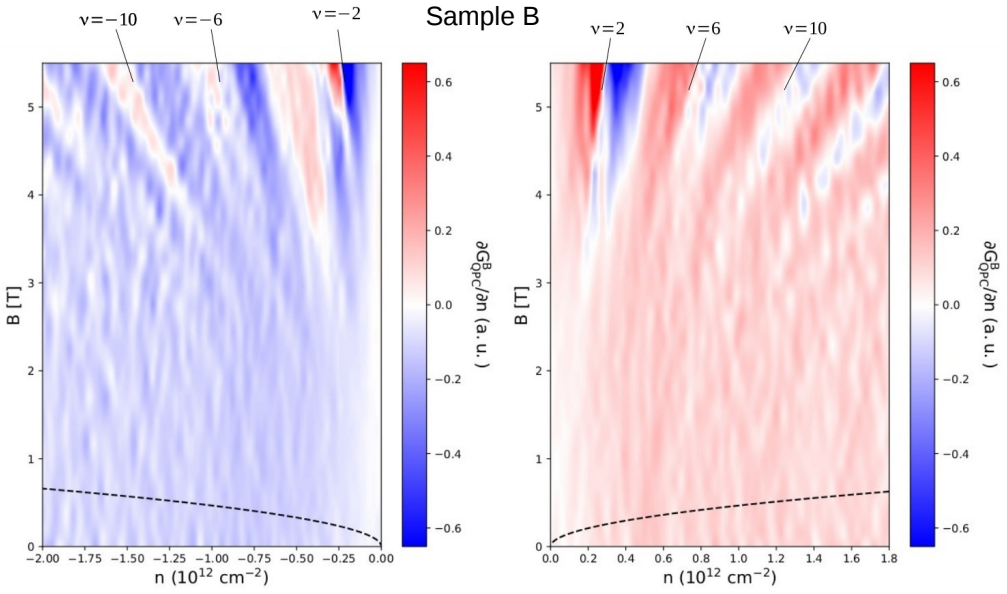

Fig. A.7. Zoom on the low-field Landau level fan on the hole side (left) and electron side (right) for the analysis of the size quantized values from the subbands toward the Landau level quantization at critical fields B_c.

B Calculation details

B.1 One-dimensional transport for the conductance determination

Inspired from LELEC2710 course

For determining the conductance through a quasi-1D channel, one must take into account the flowing current to be computed. Consider a source S and a drain D (contacts) with respective chemical potential $\mu_S = eV_S$ and $\mu_D = eV_D$ and a flowing current from S to D through a QPC. Before computing the conductance through a QPC, just consider a 1D wire. The current can be expressed as $I = nev$, where n is the density, e the electronic charge and v the group velocity. In the case of reflection at the contacts, two contributions from current comes into play, I^+ from S to D and I^- from D to S. The current I^+:

$$I^+ = e \int_0^{\mu_S} \frac{D(E)}{2} f(E) v(E) dE,$$

where $D(E)$ is the density of 1D states, $f(E)$ is the Fermi-Dirac distribution and the "1/2" factor accounts for only forward electrons with "+k" momentum. In 1D, the DOS is $D(E) = \frac{1}{\pi\hbar}\sqrt{\frac{2m^*}{E}}$ and the group velocity $v(E) = \sqrt{\frac{2E}{m^*}}$. So in 1D, the product $D(E)v(E) = \frac{2}{\pi\hbar}$ is energy-independent. Hence,

$$I^+ = \frac{2e}{h} \int_0^{\mu_S} f(E) dE.$$

If $T = 0\ K$, then $I^+ = \frac{2e}{h}\mu_S$. The same reasoning also applies for I^-: $I^- = \frac{2e}{h}\mu_D$. The total current is thus

$$I = I^+ I^- = \frac{2e}{h}(\mu_S - \mu_D) = \frac{2e^2}{h}(V_S - V_D) = \frac{2e^2}{h}\Delta V.$$

Hence the conductance $G = \frac{I}{\Delta V} = \frac{2e^2}{h}$.

This supposes that only one mode is transmitted. If several ones are involved in quasi 1D wires, then $G = \frac{2e^2}{h}M$, with M the number of modes. Now, considering a scattering region in the channel with characteristic transmission probability T like in a QPC, then three current contributions appear: the forward current I_1^+ behind the scattering region, the reflecting current I_1^- at the scattering region and the transmitted current I_2^+ which is the objective. Knowing that $I_1^+ = \frac{2e}{h}M(\mu_S - \mu_D)$ is the same as before, then $I_2^- = \frac{2e}{h}MT(\mu_S - \mu_D$. Finally, one simply obtains

$$I_2^+ = I_1^+ - I_1^- = \frac{2e}{h}MT(\mu_S - \mu_D).$$

Finally, one gets the final conductance in a quasi 1D wire with transmission probability

$$G = \frac{2e^2}{h}MT,$$

expressed in the Landauer formalism. Note that each mode can benefit from its own transmission probability T_n, which would give a sum over all modes considered at the Fermi level.

B.2 Extraction of the gate lever-arm based on the Landau level spectrum according to the V_g vs. B evolution

Based on the Supplementary Notes from Ref. [5]

Compared to the extraction method of the gate lever-arm α in the classical Hall regime, transiting from the electronic states at zero/weak magnetic fields to the quantized Landau states at higher magnetic fields allows another experimental determination of it. To do it, one has to consider both the energy dispersion E and the different Laudau level energy E_N development in graphene in function of gate voltage V_g and magnetic field B respectively:

$$E = \hbar v_F k_F = \hbar v_F \sqrt{\pi\alpha\Delta V_g} \text{ and } E_N = sgn(N) v_F \sqrt{2e\hbar|N|B},$$

where $\Delta V_g = V_g - V_{g0}$ and N the Landau level index (integer number). If α is assumed to be constant[7], equating E to E_N amounts to know the evolution of the Landau levels in a V_g-B plane:

$$E^2 = E_N^2 \Longleftrightarrow \hbar^2 v_F^2 \pi \alpha \Delta V_g = v_F^2 2e\hbar N B \Longleftrightarrow B = C_N \Delta V_g,$$

where $C_N = \dfrac{h\alpha}{4eN}$ corresponds to the slope of the Nth Landau level evolution in the V_g-B plane.

In a map where a Landau fan as a function of V_g and B is developed, fitting a straight line into each of the different Landau levels allows to determine the slopes and thus find the constant gate lever-arm α. Instead of what was being consulted in the Terrés *et al.* Supplementary Notes, it should be suggested to fit those lines in the loci of the maximum longitudinal resistance (in a 4-probe measurement) in a Landau map, not the minimum one. This suggestion is argued by the $E = E_N$ equality which is used to determine α. The hypothesis behind this is that one has to always follow the electronic states of the Laudau levels for this exercise. Physically, the corresponding electronic states contribute to transport in the bulk of a sample, leading to bulk scatterings which generate a non-zero voltage drop, hence a non-zero resistance value. The loci of minimum resistance correspond to situations where the Fermi level is lying between two successive Landau levels in the bulk: the transport within the associated edge states (due to the bending of the Landau levels towards the end of the sample) is protected from scattering events and thus leads to an equilibrium and equality of the chemical potentials between the voltage probings corresponding to the longitudinal resistance measurement, leading to zero values in this case. This does not obey the hypothesis above, so only the loci of maximum resistance should be followed. By the way, this explanation can be justified by the locations of the filling factors $\nu \propto n = \alpha \Delta V_g$ at high magnetic fields at the right drops of the minimal 4-probe longitudinal resistance, which is realized in the main text.

[7] In fact, this is not true as it is said that it diverges at the lowest Landau levels close to the Dirac point but it gets nonetheless constant for the higher Landau levels [22].

C Kwant software for simulating mesoscopic transport within the tight-binding model

Mainly taken from Ref. [28]

Kwant is a publicly available python package for numerical quantum transport calculations. It aims to be a user-friendly, universal, and high-performance toolbox for the simulation of physical systems of any dimensionality and geometry that can be described by a tight-binding model (the full description can be seen in the official paper [31]). The established algorithms allow to solve the scattering problem of a particle in an open or closed system coupled to semi-infinite leads. Based on this, various transport properties can be extracted from the system such as dispersion relations, electrical conductance, local density of states, wavefunctions etc.

Solving the scattering problem in Kwant within the tight-binding model requires to discretize the continuous Hamiltonian H of a single-particle in a non-interacting two dimensional system, i.e. discretize

$$H = \frac{-\hbar^2}{2m^*}(\partial_x^2 + \partial_y^2) + V(x, y),$$

where m^* is the effective mass and $V(x, y)$ the local potential energy. The discretized Hamiltonian is computed based on a scattering region described with sites and hoppings between neighbouring sites (see Fig. C.1). While the region is defined, semi-infinite leads are attached to it and act as quasi 1D conductors for the transmission of electronic modes through the scattering region or they can also be used as voltage probes. The definition of the discrete Hamiltonian can be done for simple square lattice with lattice constant a: to each site of the lattice is associated integer lattice coordinates (i, j) (and then corresponding real-space coordinates $(x, y) = (a_i, a_j)$) as well as potential state $|i, j\rangle$. In the limit $a \to 0$, the continuous Hamiltonian shown above can be approximated as:

$$H = \sum_{i,j}[(V(a_i, a_j) + 4t)\,|i, j\rangle\,\langle i, j| - t(|i + 1, j\rangle\,\langle i, j| + |i, j\rangle\,\langle i + 1, j| + |i, j + 1\rangle\,\langle i, j| + |i, j\rangle\,\langle i, j + 1|)],$$

where t is the hopping energy between the first-nearest-neighbours. To make this specific model numerically valid (model being an approximation of the physical reality), there are two important conditions to fulfill:

1. The most important is that the electrons must remain tightly bound to the nuclei. Therefore, the energy ranges E of the Kwant system that can be studied should be at least lower than the hopping energy t: $E < t$[8];
2. To avoid numerical abberations, the Fermi oscillation associated with at least the highest electronic wavelength λ_F should be described by a few sites and thus should be much higher than the lattice constant a: $\lambda_F >> a$.

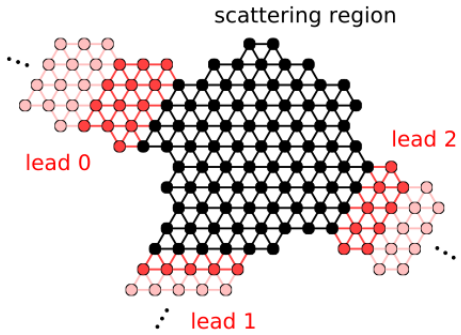

Fig. C.1. Structure of a tight-binding system in Kwant. The black dots are sites belonging to the scattering region; the bonds between interconnected neighbouring sites are described by hoppings; red dots are represented by the three semi-infinite leads attached to the scattering region with their corresponding unit cell drawn in a different shade [31].

[8] In the codes, the energy range was even restricted to $E < t/2$.

In Kwant, the discrete Hamiltonian for a graphene system, i.e. a honeycomb lattice, can be computed. The specific geometry of the scattering region is defined by starting from an infinite honeycomb lattice where one selects specific sites that will form the final device. Then, the semi-infinite leads are connected to the scattering region. Finally, one has to set the main parameters defining the investigated system that are used as inputs for calculations. These are the graphene lattice constant a (i.e. the carbon-carbon distance), the hopping energy t[9], the so-called onsite potential energy $V(a_i, a_j)$, the Fermi energy of the whole system E_F and the magnetic field B.

Another important aspect in simulations is to deal with computation time. In Kwant, to adapt the system to some experimental device dimensions (in the microscopic scale for instance), a lot of sites has to be created and this can require heavy time of calculations. To allow to deal with a lighter system while keeping the transport properties characteristic of the system with realistic dimensions and geometry from experiment, a scaling parameter called *scaling factor* s_f can be employed. If $s_f > 1$ and is applied to the lattice constant of the "real" system a_0 to give the scaled lattice constant $a = s_f a_0$, less sites will be generated with reduced time for the post calculations. Regarding graphene, a scientific paper describes a scalable tight-binding model in order not to alter the electronic properties of the real graphene system while a scaling process is considered for the simulations [32]. In the low energy range in graphene ($|E| < 1\ eV$), the Dirac Hamiltonian well describes the real graphene system and the peculiar linear dispersion $E_0(k_F) = \pm\hbar v_F k_F$ with the Fermi velocity $v_F \simeq 10^6\ m/s$. In terms of tight-binding parameters, $\hbar v_F = (3/2)a_0 t_0$, where $a_0 \simeq 0.142\ nm$ is the real carbon-carbon distance and $t_0 \simeq 2.8\ eV$ the nearest neighbour hopping energy. Now, the scaled graphene system defined with scaled tight-binding parameters a, t and dispersion relation $E(k_F) = (3/2)atk_F$ is described by the scaling factor s_f. In order not to modify the properties from the real graphene system, the band structure, hence the dispersion must be unchanged. This condition is fulfilled by setting $a = s_f a_0$ and $t = t_0/s_f$. This model was used for the simulations described in Section 3.4. It is still valid as long as $\lambda_F >> a$ like said above. In the scaled system, this holds if

$$s_f << \frac{3t_0\pi}{|E_{max}|},$$

where $|E_{max}|$ is the maximal energy of interest to investigate the real graphene system. Hence, if high carrier densities (at high energy) are desired, the constraint on s_f selection becomes stronger. In addition, the presence of a perpendicular magnetic field B_z within the tight-binding formulation amounts to invoke a new restriction on the Peierls substitution (see main text for its brief description): the magnetic length $l_B = \sqrt{\hbar/eB_z}$ must be higher than the scaled lattice parameter a: $l_B >> a$. This leads to

$$s_f << \frac{l_B}{a_0} \sim \frac{180}{\sqrt{B_z}}.$$

Solvers in Kwant allow to extract the transport properties on the basis of the scattering problem. The mathematical description of the problem solving can be found in Ref. [31]. For example, if conductance G between two quasi 1D leads is the desired property to compute based on the main parameters, Kwant will have to determine the scattering matrix S_{nm} and then to compute the total transmission T (in units of $2e^2/h$ taking into account spin degeneracy, which directly gives $G = 2e^2/h \cdot T$ or $G = 2 * 2e^2/h \cdot T$ for the additional valley degeneracy in graphene) by summing the S-matrix elements from each mode of the first lead to all modes of the last lead:

$$G_{ab} = \frac{2e^2}{h} \sum_{n\in a, m\in b} S_{nm},$$

where a, b denoting the lead indices and

$$\sum_{n\in a, m\in b} S_{nm} = T(E_F).$$

In the main text (see Section 3.4), simulations analogous to four-probe measurements are shown and explained. They aim to try reproducing the pronounced shift between the Hall resistance transition (between $\nu = -2$ and $\nu = 2$) and the maximum longitudinal resistance associated with the 0th Landau level in sample A by invoking a starting hypothesis of charge inhomogeneities at different contacts.

[9] In the codes, the hoppings were defined based on the deal with the two sublattices in graphene in which one site from a single one is bound to three sites from the other.

UNIVERSITÉ CATHOLIQUE DE LOUVAIN
École polytechnique de Louvain
Rue Archimède, 1 bte L6.11.01, 1348 Louvain-la-Neuve, Belgique | **www.uclouvain.be/epl**